

 Open access • Journal Article • DOI:10.1364/OL.18.000565

Confocal microscopy through a fiber-optic imaging bundle — [Source link](#)

Arthur F. Gmitro, David J. Aziz

Institutions: University of Arizona

Published on: 15 Apr 1993 - Optics Letters (Optical Society of America)

Topics: Confocal, Scanning confocal electron microscopy, Confocal microscopy, Microscope and Microscopy

Related papers:

- [Slit-scanning confocal microendoscope for high-resolution in vivo imaging](#)
- [Micromachined scanning confocal optical microscope](#)
- [Fiber-optic fluorescence imaging.](#)
- [Endoscope-compatible confocal microscope using a gradient index-lens system](#)
- [Design and demonstration of a miniature catheter for a confocal microendoscope](#)

Share this paper:    

View more about this paper here: <https://typeset.io/papers/confocal-microscopy-through-a-fiber-optic-imaging-bundle-2zpiczt7n6>



Confocal microscopy through a fiber-optic imaging bundle.

Item Type	text; Dissertation-Reproduction (electronic)
Authors	Aziz, David Joshua.
Publisher	The University of Arizona.
Rights	Copyright © is held by the author. Digital access to this material is made possible by the University Libraries, University of Arizona. Further transmission, reproduction or presentation (such as public display or performance) of protected items is prohibited except with permission of the author.
Download date	30/05/2022 14:25:16
Link to Item	http://hdl.handle.net/10150/187269

INFORMATION TO USERS

This manuscript has been reproduced from the microfilm master. UMI films the text directly from the original or copy submitted. Thus, some thesis and dissertation copies are in typewriter face, while others may be from any type of computer printer.

The quality of this reproduction is dependent upon the quality of the copy submitted. Broken or indistinct print, colored or poor quality illustrations and photographs, print bleedthrough, substandard margins, and improper alignment can adversely affect reproduction.

In the unlikely event that the author did not send UMI a complete manuscript and there are missing pages, these will be noted. Also, if unauthorized copyright material had to be removed, a note will indicate the deletion.

Oversize materials (e.g., maps, drawings, charts) are reproduced by sectioning the original, beginning at the upper left-hand corner and continuing from left to right in equal sections with small overlaps. Each original is also photographed in one exposure and is included in reduced form at the back of the book.

Photographs included in the original manuscript have been reproduced xerographically in this copy. Higher quality 6" x 9" black and white photographic prints are available for any photographs or illustrations appearing in this copy for an additional charge. Contact UMI directly to order.

UMI

A Bell & Howell Information Company
300 North Zeeb Road, Ann Arbor, MI 48106-1346 USA
313/761-4700 800/521-0600

CONFOCAL MICROSCOPY THROUGH A FIBER-OPTIC IMAGING BUNDLE

by

David Joshua Aziz

Copyright © David Joshua Aziz 1995

A Dissertation Submitted to the Faculty of the
COMMITTEE ON OPTICAL SCIENCES (GRADUATE)

In Partial Fulfillment of the Requirements
For the Degree of

DOCTOR OF PHILOSOPHY

In the Graduate College

THE UNIVERSITY OF ARIZONA

1995

UMI Number: 9603717

Copyright 1995 by
Aziz, David Joshua
All rights reserved.

UMI Microform 9603717
Copyright 1995, by UMI Company. All rights reserved.

This microform edition is protected against unauthorized
copying under Title 17, United States Code.

UMI

300 North Zeeb Road
Ann Arbor, MI 48103

THE UNIVERSITY OF ARIZONA
GRADUATE COLLEGE

As members of the Final Examination Committee, we certify that we have
read the dissertation prepared by David Joshua Aziz
entitled Confocal Microscopy Through A Fiber-Optic Imaging Bundle

and recommend that it be accepted as fulfilling the dissertation
requirement for the Degree of Doctor of Philosophy

Arthur Gmitro	<u>Arthur Gmitro</u>	<u>6/19/95</u>
		Date
James Burke	<u>James Burke</u>	<u>6/19/95</u>
		Date
Jose Sasian	<u>Jose M Sasian</u>	<u>6/19/95</u>
		Date
_____		Date
_____		Date

Final approval and acceptance of this dissertation is contingent upon
the candidate's submission of the final copy of the dissertation to the
Graduate College.

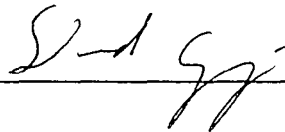
I hereby certify that I have read this dissertation prepared under my
direction and recommend that it be accepted as fulfilling the dissertation
requirement.

Arthur Gmitro	<u>6/15/95</u>
Dissertation Director	Date
<u>Arthur Gmitro</u>	

STATEMENT BY AUTHOR

This dissertation has been submitted in partial fulfillment of requirements for an advanced degree at The University of Arizona, and is deposited in the University Library to be made available to borrowers under rules of the Library.

Brief quotations from this dissertation are allowable without special permission, provided that accurate acknowledgment of source is made. Requests for permission for extended quotation from or reproduction of this manuscript in whole or in part may be granted by the copyright holder.

SIGNED:  _____

ACKNOWLEDGEMENTS

The greatest thanks go to my advisor, Art Gmitro. Art provided both guidance and support, while at the same time allowing me to follow a path of my own choosing. I benefited greatly from his advice and feedback, as well as from the detours he allowed me to take. As the years have passed and the number of students I've met at the Optical Sciences Center has grown, I've come to realize how fortunate I was to join Art's group.

I would also like to thank Steve Dvorak, Jack Gaskill, Tony Caruso, and Evan Unger who successively provided funding for me over much of the last five years. Without financial support from these individuals, my graduate school experience would have been much less fruitful. I learned as much from my "day jobs" as I did from my dissertation research.

My fellow students have greatly enhanced my graduate school experience. Andy Alexander, Carolyn Davenport, and Paul Keller constituted the core of Art's group during my early years here. More recently, C. Lamar Coleman and Yash Sabharwal have taken over this role (and the lab). In general, the faculty, staff, and students of the Optical Sciences Center combine to make an excellent program.

Last, but certainly not least, I would like to acknowledge my wife, Aliza, and son, Aryeh. After moving from Manhattan to join me in Tucson, Aliza has put up with four years of crazy hours and little income. Aryeh's arrival this year convinced me that it is time to graduate and head back out into the real world.

DEDICATION

This dissertation is dedicated to my parents, Rahmat and Simi Aziz, for a lifetime of love and support.

TABLE OF CONTENTS

LIST OF FIGURES.....	9
LIST OF TABLES.....	14
ABSTRACT.....	15
1. INTRODUCTION	16
1.1. Overview of confocal microscopy.....	16
1.2. Motivation for a fiber-optic imaging-bundle confocal microscope.....	21
1.3. Scope and organization of this work.....	23
2. CONFOCAL MICROSCOPY.....	25
2.1. Optical sectioning (axial resolution).....	25
2.2. Lateral resolution.....	33
2.3. Modes of operation	33
<i>Trans-illumination</i>	34
<i>Epi-illumination</i>	34
<i>Brightfield</i>	35
<i>Fluorescence</i>	35
2.4. Detectors.....	35
<i>Pinhole detector apertures</i>	36
<i>Slit detector apertures</i>	37
<i>Array detectors</i>	41
2.5. Scanning techniques	41
<i>Object (stage) scanning</i>	42
<i>Objective scanning</i>	42
<i>Beam scanning</i>	43
<i>Galvanometer mirrors</i>	44
<i>Nipkow disk</i>	44
<i>Acousto-optic cells</i>	45
<i>Spinning polygon</i>	45
2.6. Slit scanning	46
2.7. Aberrations.....	47
2.8. Sources.....	48
2.9. Pupil filters	48
2.10. Applications.....	49
3. OPTICAL FIBERS.....	51
3.1. Ray description	51
3.2. Mode description	54
3.3. Weakly guiding fibers.....	58
3.4. Numerical aperture	58
3.5. Number of bound modes.....	59
3.6. Dispersion	60

TABLE OF CONTENTS - *Continued*

3.7. Materials.....	61
3.8. Losses.....	62
<i>Fresnel reflections</i>	62
<i>Unbound modes</i>	63
<i>Finite cladding thickness</i>	63
<i>Scattering</i>	64
<i>Absorption</i>	64
<i>Bending</i>	65
4. FIBER-OPTIC IMAGING BUNDLES	66
4.1. Imaging bundle characteristics	67
<i>Fiber size, shape, and spacing</i>	68
<i>Numerical aperture</i>	70
<i>Modes</i>	70
<i>Crosstalk</i>	71
<i>Cladding modes</i>	72
<i>Bundle sizes</i>	73
<i>Losses</i>	73
<i>Packing fraction</i>	73
<i>Coupling losses</i>	74
<i>Transmission losses</i>	75
<i>Distortion</i>	75
4.2. Imaging properties.....	75
<i>Static scanning</i>	77
<i>Dynamic scanning</i>	82
4.3. Imaging bundle types	82
<i>Flexible imaging bundles</i>	82
<i>Bundle construction</i>	83
<i>Materials</i>	87
<i>Rigid image bundles</i>	89
4.4. Evaluation of three flexible silica multi-core fiber bundles.....	89
<i>Refractive indices and numerical aperture</i>	92
<i>Core spacing</i>	99
<i>Core size and packing fraction</i>	100
<i>Bound modes</i>	102
<i>Coupling</i>	106
<i>Crosstalk</i>	108
<i>Stray light and/or cladding modes</i>	110
<i>Conclusion of bundles evaluation</i>	110

TABLE OF CONTENTS - *Continued*

5. FIBER-OPTIC IMAGING-BUNDLE CONFOCAL MICROSCOPE	112
5.1. Fiber-optic confocal microscope (single fiber)	113
5.2. Fiber-optic imaging-bundle confocal microscope	115
<i>Modification of a confocal microscope for fiber-optic imaging</i>	
<i>bundle operation</i>	119
<i>Bundle characteristics</i>	121
<i>Fiber size and spacing</i>	121
<i>Numerical aperture</i>	123
<i>Bundle size</i>	124
<i>Bundle materials</i>	124
<i>Scanning</i>	125
<i>Optical sectioning (axial resolution)</i>	126
<i>Reflection-mode axial resolution</i>	128
<i>Fluorescence-mode axial resolution</i>	136
<i>Lateral resolution</i>	144
<i>Space variance</i>	144
<i>Radiometry</i>	149
<i>Losses</i>	151
<i>Background noise</i>	153
<i>Distal objective lens</i>	155
<i>Magnification</i>	157
<i>Telecentricity</i>	159
<i>Aberrations</i>	161
<i>Potential designs</i>	162
<i>Stabilizing and focusing mechanism</i>	169
5.3. Slit-scanning fiber-optic imaging-bundle confocal microscope	170
<i>System design</i>	170
<i>Performance</i>	179
5.4. Applications	180
6. CONCLUSION	182
APPENDIX A. CONFOCAL MICROSCOPY REFLECTION	
TECHNIQUE FOR MEASURING THE INDEX OF REFRACTION OF	
OPTICAL FIBERS AND FIBER-OPTIC IMAGING BUNDLES	185
A.1. Introduction	185
A.2. Theory of the reflection method	188
A.3. Experimental method	200
A.4. Results	205
A.5. Conclusion	214
REFERENCES	215

LIST OF FIGURES

Figure 1.1.	Confocal microscope image of a tilted object.	17
Figure 1.2.	Optical layout of an (epi-illumination) confocal microscope.....	18
Figure 1.3.	Through-focus intensity distribution of a rotationally symmetric system with an evenly illuminated pupil.	20
Figure 1.4.	The fiber-optic imaging-bundle confocal microscope.....	22
Figure 2.1.	Optical sectioning in the confocal microscope.....	28
Figure 2.2.	Scanning optical microscope (non-confocal).	29
Figure 2.3.	Simulated optical-sectioning performance in a confocal microscope.....	32
Figure 2.4.	Optical sectioning in a confocal microscope with a slit detector.	38
Figure 2.5.	Simulated optical-sectioning performance in a confocal microscope with a slit detector.	39
Figure 2.6.	Comparison of simulated optical-sectioning performance in a confocal microscope with pinhole and slit detectors.....	40
Figure 2.7.	Telecentric optics for proper inspection of specular objects with a beam-scanning system.	43
Figure 2.8.	Confocal microscopy reflection (brightfield) image of the epidermis on the back of the author's hand (intact).	50
Figure 3.1.	Several core-clad refractive index profiles of optical fibers.....	52
Figure 3.2.	Meridional and skew rays in an optical fiber.....	53
Figure 3.3.	Bound and unbound rays in an optical fiber.....	54
Figure 3.4.	Integration of a beam by an optical fiber (assuming many modes).....	55
Figure 3.5.	Intensity pattern corresponding to the bound modes of a slightly hexagonal optical fiber.	57
Figure 4.1.	Idealized hexagonal arrangement of circular core fibers.....	68

LIST OF FIGURES - *Continued*

Figure 4.2.	Geometry of cores and cladding in a hexagonally-packed imaging bundle.	74
Figure 4.3.	Hexagonal close-packed fiber model used to estimate resolution.....	78
Figure 4.4.	Reflection images of small sections of three silica multi-core fiber-optic imaging bundles.....	85
Figure 4.5.	Index of refraction of small regions of a) Sumitomo Electric Corp. IGN-05/10, b) Fujikura Ltd. FIGH-03-300C, and c) Sumitomo Electric Corp. IGN-10/13 silica fiber-optic imaging bundles.....	93
Figure 4.6.	Refractive index profiles of a single core in each of three silica fiber-optic imaging bundles.....	97
Figure 4.7.	Intensity patterns corresponding to the bound modes of a fiber in a Sumitomo Electric Corp. IGN-05/10 0.35 NA fiber-optic imaging bundle.	104
Figure 4.8.	Predicted and measured coupling of collimated light into a Sumitomo Electric Corp. IGN-05/10 0.35 NA fiber-optic imaging bundle.	108
Figure 4.9.	Absence of crosstalk in a 2.5m long Sumitomo Electric Corp. IGN-05/10 fiber-optic imaging bundle.....	109
Figure 4.10.	Stray light and/or cladding modes in a Sumitomo Electric Corp. IGN-05/10 fiber-optic imaging bundle.....	111
Figure 5.1.	Fiber-optic confocal microscope (single fiber).....	114
Figure 5.2.	Modification of a commercial epi-illumination confocal microscope to include a fiber-optic imaging-bundle.....	116
Figure 5.3.	Comparison of confocal and non-confocal microscope images collected through a fiber-optic imaging bundle.....	117
Figure 5.4.	Optical-sectioning performance of the Zeiss LSM10 confocal microscope with and without a fiber-optic imaging bundle.....	130
Figure 5.5.	Optical-sectioning performance at the center of the field in the Zeiss LSM10 confocal microscope. Comparison of system with and without a fiber-optic imaging bundle.....	132

LIST OF FIGURES - *Continued*

Figure 5.6. Experimental setup for comparison of the optical- sectioning performance of a confocal microscope and a fiber-optic imaging-bundle confocal microscope.	134
Figure 5.7. Comparison of the optical-sectioning performance of a confocal microscope with and without a fiber-optic imaging bundle.	135
Figure 5.8. Semi-infinite fluorescent sample for evaluation of the fluorescence-mode optical-sectioning performance of a confocal microscope.....	136
Figure 5.9. Fluorescence-mode axial step response of the Zeiss LSM10 confocal microscope.	138
Figure 5.10. Average fluorescence-mode optical-sectioning performance over a region of the step response of Figure 5.9.....	140
Figure 5.11. Set of through-focus images of insulinoma cells collected with the Zeiss LSM10 confocal microscope.....	142
Figure 5.12. Set of through-focus images of insulinoma cells collected with the fiber-optic imaging-bundle confocal microscope.....	143
Figure 5.13. Images of a 15 μm diameter fluorescent microsphere.....	145
Figure 5.14. Intensity plots of the fluorescent microsphere images of Figure 5.13.	147
Figure 5.15. Intensity plot of light transmitted through an overfilled imaging bundle	148
Figure 5.16. Low signal-to-noise ratio image collected with the fiber-optic imaging-bundle confocal microscope and improved signal-to-noise ratio image obtained through line averaging.....	150
Figure 5.17. Confocal images of cancer cells (round objects) and fibroblasts (elongated objects).....	156
Figure 5.18. Telecentric (Fig 5.18a) and non-telecentric (Fig. 5.18b) distal imaging lenses.	160
Figure 5.19. Gradient index (GRIN) lens design	165
Figure 5.20. Performance of the GRIN lens design.....	166

LIST OF FIGURES - *Continued*

Figure 5.21. Preliminary design of a stabilizing and focusing mechanism	170
Figure 5.22. The slit-scanning fiber-optic imaging-bundle confocal microscope. System diagram.....	174
Figure 5.23. The slit-scanning fiber-optic imaging-bundle confocal microscope. Unfolded illumination path.	175
Figure 5.24. The slit-scanning fiber-optic imaging-bundle confocal microscope. Unfolded detection path.	176
Figure 5.25. Fluorescence images obtained with the slit-scanning fiber-optic imaging-bundle confocal microscope.....	180
Figure 5.26. Reflection image of a U.S. Air Force bar target obtained with the slit-scanning fiber-optic imaging-bundle confocal microscope.	181
Figure A.1. Reflected intensity versus refractive index of the transmitted medium, n_2 , for normal incidence.	190
Figure A.2. Diagram of theoretical model for calculating reflected intensity as a function of refractive indices, n_1 and n_2 , and numerical aperture, $n_1 \sin(\theta_i)$	191
Figure A.3. Reflected intensity in the exit pupil of the collection lens for an 0.85 NA aberration-free lens with $n_1 = 1.0$ and $n_2 = 1.5$	194
Figure A.4. Total reflected intensity as a function of numerical aperture	195
Figure A.5. Vignetting of the reflected beam by the collection lens due to a tilted surface.....	197
Figure A.6. Effect of surface tilt magnitude, α , and tilt orientation, ϕ_2 , on the total reflected intensity.	198
Figure A.7. Comparison of theoretical and experimental results for a 1.4 NA oil-immersion ($n_1 = 1.518$) lens.....	199
Figure A.8. Experimental setup for measuring the reflection of light from an interface in the focal plane of the objective lens.	201
Figure A.9. Experimental results of a set of reference samples and a second-order polynomial curve fit to the data.....	206

LIST OF FIGURES - *Continued*

Figure A.10. Index of refraction of a small region of a Sumitomo Electric Corp. IGN-05/10 silica fiber-optic imaging bundle (identical to Figure 4.5a).....	208
Figure A.11. Index of refraction of a small region of a Fujikura Ltd. FIGH-03-300C silica fiber-optic imaging bundle (identical to Figure 4.5b).....	209
Figure A.12. Index of refraction of a small region of a Sumitomo Electric Corp. IGN-10/13 silica fiber-optic imaging bundle (identical to Figure 4.5c).....	210
Figure A.13. Profiles through the cores of several silica fiber-optic imaging bundles.....	211

LIST OF TABLES

Table 4.1.	Specified parameters of three silica fiber-optic imaging bundles	91
Table 4.2.	Expected and measured parameters of three silica fiber-optic imaging bundles.	92
Table 4.3.	Average core spacing in three silica fiber-optic imaging bundles.	99
Table 4.4.	Packing fraction, average core diameter, and bound modes of three silica fiber-optic imaging bundles.	101
Table A.1.	Expected and measured parameters of three fiber-optic imaging bundles (identical to Table 4.2).	207

ABSTRACT

This dissertation describes the implementation of confocal microscopy through a fiber-optic imaging bundle. This system, the fiber-optic imaging-bundle confocal microscope, permits the optical-sectioning effect of confocal microscopy to be applied to a range of samples inaccessible to a conventional confocal microscope. Two such systems were designed and built. The first system is a modified laboratory microscope used to demonstrate and evaluate the performance of the fiber-optic imaging-bundle confocal microscope. The second system is a real-time slit-scanning microscope that is expected to be a suitable design for in-vivo medical applications.

Fiber-optic imaging bundles are discussed in some detail. A number of parameters of three flexible silica imaging bundles were measured and the suitability of these bundles for use in the microscope is evaluated. A new reflection technique for measurement of optical-fiber refractive indices was developed and applied to the evaluation of these imaging bundles.

1. INTRODUCTION

1.1. Overview of confocal microscopy

Confocal microscopy is an optical technique that allows for visualization of thin slices within a thick object, expanding the usefulness of microscopy from two to three dimensions. This effect is called optical sectioning, and is the result of simultaneous imaging of a point-source and a point-detector onto a single point in the sample.

Minsky first proposed the confocal microscope in a 1957 patent application.¹ He pointed out some of the fundamental advantages of confocal microscopy, particularly the ability to examine thick specimens.

Neglecting aberrations, the intensity near the image of a point source will be the greatest at the geometric image of the point. Equivalently, the coupling of light from the sample to a point detector will be optimum from the point in the sample conjugate to the detector. Aligning the images of a point source and a point detector in the sample plane yields a sensitivity to the attributes of the sample at this point (scattering or fluorescence) that falls off quickly in both lateral and axial directions. Optical sectioning is the axial variation in sensitivity, and in high numerical-aperture confocal systems can result in an axial slice thickness as small as one-half of the wavelength (full-width at half-maximum).²

Figure 1.1 demonstrates the optical-sectioning effect in studying the reflection of light from the face of a fiber-optic imaging bundle. The bundle face is at an angle (upper left to lower right), resulting in only a strip in the middle being visible in the image. The regions of the object above and below the focal plane have been "sectioned"

away, leaving only the in-focus region visible. This differs from more conventional forms of microscopy in which both in-focus and out-of-focus object planes contribute to the image, producing blurred images of thick objects (see, for example, Figures 5.25a and 5.25b).

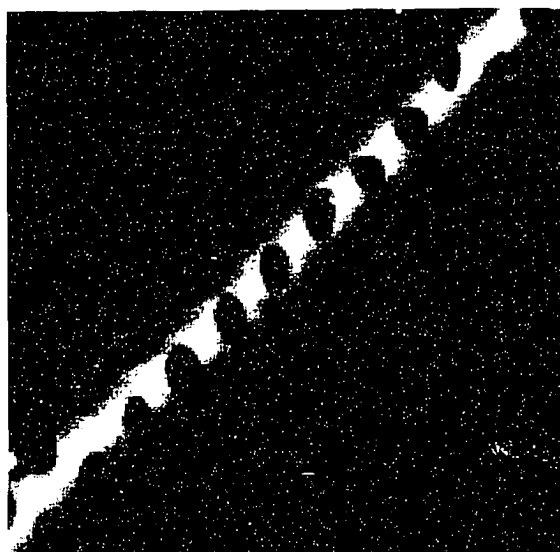


Figure 1.1. Confocal microscope image of a tilted object. The upper left and lower right portions of the object are above or below the focal plane, and have been removed from the image by the optical-sectioning effect.

The optical layout of a confocal microscope is shown in Figure 1.2. For regions of the sample that are above or below the focal plane, both the illumination and detection efficiency are reduced, resulting in a drop in sensitivity to these regions. The

reduction in sensitivity with defocus is a function of the numerical aperture of the objective and the size of the source and detection "point" images (neither one can be exactly a point due to the need to pass light). Higher numerical apertures and smaller source and/or detector images all result in a quicker falloff with defocus.

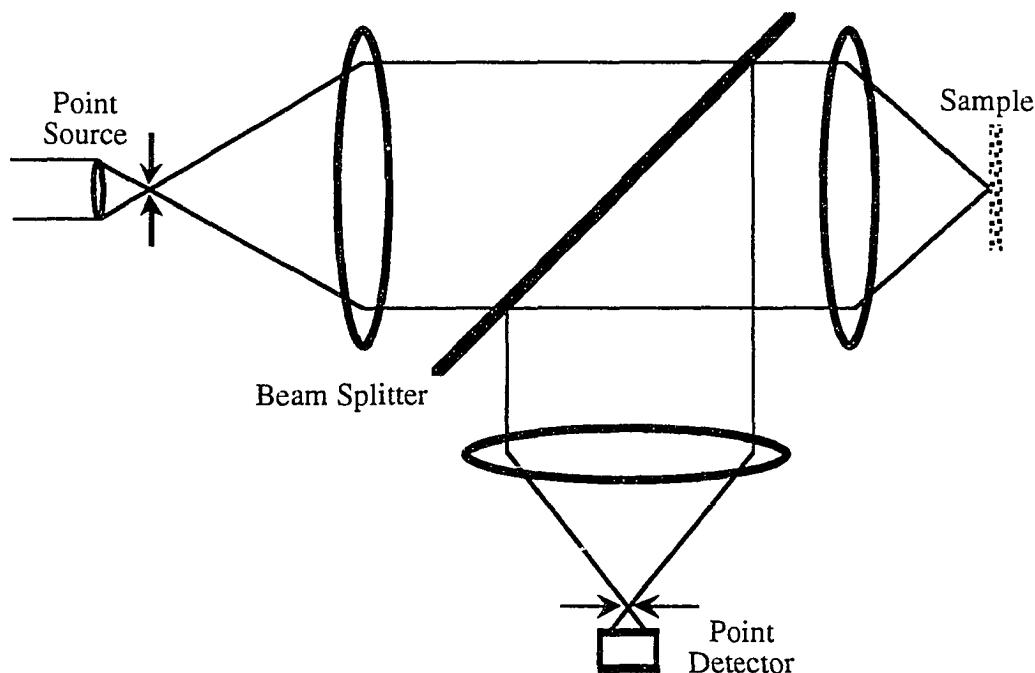


Figure 1.2. Optical layout of an (epi-illumination) confocal microscope.

As seen in Figure 1.2, the confocal microscope measures the properties of a single object point. This is necessary to preserve the optical-sectioning effect, and requires scanning to form an image of a finite field-of-view. Minsky originally envisioned a system where the object is scanned in three dimensions through the desired field-of-

view. Alternatively, the object may be held fixed and the source and detection pinhole images scanned through the desired field-of-view.

Figure 1.3 shows the through-focus intensity distribution in the image of the point-source or point-detector (often called the three-dimensional point-spread-function), including the effects of diffraction, but not aberrations, for a rotationally symmetric system with an evenly illuminated pupil. This is a planar slice through the three-dimensional intensity distribution; one axis, z , is along the optical axis, while a second axis, x , is perpendicular to the optical axis. Assuming the source and detection lenses have identical properties, the fluorescence-mode intensity point-spread-function (PSF) of the confocal microscope is approximately the square of the point-spread-function of Figure 1.3. The resulting point-spread-function of the confocal system is smaller than that shown in Figure 1.3, indicating the confocal microscope's ability to resolve finer detail than a system relying on the resolution of the illumination or collection arm alone. Analysis of the reflection (scattering) case is more complicated due to the potential for interference between light scattered from different object points.

It is also possible to simultaneously scan multiple source and detection pinhole images across the sample. This results in essentially the same image forming properties as the confocal microscope as long as the pinhole spacing is large enough to prevent significant crosstalk. Crosstalk occurs if a detection pinhole collects light from a source pinhole other than the one with which it is confocal.

It is important to note that while this discussion provides a general indication of the advantages of confocal microscopy, it does not address important issues such as

signal-to-noise ratio (SNR), imaging time, and fluorescence saturation or bleaching, which may prohibit the use of a confocal system. For a particular application, it is incorrect to assume that a confocal system will always be superior to a conventional imaging system. Also, it can be misleading to compare a confocal microscope with a "conventional" microscope because there are many different types of optical microscopes with a variety of different imaging characteristics.

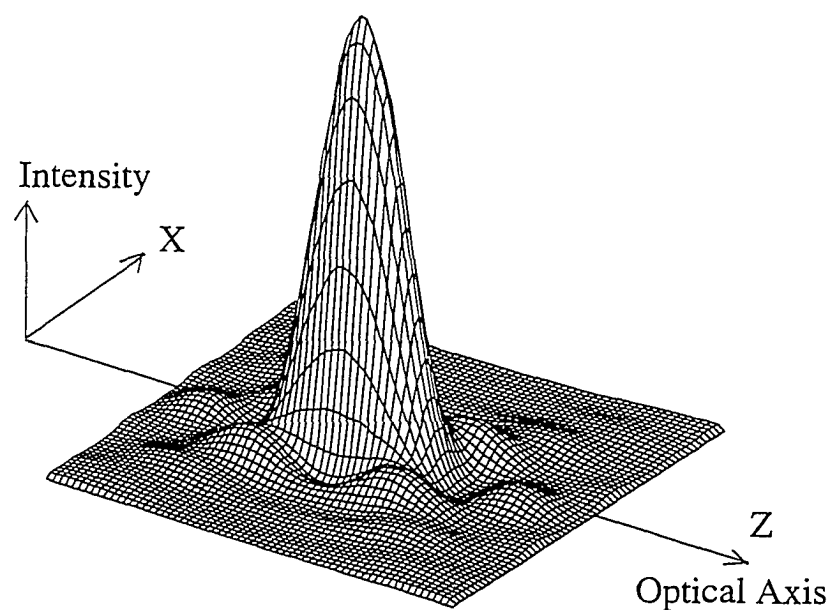


Figure 1.3. The through-focus intensity distribution of a rotationally symmetric system with an evenly illuminated pupil. Includes the effects of diffraction but no aberrations.

The majority of applications of confocal microscopes are in the biological sciences, where they are used to examine cellular and sub-cellular structures. Most samples are tagged with fluorescent dyes and may be fixed on microscope slides, in cell cultures, or even in live specimens. Confocal microscopes are also used in industrial inspection tasks such as the analysis of semiconductors. The optical-sectioning effect is the usual reason for using a confocal system in order to study the three-dimensional structure of the sample.

1.2. Motivation for a fiber-optic imaging-bundle confocal microscope

Confocal microscopy is generally performed with modified laboratory microscopes. This typically limits the range of potential samples to those that can be placed on a microscope stage and inspected with conventional microscope objectives, making in-vivo medical application unrealistic in most cases.

A recent technique has been to use an optical fiber as the source and/or detection pinhole, allowing greater flexibility in sample location.^{3,4,5,6} While this allows a compact scan head and has been applied to in-vivo problems,^{7,8} such a system requires mechanical scanning in the region of the sample and, therefore, a sophisticated mechanical apparatus.

As an enhancement of confocal microscopy, we have included a fiber-optic imaging bundle into the optical path of the imaging system (see Figure 1.4). This allows the inspection of any sample that can be reached with the end of the fiber bundle. The advantage of this system over the single-fiber system is that the scanning mechanism no longer needs to be located at the distal end of the fiber. This is because the imaging

bundle transmits the entire field rather than a single field point. However, the properties of the imaging bundle now affect the spatial resolution, field-of-view, and radiometric performance of the system. Significantly, the imaging of the system is no longer space-invariant, making analysis of the image-formation process rather complicated. There is a range of point-spread-functions, and, therefore, no single modulation-transfer-function (MTF), associated with the system.

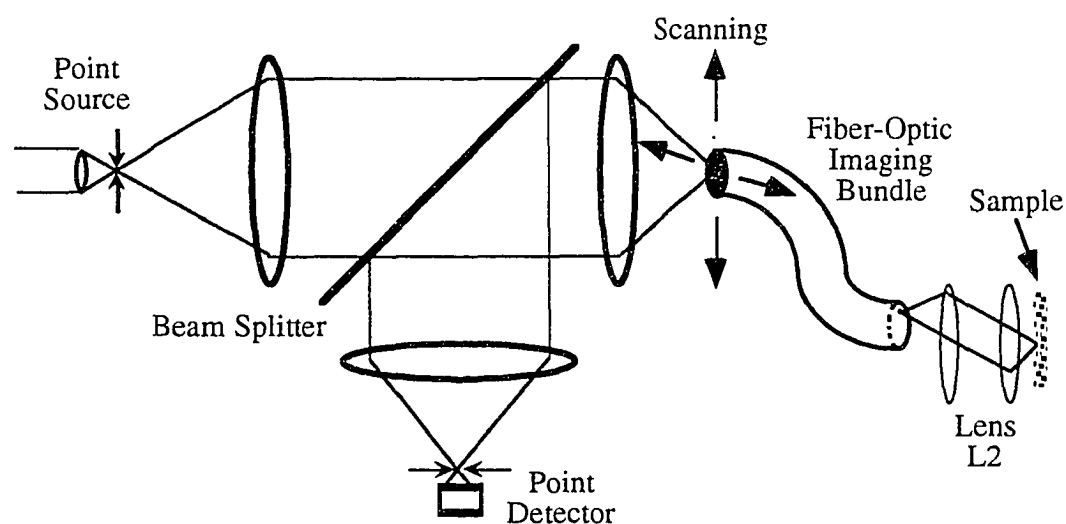


Figure 1.4. The fiber-optic imaging-bundle confocal microscope.

Fiber-optic imaging bundles are available in various lengths, thicknesses, resolutions, flexibilities, and materials. All the fiber-optic imaging-bundle confocal microscope images presented in this work were collected through a 10,000 fiber silica imaging bundle of 0.5 mm diameter (4.4 μm center-to-center spacing and 3.4 μm core diameter of the fibers).

The most exciting potential application of the fiber-optic imaging-bundle confocal microscope is examination of areas of the human body that can be reached directly, through body orifices, or percutaneously. The main obstacles to a successful system are development of adequate distal imaging optics and a positioning, stabilizing, and focusing mechanism at the distal end of the fiber bundle. This requires a compact, manipulable fiber bundle and probably a focusing and/or zooming distal objective. While suitable fiber bundles are commercially available, the distal imaging system must be designed and built specifically for this application. A catheter-based system will be difficult to build due to the size limitations, particularly on the diameter of the distal imaging system. The fiber-optic imaging-bundle confocal microscope images presented in this work were collected with conventional microscope objectives serving as the distal objective. Such objectives are clearly too large to be of use for an in-vivo system, but give some indication of potential imaging performance.

The use of confocal microscopes in semiconductor metrology and other industrial applications may also benefit from increased flexibility in the imaging system. Good performance in these applications may be easier to achieve than in in-vivo medical applications due to less stringent constraints such as mechanical size and catheter sterilizability.

1.3. Scope and organization of this work

The goal of this work is to study the implementation of confocal microscopy through fiber-optic imaging bundles and to assess the imaging performance of this type of confocal microscope. The work includes a discussion of the image formation process

in the fiber-optic imaging-bundle confocal microscope, and a comparison of its performance with that of a comparable confocal system without an imaging bundle. Both point-scanning and slit-scanning confocal microscopes were built, analyzed, and evaluated. While the point-scanning system offers the highest axial resolution, the slit-scanning system has advantages in light collection and speed, which will be important for in-vivo medical applications.

The dissertation is organized as follows. Confocal microscopy is described in chapter 2. Optical fibers and fiber-optic imaging-bundles are described in chapters 3 and 4, respectively. The fiber-optic imaging-bundle confocal microscope is described in chapter 5, and experimental results with two microscopes are presented. Chapter 6 contains conclusions and directions for future work. A new refractive index measurement technique that is used in the analysis of several silica imaging bundles is described in appendix A.

2. CONFOCAL MICROSCOPY

As described in the preceding chapter, confocal microscopy allows for visualization of thin slices within a thick object. This so called optical-sectioning effect comes about due to the simultaneous (confocal) imaging of a point source and a point detector onto a single point in the sample. These point images are scanned through the field-of-view to build up a complete image of the sample.

2.1. Optical sectioning (axial resolution)

The optical-sectioning effect permits the formation of a three-dimensional image without the need for the difficult process of mechanical sectioning of the object, examination of each section, and then assembly of the resulting images to form a composite image. In many cases, it is not possible to perform this mechanical sectioning without altering the sample. For example, it is difficult to obtain a set of thin histological sections from a thick sample without some variation in the orientation, thickness, and shrinkage or stretching of the sections. Thus, confocal microscopy makes examination of some thick objects easier and more accurate.

Optical sectioning was demonstrated in Figure 1.1, where out-of-focus portions of a tilted sample are completely removed from the image. Moving (focusing) the sample axially will bring other regions of the sample into focus. A composite image of the sample can be formed by adding together a through-focus set of images. This would not be possible in conventional forms of microscopy where both in-focus and blurred out-of-focus portions of the image are visible, resulting in much more background noise in the composite image.

Figure 1.2 shows one possible optical layout of a confocal microscope. The point source is focused onto a specific point in the sample, illuminating this point and a small region surrounding it. The point detector (implemented with a pinhole in front of a detector) is simultaneously imaged onto the same spot in the sample. Portions of the object that are not located in the image of the point source are not only minimally illuminated, but are also out-of-focus at the detector pinhole, so that most of the signal from them does not reach the detector. This can be described with a geometrical model, as shown in Figure 2.1 for a defocused on-axis point object. Solid lines in this figure show imaging of the source and detection pinholes into the sample region. Dashed lines show coupling of the light from an out-of-focus point (on-axis) to the detector. The illumination beam is out-of-focus at the object. In the geometrical optics limit, the illumination intensity varies as $1/z^2$, where z is the defocus distance. The detection sensitivity is proportional to the ratio of the areas of the detector pinhole and the defocused image of the point object at the detector pinhole. This also varies as $1/z^2$, yielding a combined intensity point-response that varies as $1/z^4$.

The total signal collected from out-of-focus planes in a confocal microscope varies as $1/z^2$ due to the range of lateral positions that contribute to the image. This is obtained from the detected intensity per point that varies as $1/z^4$, in conjunction with the range of lateral positions contributing to the image that varies as z^2 (see Figure 2.1).

The optical-sectioning effect does not occur in the non-confocal scanning microscope shown in Figure 2.2. Solid lines in this figure show imaging of the source pinhole into the sample region. Dashed lines show coupling of the light from an out-of-focus point

(on-axis) to the detector. The illumination intensity at any point varies as $1/z^2$ in this system. The large-area detector, on the other hand, collects the same amount of light from all axial positions (an idealized condition that is accurate for moderate amounts of defocus). The total signal collected from in-focus and out-of-focus planes is the same due to the z^2 dependence of the range of lateral positions contributing to the image, combined with the $1/z^2$ intensity response. Thus, the detection sensitivity is independent of defocus. Out-of-focus portions of a thick sample are coupled to the detector in the form of a blurry background signal, resulting in a fuzzy image.

A complete description of the optical-sectioning performance of a confocal microscope includes the effects of diffraction. The thickness of the optical section is determined by the three-dimensional point-spread-functions of the illumination and collection arms, in conjunction with the sizes of the source and detection pinholes. The depth-of-focus of a slow optical beam is much larger than that of a fast optical beam, resulting in a thicker optical section. The size of the source and detection pinhole images at the sample are important because the light throughput can be improved by increasing the pinhole sizes, albeit at the expense of reduced optical-sectioning performance. For laser scanning systems, the source-pinhole image is typically diffraction limited, while the detection-pinhole image size may be made somewhat larger to collect adequate signal.

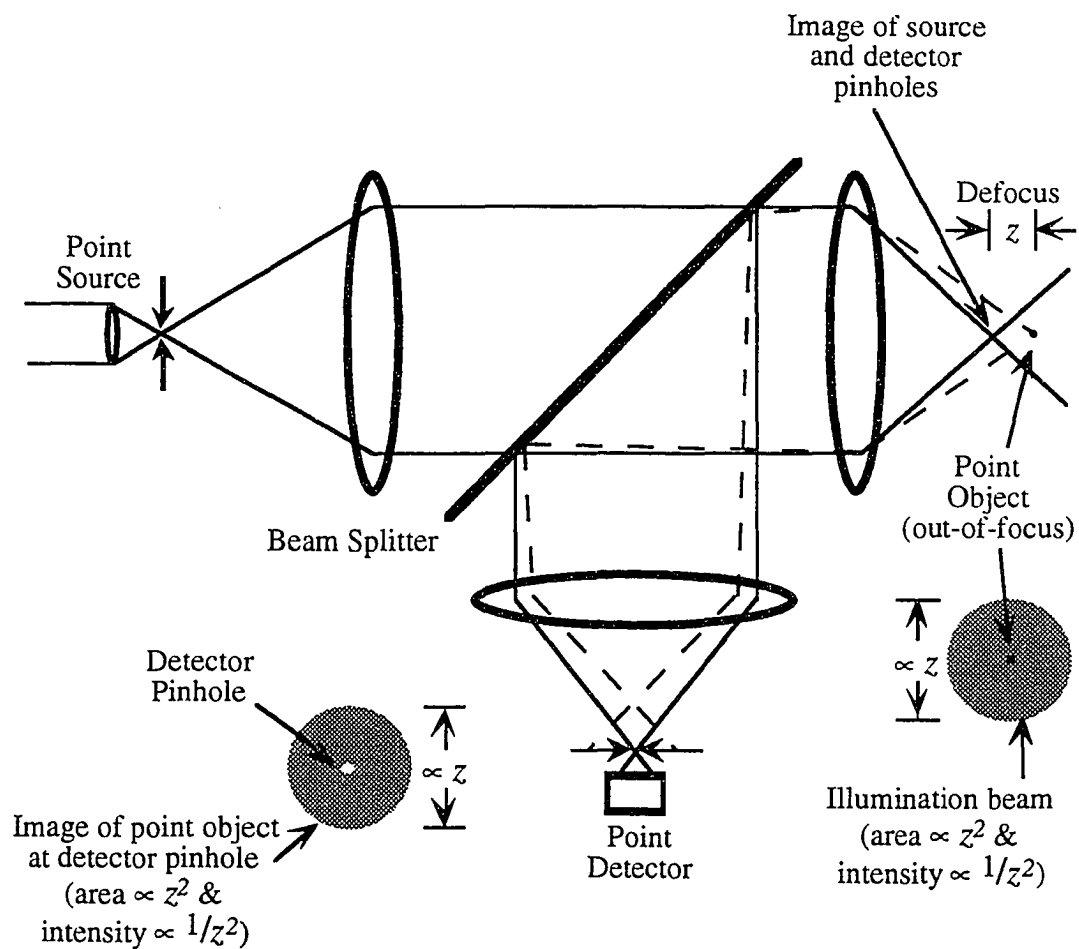


Figure 2.1. Optical sectioning in the confocal microscope. Solid lines in this figure show imaging of the source and detection pinholes into the sample region. Dashed lines show coupling of the light from an out-of-focus point (on-axis) to the detector.

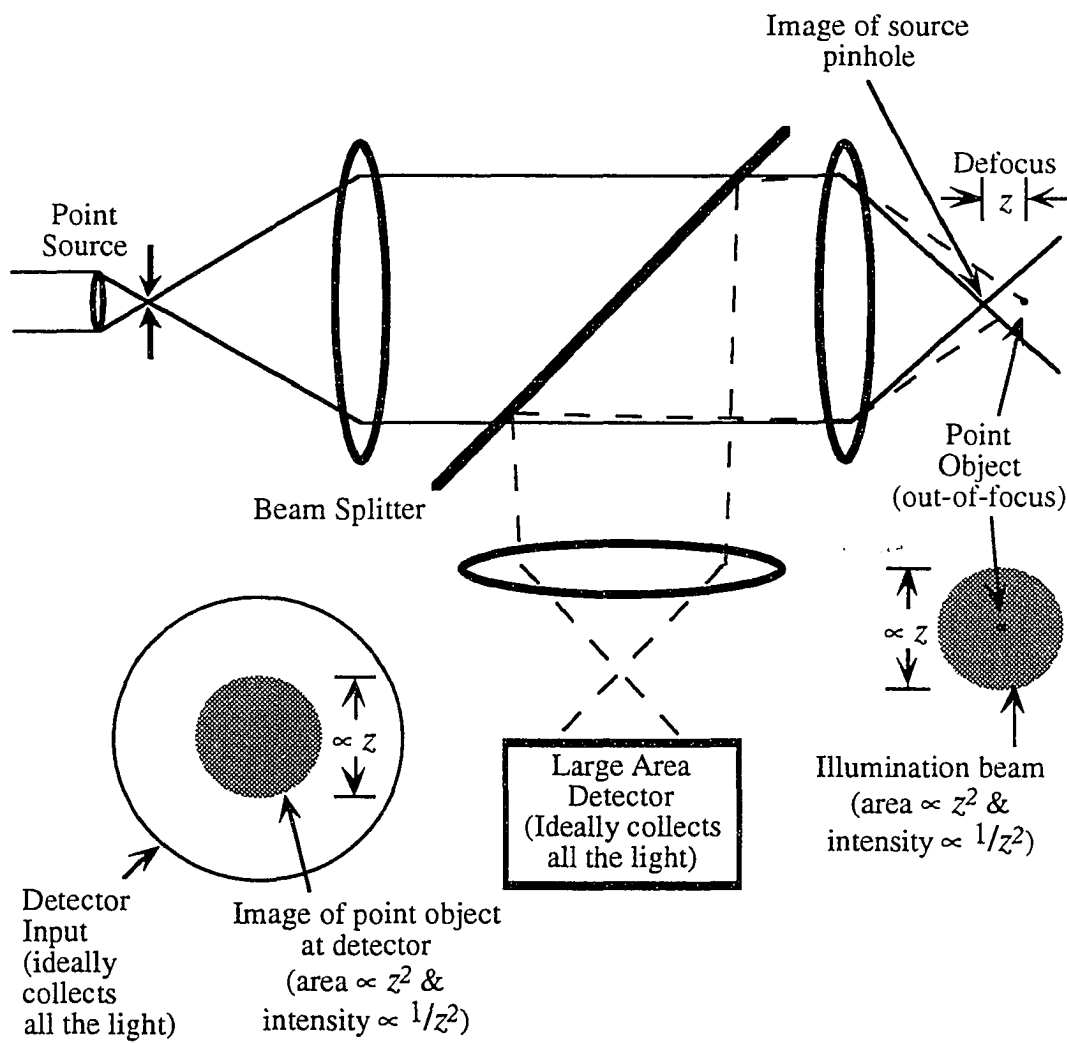


Figure 2.2. Scanning optical microscope (non-confocal). Solid lines in this figure show imaging of the source pinhole into the sample region. Dashed lines show coupling of the light from an out-of-focus point (on-axis) to the detector.

The on-axis intensity point response (including diffraction) of the non-confocal scanning optical system of Figure 2.2 is⁹

$$I \propto \text{sinc}^2\left(\frac{NA^2}{2\lambda}z\right) \quad (2.1)$$

where $\text{sinc}(x) = \sin(\pi x)/(\pi x)$, NA is the numerical aperture, λ is the wavelength, and z is the defocus of the object point. This is the on-axis intensity variation in the focal region of a lens, as shown in Figure 1.3.

The on-axis intensity point response of an ideal confocal microscope (point source and point detector) is^{10,11}

$$I \propto \text{sinc}^4\left(\frac{NA^2}{2\lambda}z\right). \quad (2.2)$$

The point response of the source and detection arms have combined to yield this faster decrease in sensitivity with axial displacement. The detector aperture diameter can be increased to collect more signal. This results in an increase in the size of the axial point response until it reaches the case of equation (2.1).

One common method of assessing the axial resolution of a confocal microscope is to scan a plane-object axially through focus.² With the non-confocal microscope of Figure 2.2, this will result in no variation in signal intensity, as long as the detector is big enough to capture all the reflected or fluorescent light (an idealized condition).

The ideal confocal microscope will produce a response to a plane mirror scanned through focus (in the paraxial approximation) of

$$I = \text{sinc}^2\left(\frac{u}{2\pi}\right) \quad (2.3)$$

where

$$u = \frac{8\pi}{\lambda} \sin^2\left(\frac{\alpha}{2}\right) z \quad (2.4)$$

and α is the half-angle of the beam in the object space ($NA = n\sin(\alpha)$).¹² This differs somewhat from the definition of Born and Wolf,⁹ and is accurate for larger numerical apertures.¹³ The simulated response to a plane mirror scanned through focus is shown in Figure 2.3 for a variety of detector pinhole sizes. The pinhole radius is often written in terms of the normalized parameter

$$v_p = \frac{2\pi}{\lambda} \sin(\alpha) r_p \quad (2.5)$$

where r_p is the radius of the pinhole.¹² The ideal confocal microscope has $v_p = 0$ for both the source and the detector. The axial response for $v_p = 0$ shows the expected sinc^2 behavior.¹² Larger values of v_p produce progressively worse optical-sectioning performance. The condition $v_p = \infty$ corresponds to the non-confocal case shown in Figure 2.2 and results in a constant response to a plane mirror scanned through-focus. The responses shown in Figure 2.2 have been normalized to the same peak value, although the large detector pinholes actually collect more light than the small detector pinholes.

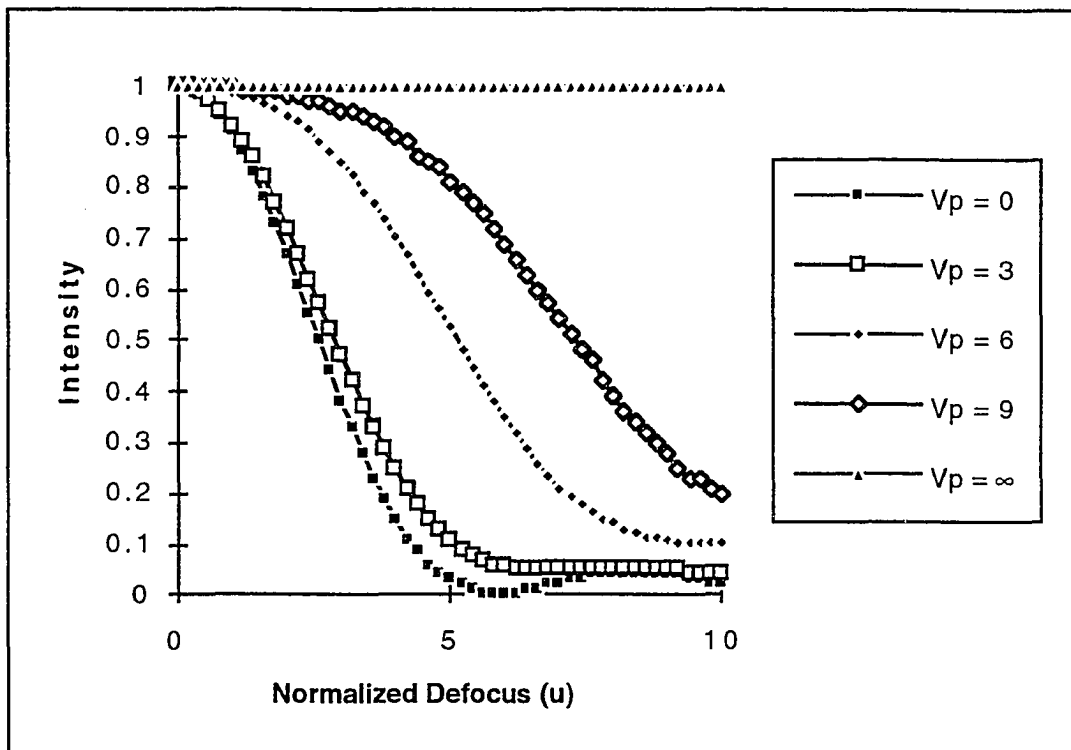


Figure 2.3. Simulated optical-sectioning performance in a confocal microscope. The detected intensity for a plane mirror scanned through focus is shown. The performances with normalized pinhole radii of $v_p = 0, 3, 6, 9$, and ∞ are shown (see legend).

A planar fluorescent object scanned through focus produces a signal that does not go to zero in the $v_p = 0$ case, and which is somewhat broader than the curves shown in Figure 2.3.¹² This is due to the incoherence of the fluorescence emission from the sample. The response is further degraded by the wavelength shift between the fluorescence-excitation and the fluorescence-emission.

2.2. Lateral resolution

The lateral resolution of a confocal microscope is determined by the lateral dimensions of the images of the "point" source and "point" detector. In general, these images are non-ideal, having finite size in order to pass light. The geometrical images of these points in conjunction with the point-spread-functions of their respective imaging systems determine their images in the sample plane. The complete point-spread-function is obtained by multiplying together the source and detection point-spread-functions.

In the ideal case of infinitesimal point source and point detector, the combined diffraction-limited images in the sample plane will yield a smaller point-spread-function than that from a single diffraction-limited beam of the same numerical aperture. For the case of identical source and detection point-spread-functions this will yield an overall point-spread-function that is narrower in the ideal confocal system by a factor of approximately 1.4 (assuming an Airy function diffraction pattern).² This is the source of the idea that confocal microscopy yields higher lateral resolution than forms of microscopy in which the resolution is determined by either the illumination or collection arm, with the other arm having minimal effect. Unfortunately, this effect is quickly lost due to the finite pinhole sizes often necessary to obtain adequate signal, and thus may not represent a realizable gain.

2.3. Modes of operation

Confocal microscopes have a number of operating modes, including trans-illumination and epi-illumination, brightfield and fluorescence.

Trans-illumination

In the trans-illumination mode, the sample is illuminated from one side and the scattered or fluorescent light detected on the other side. If no sample is present, the light passes through focus unperturbed and the maximum amount of light reaches the detector for each scan position. Thus, it is the scattering or absorption of light that denotes an effect due to the sample. This poses difficulties, as unscattered illumination light will be detected as background noise, making the detection of faint objects difficult. When operated in the fluorescence mode, filtering out the excitation wavelengths reduces this problem.

The advantages of confocal microscopy come from the combined imaging properties of the illumination and collection arms. Unfortunately, this makes the aberrations present in both arms important. Thus, in trans-illumination operation, two sets of high-quality optics (illumination and collection) are necessary to obtain good imaging performance.

Epi-illumination

In epi-illumination, a single objective acts as the final imaging optic in both the illumination and collection arms, eliminating the need for two high-quality objectives. Implementations of the fiber-optic imaging-bundle confocal microscope are likely to operate in epi-illumination due to the difficulty of positioning fiber bundles on opposite sides of the sample. This will be the case with most in-vivo medical applications as well as industrial applications such as semiconductor metrology.

Brightfield

In the brightfield mode, images are formed with the light scattered from the sample. In an epi-illumination system, this is the light back-scattered from the object through the detection pinhole.

Since the confocal microscope operates ideally with a point source, the brightfield mode is inherently coherent. This is the case even for a non-monochromatic source because light emitted by a point source will always be able to interfere with itself for zero optical-path-length difference. In a real system, where a finite-sized detector pinhole is necessary to collect adequate signal, the imaging becomes partially coherent.

Fluorescence

The fluorescence mode is implemented by exciting a fluorescent sample at one wavelength range and collecting the fluorescent light over some range of longer wavelengths. The excitation wavelengths are typically eliminated from the detected signal by a dichroic beam-splitter and/or a long-wave pass filter. In contrast to the brightfield mode, the fluorescence mode is inherently incoherent, as the detected signal is proportional to the signal intensity at the sample, rather than the signal amplitude.

2.4. Detectors

The ideal confocal microscope uses a point detector. In real systems, however, this detector must have finite size to collect light, with there being an inverse relationship

between signal and resolution (larger pinholes yield poorer resolution). Additionally, alternative pinhole geometries such as slits may be implemented to modify the system performance as desired. Array detectors can also be used to simplify postprocessing of the data, as discussed below.

Pinhole detector apertures

Point (pinhole) detectors are often implemented by a small circular aperture in front of an optical detector, typically a photo-multiplier tube. The pinhole is positioned so that its image is coincident in the sample with the source pinhole image. As discussed above, the system resolution (axial and lateral) is a function of the size of the pinhole images, and, therefore, the physical size and magnification of the detector pinhole.

In order to take full advantage of the optical-sectioning effect, the detection pinhole must eliminate much of the light collected from the sample, which generally results in low signal levels. This can be remedied by increasing the diameter of the detection pinhole, whereby more light is collected at the expense of resolution. However, background noise will also increase, resulting in the need for a careful choice of pinhole size to optimize image quality for a particular application.^{2, 14}

The signal-to-noise ratio (SNR) of the microscope can be improved by averaging multiple frames or reducing the scan rate. For random noise, increasing the signal collection time by either of these techniques will be advantageous because the signal adds constructively while random noise does not. The SNR increases by the square root of the sampling time, so if the scanning is slowed by a factor of four, or if four frames are averaged, the SNR will improve by a factor of two. It may not be possible

to implement either of these techniques due to sample motion, fluorescence saturation, or fluorescence bleaching. Fluorescence saturation and bleaching are temporary or permanent reductions in the fluorescence efficiency of a material due to excessive illumination intensity.

Slit detector apertures

Slit detectors can be used in confocal microscopy as a compromise between signal strength, imaging time, and resolution. Confocal images often have low signal levels, such as might be the case in observing a weakly fluorescent object. Increasing the diameter of a pinhole detector sufficiently to obtain adequate signal may yield unacceptably poor optical sectioning. The slit detector maintains the confocal behavior of the system only in the direction perpendicular to the slit.¹⁵ This results in a different optical-sectioning performance between the pinhole and the slit, and can yield a stronger signal without a significant loss in axial resolution (but not necessarily increased SNR).¹⁶

The effect of pinhole versus slit detectors can be explained qualitatively with a geometrical optics description. The slit detection aperture produces a $1/z$ reduction in detection sensitivity to an out-of-focus point object, as shown in Figure 2.4.

Combined with the $1/z^2$ reduction in illumination intensity, as described above for Figures 2.1 and 2.2, this produces an overall $1/z^3$ intensity point-response on-axis. This falls between the $1/z^4$ point-response of the confocal system of Figure 2.1 and the $1/z^2$ point-response of the non-confocal system of Figure 2.2. The intensity signal from a plane mirror scanned through focus will vary as $1/z$, rather than the $1/z^2$

variation described above for the ideal confocal system with a point source and a point detector.

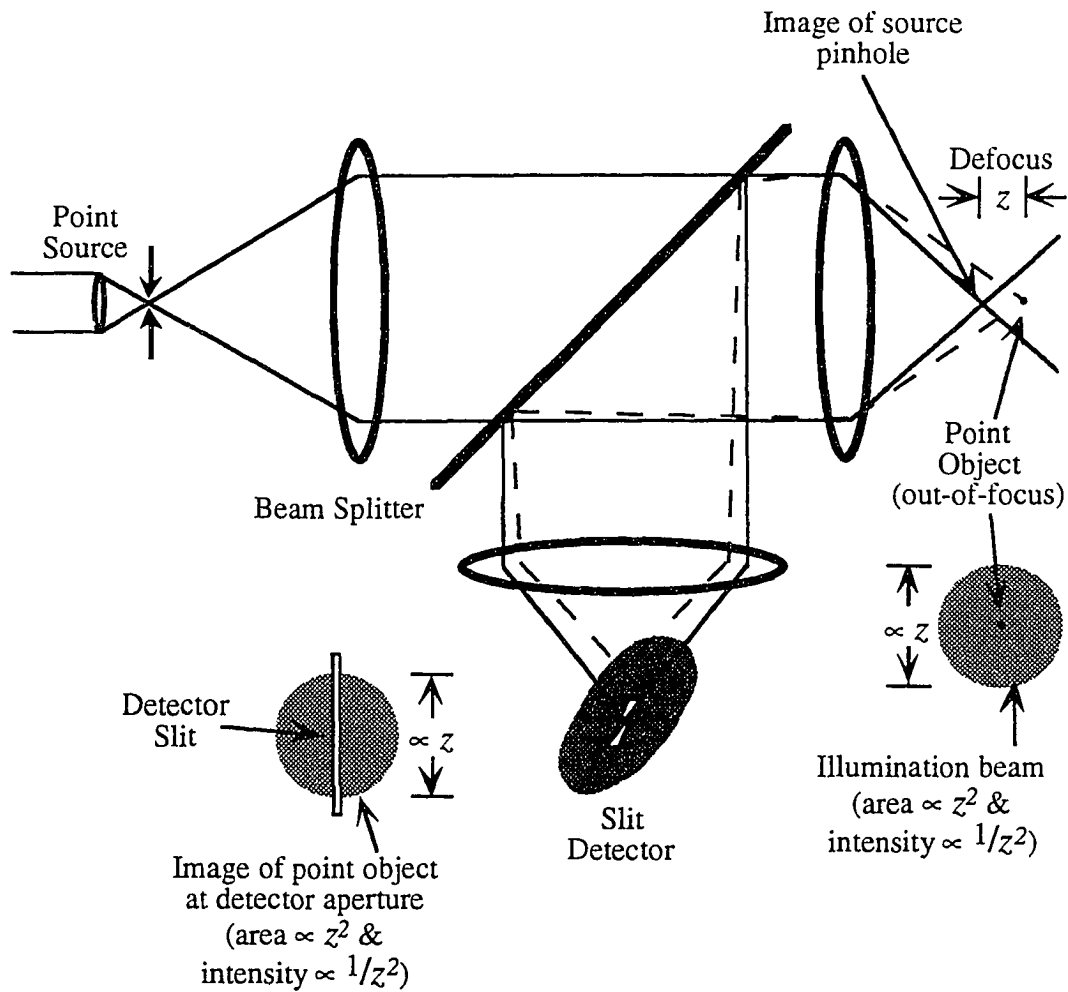


Figure 2.4. Optical sectioning in a confocal microscope with a slit detector. Solid lines in this figure show imaging of the source and detection apertures into the sample region. Dashed lines show the coupling of light from an out-of-focus point (on-axis) to the detector.

The simulated response (including diffraction) to a plane mirror scanned through focus is shown in Figure 2.5 for a variety of slit widths. The slit half-width has been used in place of the pinhole radius, r_p , in equation (2.5) to calculate the value of the normalized aperture parameter, v_p . The responses have been normalized to the same peak value, although the wide slits (such as $v_p = 5$) actually collect more light than the thin slits (such as $v_p = 1$).

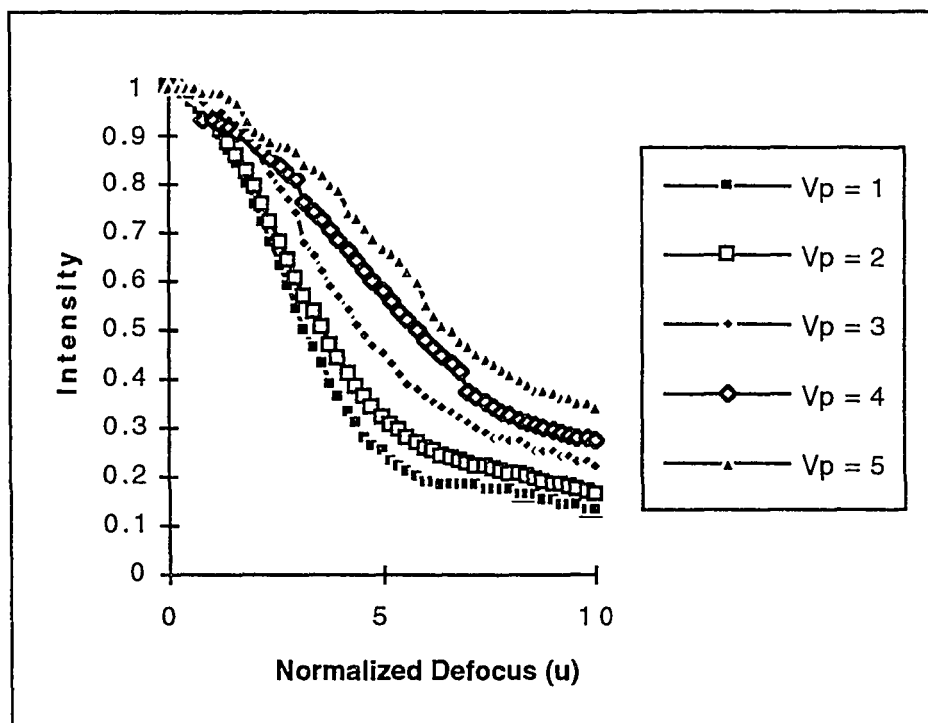


Figure 2.5. Simulated optical-sectioning performance in a confocal microscope with a slit detector. The detected intensity for a plane mirror scanned through focus is shown. The performances with normalized slit widths of $v_p = 1, 2, 3, 4$, and 5 are shown (see legend). The small jumps visible in the $v_p = 3, 4$, and 5 curves are due to the an inadequate number of points in the sampling array, and are not an attribute of the slit detector.

The simulated optical-sectioning performance (response to a plane mirror scanned through focus) for pinhole and slit detectors is compared in Figure 2.6 for the cases of $v_p = 1$. The $v_p = 1$ slit detector case does not have the sinc^2 behavior seen with the $v_p = 1$ pinhole detector (the responses with $v_p = 1$ and $v_p = 0$ pinhole detectors are almost identical). As expected, the pinhole detector provides somewhat better axial resolution. However, the peak signal with the slit detector is approximately twice as strong as the peak signal with the pinhole detector.

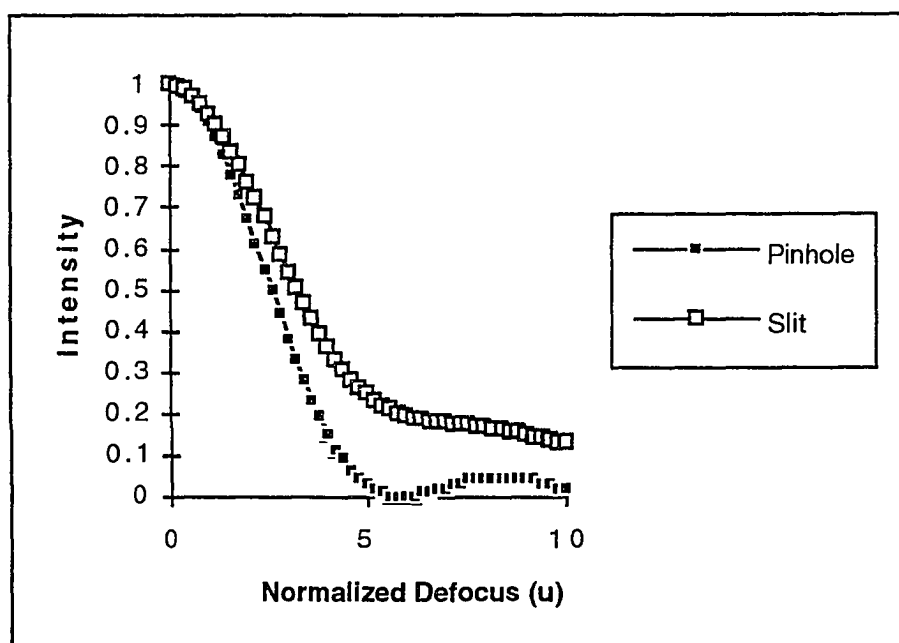


Figure 2.6. Comparison of simulated optical-sectioning performance in a confocal microscope with pinhole and slit detectors. The detected intensity for a plane mirror scanned through focus is shown. $v_p = 1$ in both cases, where r_p is the pinhole radius or slit half-width.

Array detectors

Image acquisition in confocal microscopes is typically done sequentially as the pinhole images are scanned across the object, with the final image being reconstructed with a computer. A slit-scanning system (described below) with a linear array detector performs in much the same fashion with the exception that data are collected a row at a time.

Alternatively, the image can be acquired with an area detector such as a CCD camera. This is done by scanning the light passing the detection aperture (pinhole or slit) across the CCD camera simultaneously with the scanning of the detection aperture image across the sample. The CCD camera is allowed to integrate during the entire scan time, eliminating the need to reconstruct the image. This technique is used in the real-time slit-scanning system described in chapter 5.

Array detectors have also been proposed in order to take advantage of the light normally eliminated by the pinhole, under the assumption that the light falling outside the pinhole aperture contains additional information about the object under examination.¹⁷

2.5. Scanning techniques

Since the confocal microscope detects only a single point (or line) within the sample at a time, scanning is necessary to form an image. This can be accomplished by scanning either the sample through the beam or the beam through the sample. The scanning is not limited to transverse planes within the sample, but rather can be

performed in any desired orientation in two or three dimensions. Thus, it is possible to obtain with confocal microscopy a two-dimensional view with arbitrary orientation, or even a three-dimensional view of the sample.

Object (stage) scanning

The simplest means of scanning in confocal microscopy is to leave the optical system fixed and scan the sample in the x , y , and z directions through the region of interest. The main advantage of object scanning is that imaging is performed at a single, on-axis, field point. This yields space-invariant imaging in each transverse plane and allows optimization of the optical system for a single field point, simplifying the optical design. The field-of-view in an object-scanning system is determined by the physical scan mechanism and is independent of the magnification. The main drawback of object scanning is the limitation to slow-scan systems (several seconds) due to the mass of the specimen stage.

Objective scanning

Objective scanning systems are implemented by scanning the objective(s) in lateral and axial directions to move the source and detection pinhole images through the sample. Image formation in this system is nearly on-axis (scanning the objective laterally is simply moving the axis), simplifying the optical design. The image-acquisition speed is limited by how fast the objectives can be scanned through the desired range. Many confocal microscopes are built by modifying standard laboratory microscopes. Since such systems are not easily modified to allow scanning of the objectives, objective scanning is rare in commercial systems.

Beam scanning

Beam scanning is implemented with several techniques, including galvanometer mirrors, Nipkow disks, acousto-optic cells, and rotating polygon mirrors. The source and detection beams need to be scanned in unison, making this design generally more applicable to epi-illumination systems than trans-illumination systems. It is necessary to use a telecentric system in beam-scanning microscopes for proper examination of specular objects, as shown in Figure 2.7.¹¹

Since beam-scanning systems include off-axis imaging, aberration-correction of the optical design is necessary for multiple field positions. The fiber-optic imaging-bundle confocal microscope includes off-axis imaging, which will need to be addressed in the design of the distal optics.

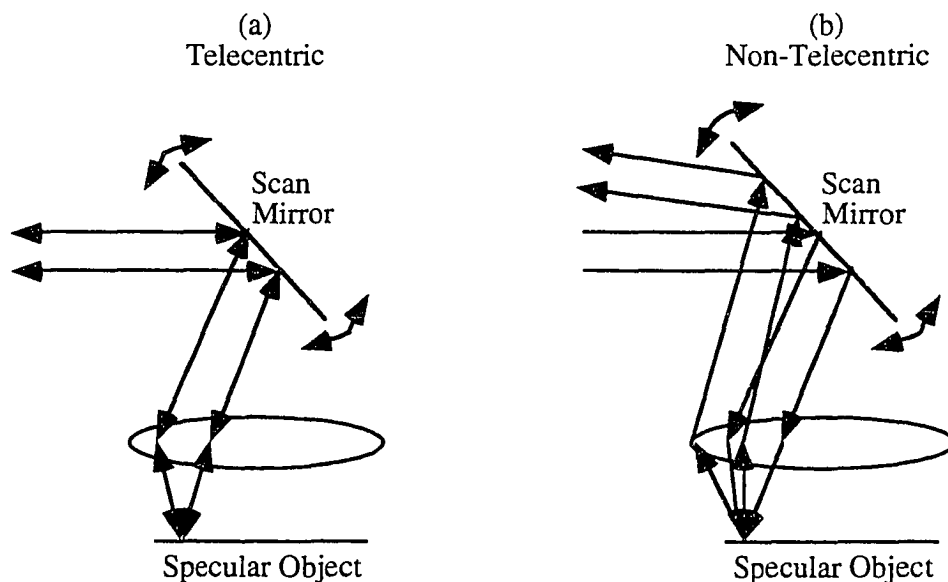


Figure 2.7. Telecentric optics for proper inspection of specular objects with a beam-scanning system.

Galvanometer mirrors

Galvanometer mirrors are often used for beam scanning in optical systems. Scan ranges of a fraction of a degree to many degrees are available, and the mirrors can be driven at rates up to thousands of cycles per second.¹⁸

In order to avoid vignetting of the beam in a scanning system, it is necessary to image the scanning mirror into the aperture of the objective (assuming the objective is not underfilled). Thus, a relay system is necessary for each scan mirror. It is possible in some cases to dispense with the relay system and accept degraded performance in exchange for a simpler optical system.

The galvanometer has one or more reflecting surfaces, with each reflecting face performing one or more scanning tasks within the system. For instance, in the slit-scanning system described in chapter 5, it is necessary to scan the source-slit image across the sample, the detection-slit image across the sample, and the detection-slit image across the face of the detector array. These three scanning tasks can be performed by one mirror face (see Fig. 5.22), two mirror faces,¹⁹ or three mirror faces.²⁰ The advantage of using a single scanner for multiple beams is that the beams are scanned in a fixed relationship to each other, eliminating the need to synchronize the timing of several scanners.

Nipkow disk

The Nipkow disk has an array of pinholes, which are imaged onto the sample. A beam of light covering many pinholes illuminates the "source" disk, which, when spun, results in a number of source points sweeping across the sample. A "detection" disk is

simultaneously spun and collects light through an array of detection pinholes conjugate to the source pinholes. The collected light is coupled to a detector array or through an ocular to the eye of a human observer. Nipkow disk systems typically use non-laser illumination such as an arc lamp and often operate in real-time. The minimum spacing between the pinholes in the disk is limited by the requirement that the response to illumination from a single source pinhole be detected through only a single detection pinhole, thereby avoiding crosstalk.¹⁵

Due to mechanical alignment difficulties, the Nipkow disk system is practical only if the same disk is used for both source and detection pinholes. This may be accomplished by using the same pinholes for illumination and detection, or by using different regions of the disk for the source and detection pinholes.²¹

Acousto-optic cells

Acousto-optic cells can be used to scan an optical beam by diffracting the beam as it passes through the cell. The diffraction angle is a function of wavelength, making these cells unsuitable for the collection arm of fluorescence systems, which have a wavelength shift between excitation and emission, as well as a range of emission wavelengths. Acousto-optic cells, however, are extremely fast (modulation frequencies of many MHz), allowing them to be used in real-time systems.

Spinning polygon

Spinning polygon mirrors are used in a similar fashion as galvanometer mirrors. The beam is scanned successively across the field by each facet of the polygon, with the sweep angle being determined by twice the angle between the facets (e.g., for a 72

facet polygon, the scan angle is $2 \times [360 \text{ degrees}/72] = 10 \text{ degrees}$). These scanners are most suitable for the fast-scan direction in confocal microscopes using two-dimensional scanners.²²

2.6. Slit scanning

As an alternative to the source and detection pinhole in confocal microscopy, it is possible to use a slit source and a slit detector. Images of a line source and detection slit are scanned across the sample. The light passing the detection slit is collected by a detector array, thereby collecting an entire row of pixels at one time. The detection slit can also be scanned across a two-dimensional detector array, such as a CCD, which integrates during the entire scan time to produce a two-dimensional image. This alternative method eliminates the need to reconstruct the image, and is used in the slit-scanning fiber-optic imaging-bundle confocal microscope of chapter 5.

The slit-scan confocal microscope represents a compromise between the optical-sectioning performance of the confocal microscope and the fully parallel nature of widefield microscopes, which image the entire field at one time. By using slits instead of pinholes, scanning needs to be performed in only one direction, significantly improving the rate at which images can be collected. The point-spread-function is now asymmetric, with a faster reduction in sensitivity perpendicular to the slit than parallel to the slit. In the fluorescent case, the image formed with this slit-scanning system (one-dimensional scanning) is equivalent to the image formed with a point-source and slit-detector (two-dimensional scanning).

2.7. Aberrations

The scanning techniques used in confocal microscopy can logically be divided into those that examine only a single position in the field (typically on-axis) versus those that cover a finite field. Imaging only a single, on-axis, field point eliminates the need to control off-axis aberrations in the optical design, which is an enormous simplification. This allows fewer components to be used in the objective and can therefore yield higher transmission.

Confocal microscopes generally use fast optical beams to maximize the optical-sectioning effect (for example, oil-immersion microscope objectives with numerical apertures up to 1.4). This makes the imaging performance of the system very sensitive to the thickness and refractive indices of the material between the final optics and the sample. For example, a variation of only 20 μm from the design thickness in microscope cover slips can halve the axial resolution in a 1.2 NA system.²³ This is an important factor in sub-surface and three-dimensional imaging, where the material above the sample effectively becomes part of the optical system and may significantly alter the imaging performance.

Index of refraction mismatches between the expected and actual intervening materials between the final lens and the focal plane can significantly reduce the imaging performance. Not only will the resolution be degraded, but the depth of an object may be misinterpreted. For example, it will be difficult to design a high-resolution system for examining human dermis. This is due to substantial variations between people and locations on the body of the properties, such as thickness and dryness, of the intervening epidermis.²⁴

2.8. Sources

Both laser and non-laser sources are used in confocal microscopy. Lasers offer intense sources of nearly monochromatic light, making them excellent sources for both reflection and fluorescence applications. They are also easily manipulated to allow efficient coupling of the beam through a pinhole and onto the sample. A variety of continuous wave and pulsed lasers are used in confocal microscopy.²⁵

Arc-lamp and other non-laser sources are used in Nipkow disk and some slit-scanning systems. While the illumination efficiency of such a system is typically lower than in a laser system, the incoherent nature of the light has advantages in cases such as real-time viewing through an ocular in a Nipkow disk system, where laser speckle may be distracting.²⁶

2.9. Pupil filters

In order to obtain an infinitesimally small focal point, it is necessary to focus the light from a full spherical shell surrounding the point, which is impossible in a real system. The finite extent of the pupil leads to diffraction effects and the minimum attainable spot size, as seen in Figure 1.3. It is possible with phase and/or amplitude filters in the illumination and collection pupils to alter the point-spread-function of the system, and, consequently, the overall performance of the system.^{27,28} Confocal systems are often hampered by low light levels due to the rejection of much of the light by the detection pinhole, making it undesirable to include amplitude filters in the collection arm.

2.10. Applications

Confocal microscopy has gained popularity in scientific, medical, and industrial environments, primarily due to the optical-sectioning effect. For example, confocal microscopes are used to examine the three-dimensional structure of semi-transparent objects such as fixed cells on microscope slides.

In semiconductor metrology, confocal microscopy is used to examine structures such as embedded wires connecting components on a chip or module. These structures are often located on multiple levels. A confocal microscope can be used to examine lower levels by using the optical-sectioning effect to minimize the impact of the upper levels on the image (the upper levels would normally obscure the lower levels).²⁹

Confocal microscopy is potentially useful in clinical medicine in a number of disciplines. It is possible to study biopsy samples without any treatment of the sample beyond mounting it on a stable base. This technique has been used by us to examine a fresh skin biopsy sample in reflection down to a depth of approximately 150 μm .

Confocal microscopy is also promising for in-vivo examination of tissue specimens. For example, an important clue in determining the progression of cancer is the invasion of the cancer cells below the basement membrane, which can potentially be done in-situ with a confocal microscope. Confocal microscopes have been used for in-vivo studies of human skin^{24,30} and eyes¹⁹ in non-invasive systems. Figure 2.8 shows a reflection image of the epidermis on the author's hand (intact), approximately 110 μm below the surface. This image was collected with a Zeiss LSM10 confocal microscope.

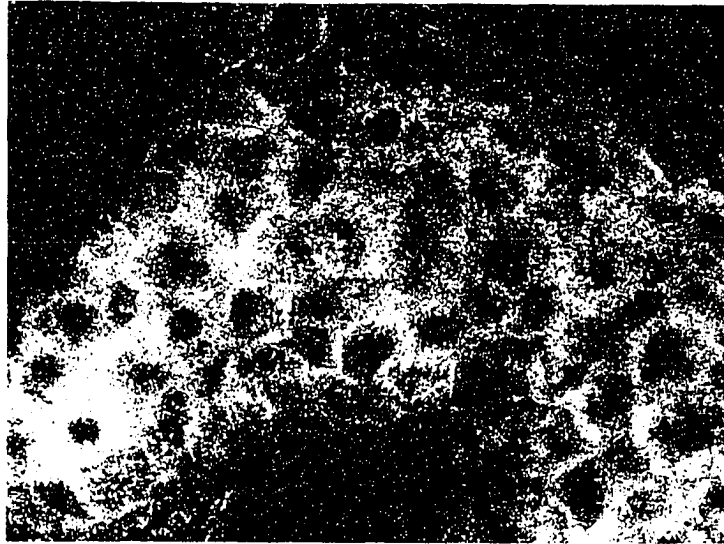


Figure 2.8. Confocal microscopy reflection (brightfield) image of the epidermis on the back of the author's hand (intact). Optical section depth approximately 110 μm below the surface of the skin. Image acquired with a Zeiss LSM10 microscope, Argon laser illumination (488 nm and 514 nm) and a 63x/1.4 NA oil immersion objective. Scan time = 2 seconds (sample mechanically stabilized with the end of the objective).

3. OPTICAL FIBERS

Optical fibers are dielectric waveguides best known for their applications in telecommunications, but also used for a variety of imaging and non-imaging applications. Fibers can be round, elliptical, polygonal, and so forth, with each type of fiber having somewhat different optical properties.

Most optical fibers are composed of a glass core surrounded by a cladding of lower refractive index material. Early fibers were unclad, relying on the index difference between the glass and surrounding air to contain the light. However, unclad fibers are susceptible to losses due to dirt or impurities on the surface of the fiber, and are seldom used in practice (with the exception of some specialty fibers that cannot be clad due to material considerations). The index of refraction in an optical fiber may vary within the core and/or clad to achieve specific operating characteristics, such as low dispersion in a telecommunications fiber or minimal crosstalk in a fiber-optic imaging bundle. Several core-clad refractive index profiles are shown in Figure 3.1.

The propagation of light in an optical fiber can be described in terms of rays (geometrical optics description) or modes (physical optics description).³¹ The mode description is more accurate, but is also more complex, and is unnecessary to explain many of the phenomena characterizing optical fibers.

3.1. Ray description

The simplest way to view optical fibers is in terms of light rays that, once coupled into the fiber core, propagate down the fiber as long as they reflect off the core-clad

interface at angles larger than the critical angle. Bound rays in a round optical fiber are either meridional or skew rays. Meridional rays pass through the fiber axis between each reflection, and therefore always travel in one plane. Skew rays rotate around the axis as they propagate down the fiber. Meridional and skew rays are shown in Figures 3.2a and 3.2b, respectively.

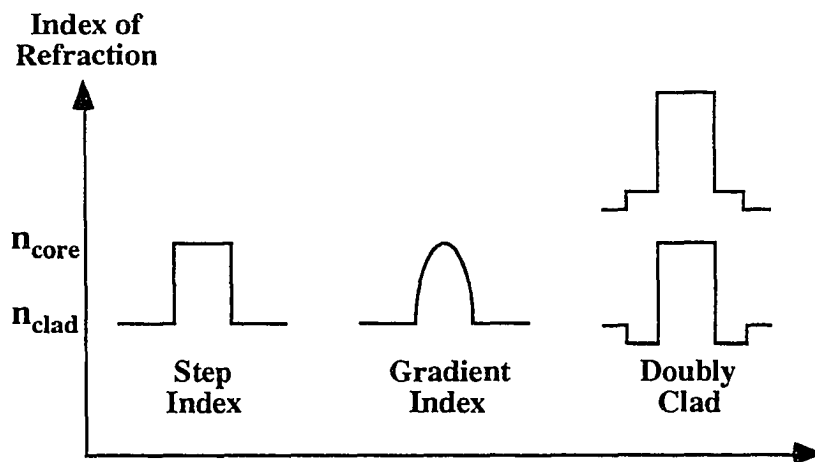


Figure 3.1. Several core-clad refractive index profiles of optical fibers.

Since bound rays in the core are totally internally reflected at the core-clad interface, they correspond to imaginary incidence angles in the clad. Rays that exist in the clad can never be refracted into a bound ray in the core. Therefore, light that is coupled into the clad of an optical fiber is either lost through the outside wall of the fiber or propagates as a cladding mode (occurs when the fiber has an outer coating with an even lower index of refraction than the clad). An exception to this is scattering that occurs at the core-clad interface or within the core, and results in a change in

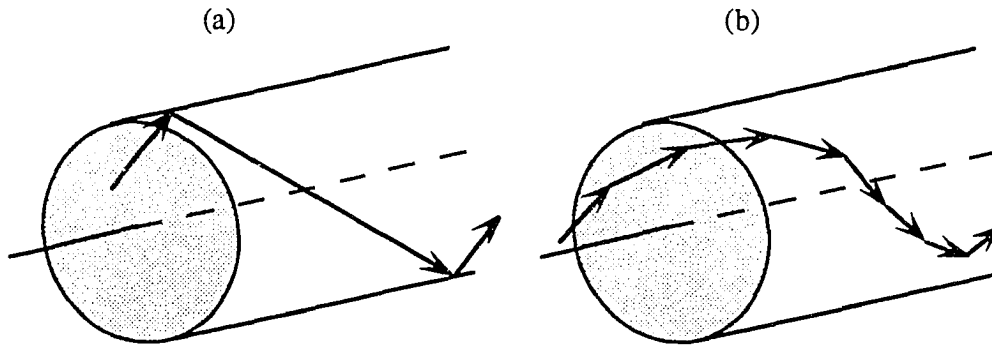


Figure 3.2. Meridional (a) and skew (b) rays in an optical fiber.

propagation direction such that the light is now totally internally reflected within the fiber core. Assuming scattering is low (which would be necessary in a low loss fiber), this effect can be neglected.

Several rays are shown in Figure 3.3. A bound ray is depicted by short dashes, having been coupled into the fiber core such that the reflections at the core-clad interface occur at angles greater than the critical angle. The solid line shows a ray that is coupled into the core at an angle too steep to be retained in the fiber. A "clad" ray is depicted with long dashes and can be seen to pass through the core without becoming bound.

A beam of light with finite numerical aperture can be described as the sum of many rays with different propagation directions. These rays will undergo many reflections off the core-clad interface in a typical fiber, with the result that the light exiting the fiber will be uniformly distributed across the face of the fiber. Thus, in the ray model, an optical fiber can be thought of as a device that integrates the light captured by it, emitting a spatially uniform beam over the same range of angles as the input beam.

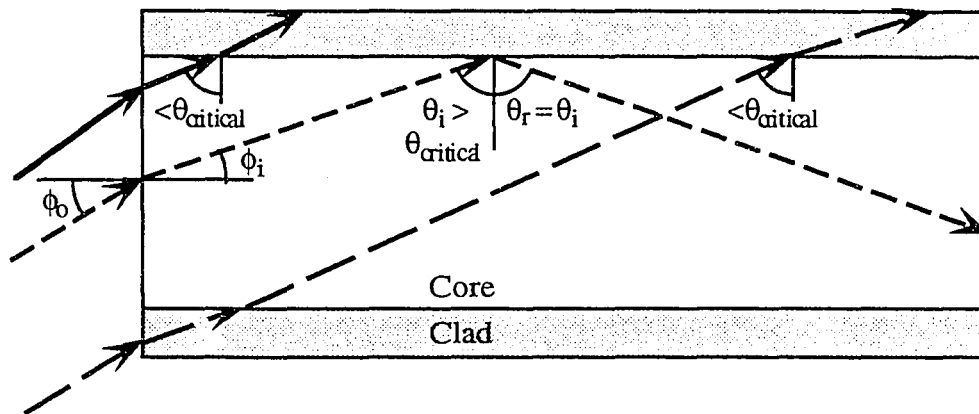


Figure 3.3. Bound and unbound rays in an optical fiber. A bound ray is depicted by short dashes. An unbound refracting ray that is not totally internally reflected (TIR) at the core-clad interface is depicted by a solid line. An unbound "clad" ray is depicted with long dashes. Each ray transmitted through an interface is accompanied by a reflected ray. These non-TIR reflected rays are not shown in this figure.

A diagram of this is shown in Figure 3.4a. If a fiber is not uniformly illuminated over its full numerical aperture, then the corresponding output beam will comprise only the range of angles that make up the input beam. The fiber will generally produce an axially symmetric output beam even for an asymmetric input beam, as shown in Figure 3.4b.

3.2. Mode description

The mode description of optical fibers recognizes that an optical fiber is really a dielectric waveguide and can support only the electromagnetic field distributions of specific modes. This complete orthogonal set of modes includes a discrete set of

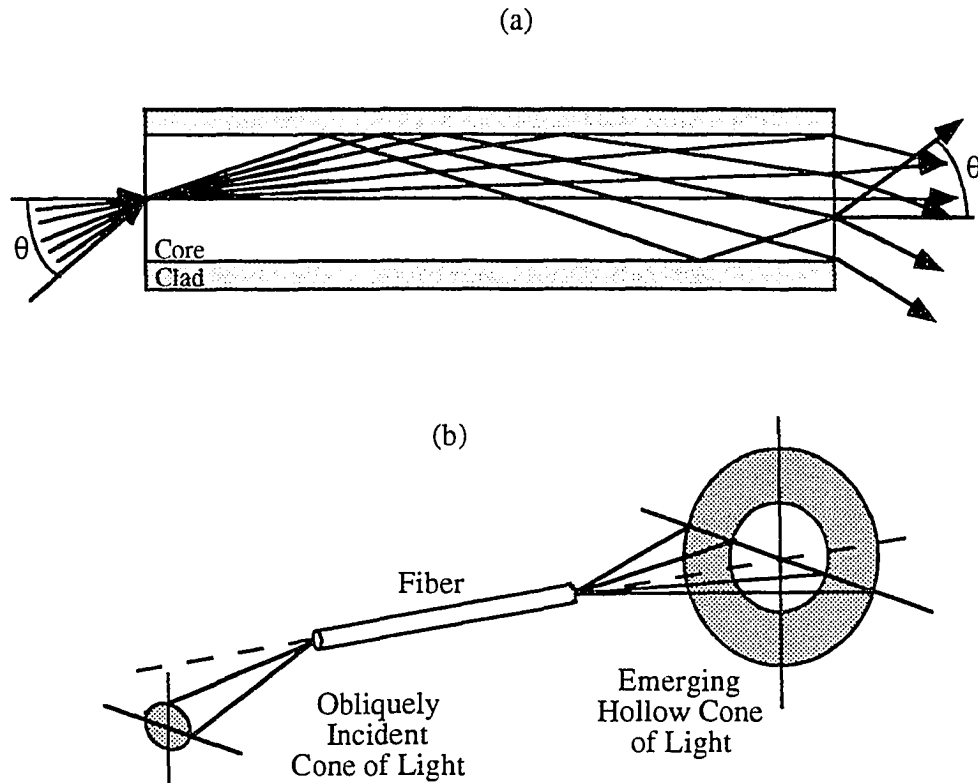


Figure 3.4. Integration of a beam by an optical fiber (assuming many modes). (a) Light that is coupled into the core at any point is evenly distributed across the core upon exiting the fiber. (b) Light passing through the fiber maintains the same angle magnitude with respect to the axis, but spreads azimuthally to become approximately symmetric about the axis (after Hopkins³²).

bound modes and a continuous set of unbound modes.³³ The modes are a function of the physical dimensions and material parameters of the fiber, as well as the wavelength and the vectorial nature of the light. Light incident on the end of an optical fiber excites a mode of the fiber according to the overlap between the modal field and the electromagnetic field of the illuminating beam.

The intensity pattern for a superposition of the bound modes of a single fiber in an 0.35 NA fiber-optic imaging bundle is shown in Figure 3.5. The lowest order mode predominant in Figure 3.5 is likely to be rotationally symmetric and approximately Gaussian, as it is in all weakly guiding circular fibers (this fiber is actually somewhat hexagonal, as seen in Figure 4.4a). The higher order modes vary both radially and azimuthally. The experimental conditions used to obtain this measurement are described in chapter 4 (see Figure 4.7).

Unbound modes can be divided into refracting and tunneling modes. Refracting modes correspond roughly to ray directions that are not totally internally reflected at the core-clad interface. Energy in the refracting modes attenuates very quickly.

Tunneling modes can be thought of as a form of frustrated total internal reflection arising due to the curvature of the core-clad interface.³⁴ The modes of an optical fiber are a function of both core and clad parameters, and some amount of the light propagates in the clad. A tunneling mode occurs when the initially monotonically decreasing electric field in the clad becomes oscillatory, resulting in some of the energy propagating radially outward.

The degree to which the ray description adequately describes the performance of an optical fiber increases with the number of modes. For a single-mode telecommunications fiber, the mode description will nearly always be necessary to describe the fiber, while for a large core fiber with hundreds or thousands of bound modes, the ray description will generally be sufficient. With only a few bound modes, the fiber of

Figure 3.5 is not adequately represented by the ray model, and the mode description must be employed to fully describe the optical characteristics of the bundle.

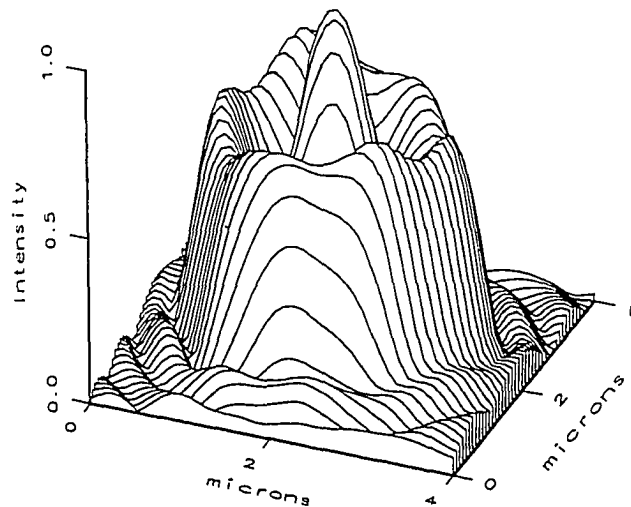


Figure 3.5. Intensity pattern corresponding to the bound modes of a slightly hexagonal optical fiber. Fiber NA = 0.35; core diameter $\sim 3.4 \mu\text{m}$; white light illumination overfilling the fiber.

The tangential components of the electric and magnetic fields are continuous across the core-clad interface of an optical fiber. Thus, the modes shown in Figure 3.5 actually extend into the fiber cladding. This also says that light incident on the clad can be coupled into bound modes, albeit inefficiently. This is an example of where the ray description is lacking.

3.3. Weakly guiding fibers

Many optical fibers can be described as "weakly guiding," which is defined by $\Delta \ll 1$, where

$$\Delta = [(n_{core} - n_{clad})/n_{clad}]^{.35} \quad (3.1)$$

For the Sumitomo IGN-05/10 imaging bundle, $n_{core} = 1.498$ (peak at center) and $n_{core} = 1.454$, yielding $\Delta = 0.03 \ll 1$. Measurement of these refractive index values is described in appendix A.

3.4. Numerical aperture

The numerical aperture of an optical fiber is a geometrical optics concept used to describe the range of angles over which illuminating light will be coupled into the bound modes of the fiber. It is determined by the indices of refraction of the core and clad, where

$$NA = \sqrt{n_{core}^2 - n_{clad}^2} \quad (3.2)$$

For the case of gradient-index core profiles, as shown in Figure 3.1, the numerical aperture is a function of position in the core, yielding a local numerical aperture

$$NA(r) = \sqrt{[n(r)]^2 - n_{clad}^2} \quad (3.3)$$

where the index profile is assumed to be axially symmetric.

The numerical aperture of a fiber is defined by the steepest meridional ray that will be totally internally reflected at the core-clad interface. Skew rays can be bound by a fiber at angles steeper than indicated by the numerical aperture. This leads to an effective NA for a perfect circular fiber that is somewhat greater than the nominal NA defined in equation (3.2).³⁶ In practice, the nominal NA provides a reasonable estimate for real, imperfect fibers, and is the value specified by manufacturers, albeit usually for the preform, rather than the actual fiber.³⁷

For single-mode fibers, such as those used in telecommunications, the mode field radius (beam waist radius) of the approximately Gaussian lowest order mode is a more useful parameter than numerical aperture.

3.5. Number of bound modes

The number of bound modes in a fiber is a function of the core diameter, wavelength, numerical aperture, and core index profile. For step-index fibers, the number of bound modes is approximately

$$N_{bm} = \left(\frac{V^2}{2} \right), \quad (3.4)$$

where

$$V = \left(\frac{\pi D}{\lambda} \right) NA \quad (3.5)$$

and D is the core diameter, λ is the wavelength, and NA is the numerical aperture.³¹ Equation (3.4) is valid for $V \gg 1$. It is interesting that this definition of the fiber "V"

parameter is equivalent to the definition of the normalized pinhole radius parameter, v_p , given in equation (2.5), where the pinhole radius and beam NA have been replaced by fiber core radius and fiber NA, respectively.

3.6. Dispersion

There is significant motivation for controlling the number of bound modes in a fiber. Each mode has a distinct group velocity, which is the rate at which energy in the mode propagates through the fiber. If a pulse of light is coupled into multiple bound modes, the resulting pulse exiting the fiber will be spread out in time according to the product of the fiber length and the range of group velocities of the excited modes. This phenomenon is called inter-modal dispersion, and is the reason most telecommunications fibers are designed to support only a single mode.

The light exiting from a fiber is the sum of the light contained in each bound mode (neglecting any remaining light in unbound modes). Since each mode has a different group velocity, the field distribution exiting a multi-mode fiber will vary with fiber length.

There are two other types of dispersion in optical fibers, which together are referred to as chromatic dispersion.³⁸ Material dispersion is due to the change in refractive index with wavelength. Waveguide dispersion is due to the change in the relative dimensions of the waveguide and the light wavelength. Chromatic dispersion results in pulse spreading, and, therefore, limits the bandwidth of single-mode fibers.

3.7. Materials

Optical fibers are manufactured from a variety of materials including silica and doped silica, conventional optical glasses (primarily borosilicates, also referred to as soft glass³⁹), plastics, and specialty materials for purposes such as infrared transmission or radiation resistance.

Silica is the most common material used in the manufacture of optical fibers. Dopants such as germanium or fluorine are used to raise or lower the refractive index in order to obtain a waveguide structure. Losses in silica fibers are very low, particularly in the near infrared, and can be minimized over broad wavelength regions by controlling the hydroxyl (OH) ion content. Silica multi-mode fibers are available with losses of 0.1 - 3 dB/m over the wavelength range of approximately 200 nm to 2500 nm, and are capable of carrying power levels in excess of 1 GW/cm².^{40,41} Silica imaging bundles transmit extremely well in the visible region, with losses of 0.1 - 0.2 dB/m,^{42,43} and are commonly used in medical and industrial endoscopes. While these losses would be unacceptable in telecommunications fibers, they are reasonable for short fiber lengths such as might be used in medical or industrial systems.

Single-mode telecommunications fibers operating at 1300 or 1550 nm are manufactured using silica. These two wavelengths are chosen due to minimum chromatic dispersion at 1300 nm and minimum attenuation at 1550 nm (on the order of 0.2 dB/km). The bandwidth of these fibers can be many GHz-km (given as the product of frequency bandwidth and distance because the pulse-spreading is proportional to both fiber length and signal bandwidth).

Conventional optical glasses were the most common materials used in early optical fibers, and are still common in imaging and non-imaging bundles.⁴⁴ These fibers generally exhibit high numerical apertures, on the order of 0.6 in flexible imaging bundles and 1.0 in rigid bundles.⁴⁵ Losses are fairly uniform throughout the visible spectrum, making glass fibers and bundles suitable for illumination and endoscopy applications.

Plastic is used in the manufacture of optical fibers that need to be either very flexible or inexpensive. Such applications include illumination and imaging bundles as well as rigid light conduits.^{46,47,48}

In order to transmit light in the infrared at wavelengths longer than approximately 2.5 μm , it is necessary to use special materials. For example, silver halide fibers can transmit wavelengths between 3 μm and approximately 15 μm .⁴⁹

3.8. Losses

There are several loss mechanisms in optical fibers, including Fresnel reflections from the end faces, coupling into unbound modes, finite cladding thickness, scattering, absorption, and bending.

Fresnel reflections

Fresnel reflection losses occur at the entrance and exit faces of optical fibers due to the change in refractive index between the fiber material and the surrounding medium.

For glass fibers immersed in air, these losses are approximately 4% at each face. Most fibers have relatively small index variations between core and clad, so reflections from

the two regions of the fiber will be approximately the same. These losses may be reduced by putting anti-reflection coatings on the faces of the fiber.

Unbound modes

As discussed above, only light coupled into the bound modes of a fiber is transmitted efficiently by the fiber. Light that is not coupled into the bound modes is typically attenuated over a short length of the fiber.

Energy coupled into tunneling modes is lost more gradually than energy coupled into refracting modes. For the fibers discussed in the following chapters (a few microns in diameter), little energy in these modes will remain beyond the first few millimeters. For example, the fiber in the Sumitomo bundle of Figure 3.5 has a constant cladding refractive index and a cubic core index profile (core radius $\approx 1.7 \mu\text{m}$). This results in approximately 90% of the energy in the tunneling modes being lost within the first millimeter.³¹

Finite cladding thickness

In order to have lossless transmission, the clad must have infinite thickness due to the infinite extent of the evanescent waves in the cladding. In practice, a clad thickness of some number of wavelengths will be adequate to minimize losses. The necessary clad thickness is a function of the wavelength, core diameter, numerical aperture, and mode. If the clad is too thin, energy can be lost through the interface between the cladding and surrounding jacket. This effect is employed in fiber couplers by bringing multiple cores together with a cladding thickness too thin to prevent coupling between

the modes of the fibers. This is also a source of reduced resolution in imaging bundles due to crosstalk between the fibers of the bundle.

In single-mode telecommunications fibers, the index of refraction difference between the core and clad of the fiber is small, requiring a thick clad, typically 125 μm in diameter, while the core may be only 5 μm in diameter. This is necessary due to the large extension of the evanescent waves into the cladding. It is also possible to limit losses and crosstalk without employing a thick cladding by increasing the core-clad refractive index difference while maintaining a very small core (a few wavelengths in diameter). This is the technique used in making high-resolution imaging bundles, where a thick cladding on each fiber would result in inefficient light transfer through the bundle.

Scattering

Scattering of light in an optical fiber occurs in the core, the clad, or at the core-clad interface. Scattering redistributes energy from bound modes into other bound modes and into unbound modes, resulting in losses. The effect of impurities at the core-clad interface can be minimized by making the core viscosity higher than the clad viscosity. This causes the impurities to be pushed into the clad during the manufacturing process.⁵⁰

Absorption

The absorption of light in fibers varies widely with material and wavelength. The losses acceptable for telecommunications fibers are generally much lower than for other types of fibers. The wavelengths chosen for optical communications are heavily

influenced by the absorption spectrum of silica. This is in distinction to general use fibers, which are designed to give good transmission for short distances over a fairly wide wavelength range. As discussed in chapter 4, absorption losses in short lengths (e.g., < 3 meters) of silica imaging bundles are substantially less than the input coupling losses, and are of minimal importance in the fiber-optic imaging-bundle confocal microscope

Bending

Losses in fibers occur due to bending because the angles at which the rays intersect the walls of the fiber change, resulting in some of the bound rays becoming unbound. High-resolution silica imaging bundles are of moderate flexibility, being constructed of many fibers fused together into what is a reasonably thick bundle (e.g. 0.5 mm diameter). Bending in this case is restricted by the mechanical limitations of the bundle. For example, the Sumitomo IGN-05/10 bundle has fiber core diameters on the order of $3.4\ \mu\text{m}$ (see chapter 4) and a specified minimum bending radius of 30 mm.⁵¹ This results in a bending-radius to core-radius ratio that is greater than 10^4 . In conjunction with the bundle numerical aperture of 0.35, this results in negligible bending losses.⁵²

Exceeding the allowed bending radius is likely to result in a catastrophic failure of the bundle (it breaks) before sizable bending losses occur. For this reason, bending losses are not considered a significant issue in the fiber-optic imaging-bundle confocal microscope.

4. FIBER-OPTIC IMAGING BUNDLES

This chapter discusses general properties of fiber-optic imaging bundles, particularly their suitability for inclusion in a fiber-optic imaging-bundle confocal microscope.

Fiber-optic imaging bundles are arrays of optical fibers assembled in a fixed spatial orientation, allowing transmission of an image. The image is focused onto one end of the bundle. Each fiber collects an amount of light approximately proportional to the irradiance in a small region of the image. The fibers transmit the light to the other end of the bundle, and the light exiting from the bundle represents a sampled image of the irradiance distribution at the entrance face of the bundle. The fidelity of this process is determined by the properties of the fibers and the bundle. Important fiber parameters are size, spacing, numerical aperture, losses, and the finite number of bound modes. Important bundle parameters are size and flexibility, the number of fibers, crosstalk between the fibers, and light coupled into the cladding.

Fiber-optic imaging bundles were first proposed in 1927,^{53,54} and successfully assembled and tested in the early 1950's.⁵⁵ Since that time, the techniques used to manufacture imaging bundles have improved considerably, resulting in both flexible and rigid bundles made of a variety of materials and used in numerous applications. Flexible imaging bundles are typically used in medical and industrial endoscopy applications, while rigid image bundles are used in image intensifiers, tapers, and faceplates. Materials used in imaging bundles include pure-silica and doped-silica glass, compound glasses, plastics, and a few specialty materials.

Silica imaging bundles offer the highest resolution and lowest loss of commercially available flexible bundles, making them the best choice for use in a confocal microscope. Experimental results for three silica bundles are given in this chapter, and one of them (Sumitomo Electric Corp. IGN-05/10) was used in the two fiber-optic imaging-bundle confocal microscopes described in chapter 5.

Fiber bundles are typically assembled with round cores in a hexagonal pattern, although the actual shapes and positions may be perturbed during manufacturing. A hexagonal pattern yields the most efficient packing of round fibers in an array. Alternative geometries are round or square cores in a square pattern and hexagonal cores in a hexagonal pattern. Moiré fringes can result when a high spatial-frequency pattern (e.g. a grating) is transmitted by a fiber bundle. The regularity of these fringes is reduced by bundle irregularities, and may actually make the perfect hexagonal bundle an undesirable idealization.^{56,57} Figure 4.1 shows an idealized hexagonal array of round fibers; Figure 4.4a shows a section of a Sumitomo IGN-05/10 bundle. The cores of the Sumitomo bundle have become somewhat hexagonal during the manufacturing process. The fiber size, shape, and spacing varies considerably in this bundle, although the arrangement is roughly hexagonal over short distances.

4.1. Imaging bundle characteristics

The point-spread-function (PSF) of an imaging bundle depends on the position of the image point with respect to the fibers. Light that falls directly on a fiber core will be most efficiently transmitted by the bundle, while light that falls on the cladding region between the cores will generally be distributed through the clad in some complex

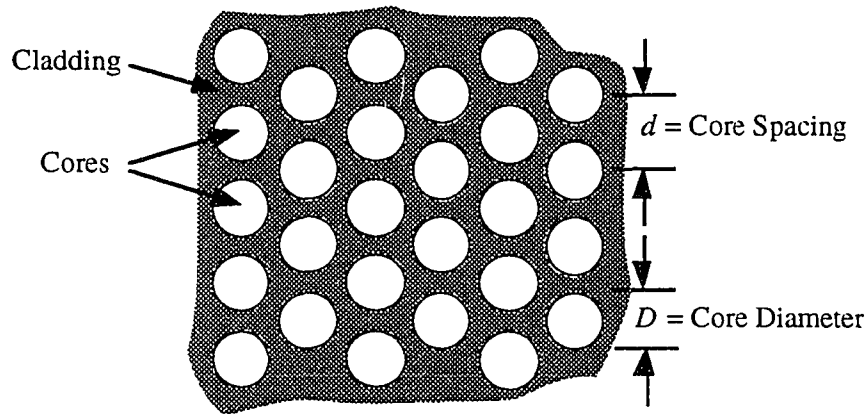


Figure 4.1. Idealized hexagonal arrangement of circular core fibers.

manner or lost through the sides of the bundle. Additionally, due to the finite number of bound modes in an optical fiber, light that is incident on a fiber core must be coupled into the bound modes of the fiber in order to be efficiently transmitted. Thus, the point-spread-function of fiber bundles is space-variant, and no single point-spread-function or modulation-transfer-function (MTF) can be assigned to a bundle. Most of the literature concentrates on either specifying an average point-spread-function or generating a space-invariant imaging system by rapid ("dynamic") lateral scanning of the bundle to blur out the effect of individual fibers.

Fiber size, shape, and spacing

The size of the fibers in an imaging bundle influences the imaging performance due to the integrating effect of the fibers. In a fiber with many bound modes, all the light falling within the numerical aperture of the fiber will be captured by the fiber, and will be approximately evenly distributed across the fiber at the other end. In this case, detail finer than a single fiber will be lost by the bundle.

In the case of only a few bound modes, coupling of light into the fiber will be determined by the coupling between the field distributions of the illuminating beam and the bound modes of the fiber. This can be calculated with overlap integrals, which yield a coupling coefficient for each bound mode.³¹ Neglecting mixing of modes during transmission and mode-dependent loss and crosstalk, the fields exiting the fiber will be determined by the set of coupling coefficients times the corresponding mode distributions times a phase shift for each mode. In general, the field distribution exiting the fiber will not be the same as the fields coupled into the fiber due to the different phase velocity (and therefore different phase shift with fiber length) of each mode.

The fibers in imaging bundles vary in size. In cases of interest for implementing confocal microscopy through a bundle, the fiber cores are spaced between approximately 1 μm and 10 μm center-to-center. The smallest core spacings are found in flexible single-mode silica bundles, which have been produced but are not commercially available.⁵⁸ Flexible multi-mode silica bundles typically have core spacings in the 3 - 8 μm range,^{51,59,60,61} while flexible compound glass bundles have larger core spacings in the 6 - 25 μm range.^{45,60,62,63,64,65,66} Plastic bundles have been produced with 9 μm core spacing.⁴⁸

Imaging bundles must have a finite amount of area devoted to cladding material in order to guide the light and minimize crosstalk. The ratio of the core area to the total picture area of the bundle is referred to as the "core packing fraction" or simply the "packing fraction."^{32,67}

During the manufacturing of imaging bundles, round fibers are typically fused together in a hexagonal array. When round fibers are combined in such a pattern, there are initially small voids between the fibers. In rigid image bundles, such as fiber-optic faceplates, these voids are often filled with Extra Mural Absorption (EMA) to reduce crosstalk by absorbing stray light. In flexible image bundles, however, EMA is typically not used, and the voids are filled by cladding material during the fusing of the fibers. When possible, a higher viscosity material is used for the cores than for the cladding.⁵⁰ This causes the cladding to deform while maintaining the round structure of the cores. This is preferable to lower viscosity core than cladding, in which case the cladding thickness will remain constant and the cores will tend to deform, becoming somewhat hexagonal. As seen in Figure 4.4, some amount of core deformation occurs in silica bundles.

Numerical aperture

To maximize the packing fraction (for minimum coupling loss), it is desirable in imaging bundles to have thin cladding layers surrounding the fiber cores. This is accomplished by using large core-clad refractive index differences, which produces a quick decay of the evanescent fields in the cladding for most modes. These large refractive index differences result in fairly high numerical apertures of 0.2 - 0.66 in flexible imaging bundles.

Modes

The modes of fibers in an imaging bundle are similar in nature to the modes of a single optical fiber, with the exception that the modes of adjacent fibers may be coupled.

The manufacturing process for silica bundles tends to yield fibers that are somewhat hexagonal, and therefore have slightly different bound modes than round fibers. All commercially available imaging bundles are multi-mode at visible wavelengths. The bound modes of a fiber in a high-resolution silica imaging bundle are discussed and shown below.

Crosstalk

Crosstalk between fibers comes about due to coupling between the modes of adjacent fibers. Crosstalk is a function of the excited modes of the fibers, the degree of coupling between the modes of adjacent fibers, and fiber length. These parameters must be controlled to minimize crosstalk in imaging bundles.

Power exchange between a pair of nearly-identical single-mode fibers is given by

$$P_1(z) = 1 - F^2 \sin^2\left(\frac{C}{F}z\right); \quad P_2(z) = F^2 \sin^2\left(\frac{C}{F}z\right), \quad (4.1)$$

where $P_1(z)$ and $P_2(z)$ are the power in the two fibers and z is the length of the coupling region.³¹ The parameter C describes the interaction between the modes of the two fibers (C varies inversely with fiber separation) and influences the beat length over which the light is exchanged from one fiber to the other and back again. The parameter F describes the physical similarity between the fibers, and impacts both the beat length and the maximum amount of power exchanged between the fibers.

Crosstalk between multi-mode fibers has a significantly different appearance than that of single-mode fibers. The beat length of the modes of adjacent fibers, and therefore the rate at which energy is exchanged back and forth between the fibers, is a function of mode. For multiple excited bound modes with a variety of beat lengths, the energy will eventually reach an equilibrium (assuming many modes).⁶⁸ Small differences in the fiber core diameters result in a rapid decrease in crosstalk rate and magnitude. Alternative derivations of crosstalk have been made by Hopkins and Kapany⁶⁹ and by Kapany^{70,71} based on the area of adjacent fiber cores that are in close contact with each other, and by Hosono⁷² using the mode coupling between adjacent fibers.

During the manufacturing process, dissimilarities between adjacent fibers in imaging-bundles arise, significantly reducing the crosstalk. Sumitomo Electric Corp. uses a "disordered pack" scheme to control crosstalk by intentionally varying the core diameters, both between fibers, and of each fiber along its length.⁷³ Experimental measurements of crosstalk have been published by Sumitomo Electric Corp.,⁷⁴ Conde, et al,⁵⁷ and Komiyama and Hashimoto.⁷⁵

Cladding modes

Light coupled into the cladding of fiber bundles can propagate in cladding modes. In the case of multi-core fiber bundles (such as the Sumitomo IGN-05/10 and IGN-10/13), the continuous cladding throughout the bundle results in the extension of these modes over the entire bundle. The light in cladding modes in a multi-core fiber bundle will generally exit from the bundle at a position related in some complex fashion to the input position. This light will contribute background noise, reducing the contrast of images transmitted by the bundle.

Cladding modes are likely to be less of a problem in leached bundles, where the fibers are adjacent only at the ends of the bundle, resulting in cladding modes that are limited in extent to a single fiber. It is not clear how significant cladding modes are in the case of wound bundles (described below), which may have a continuous cladding region containing many fibers and extending over the entire length of the bundle.

Bundle sizes

Imaging bundles are available in a large range of sizes, from a few hundred fibers in the smallest silica bundles to hundreds of thousands of fibers in large rigid bundles. The number of fibers can be thought of as the space-bandwidth product of the bundle, providing the upper limit on the number of pixels in an image. The Sumitomo IGN-05/10 imaging bundle used in the systems of the following chapter have 10,000 fibers. Therefore, these systems can collect an image with up to 10,000 pixels.

Losses

Packing fraction

As described above, the packing fraction is the ratio of the area of the cores to the total picture area of the bundle. This is a geometrical optics estimate of the maximum throughput of a fiber bundle (neglecting Fresnel reflections at the entrance and exit faces, and absorption and scattering losses in the bundle). For round cores in a hexagonal pattern, as shown in Figure 4.2, the packing fraction is:

$$\text{Packing Fraction (PF)} = \frac{\pi \left(\frac{D}{2} \right)^2}{\left(\frac{\sqrt{3}d^2}{2} \right)}, \quad (4.2)$$

where D and d are the average core diameter and core center-to-center spacing, respectively.

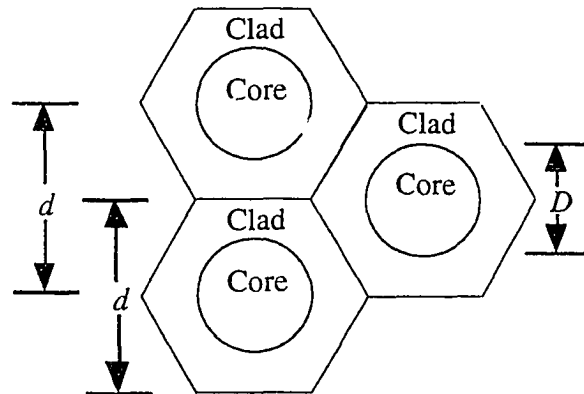


Figure 4.2. Geometry of cores and cladding in a hexagonally-packed imaging bundle. D = core diameter and d = center-to-center core spacing.

The allowable packing fraction is proportional to the size of the cores and the numerical aperture. This is because the clad thickness necessary to minimize crosstalk decreases with both increasing core diameter and higher refractive index difference between core and clad. The cores can be reduced in size to yield a higher resolution bundle, but the cladding cannot be reduced proportionally without increasing the crosstalk.

Coupling losses

In an identical fashion to single fibers, light incident on the end of a fiber bundle must be coupled into the bound modes of the fiber in order to effectively propagate to the distal end of the bundle. Illumination light that falls onto cladding regions of a multi-

mode bundle will generally be lost. This was discussed in the previous chapter for single fibers and applies equally to bundles.

Transmission losses

Transmission losses in multi-mode fiber bundles are largely a function of the material with which the cores are constructed. The properties of materials used in fiber bundles are discussed below.

Distortion

Maximum fiber misalignment is typically specified for imaging bundles in terms of the deviation of a straight line when seen through the bundle. This is usually defined by bundle manufacturers as distortion or coherency, and has no relationship to the classical definitions of optical distortion or coherence.

The two manufacturers of the multi-core silica bundles used in this work do not specify the distortion of their bundles. Current leached compound glass imaging bundles have minimal distortion.⁷⁶ Wound fiber bundles tend to have misalignment of multi-fiber groups rather than single fibers,⁷⁷ resulting in a line input producing a substantially distorted line output.

4.2. Imaging properties

Fiber-optic imaging bundles are used in two distinct ways: static scanning or dynamic scanning. In "static scanning", a term proposed by Hopkins and Kapany, the fiber bundle ends are held in fixed positions, resulting in the space-variant imaging described above.⁵⁵ "Dynamic scanning" of a fiber bundle was proposed somewhat

later by Kapany,⁷⁸ and is accomplished by laterally scanning the ends of the fiber bundle in unison. This blurs out the structure of the fibers in an image conveyed by the bundle, and, thereby, yields a space-invariant (isoplanatic) imaging device. Kapany and his colleagues found that scanning the bundle randomly over a distance of approximately 4 - 5 fiber diameters at a rate of 80 cycles per exposure completely eliminated the space-variance of the imaging, and approximately doubled the cutoff frequency of the bundle modulation-transfer-function. Unfortunately, it is often not noted in the literature whether static-scanning or dynamic-scanning has been used for a modulation-transfer-function measurement, making it difficult to compare various manufacturers' bundles with each other or with theoretical predictions.

Since the goal of this work is to inspect difficult to reach locations via an imaging bundle, it can be assumed that the sample locations will not generally lend themselves to the mechanism necessary for precise physical scanning of the fiber bundle. Therefore, the static-scanning case will be more relevant for this application. Furthermore, as discussed in the following chapter, the main advantage of the fiber-optic imaging-bundle confocal microscope over the (single fiber) fiber-optic confocal microscope is the elimination of the lateral scanning mechanism at the distal end of the fiber.

Theoretical models of imaging performance in static and dynamic scanning have been developed by a number of authors. These models assume that light coupled into a fiber will be evenly distributed across the core upon exiting the fiber - a geometrical optics approximation whose validity increases with the number of bound modes in the fibers. The number of bound modes increases with the core diameter and the core-

clad refractive index difference, and decreases with wavelength. High-resolution silica imaging bundles are used in the fiber-optic imaging-bundle confocal microscope described in chapter 5. As seen in Figure 4.7, the fibers of such a bundle have only a few bound modes, making the assumption of many modes questionable for these bundles.

Static scanning

In their early work, Hopkins and Kapany estimated the static-scanning resolution of a bundle to be limited by the size of the fibers in the bundle. They obtained a resolution of 4 lines/mm for a bundle composed of $D = 60 \mu\text{m}$ diameter fibers.^{55,69} This theoretical result followed from the fact that a straight line imaged through the bundle would appear "broken," with the maximum extent of the error in the image being two fiber diameters (approximately $1/8 \text{ mm}$ since they were using unclad fibers). Therefore, the smallest resolvable detail is on the order of two fiber diameters, and the maximum spatial frequency that can be transmitted is $f = 1/(4D) = 4 \text{ lines/mm}$. They found experimentally that their bundle could resolve this spatial frequency, and furthermore, that it could resolve higher spatial frequencies when the test object (grating) was rotated to coincide with one of the three orientations, $\phi = \pi/6, \pi/2$, and $5\pi/6$, shown in Figure 4.3.

Hopkins later estimated the resolution of a fiber bundle based on the sampling frequency.³² He predicted a maximum spatial frequency of $f = 1/(2d)$ for a perfectly aligned close-packed bundle (neglecting cladding thickness, as shown in Figure 4.3, to obtain core spacing, d , equals core diameter, D). Considering the finite cladding

thickness and fiber misalignments of a real bundle, he rewrites this in terms of core diameter as $f = 1/(2.5D)$.

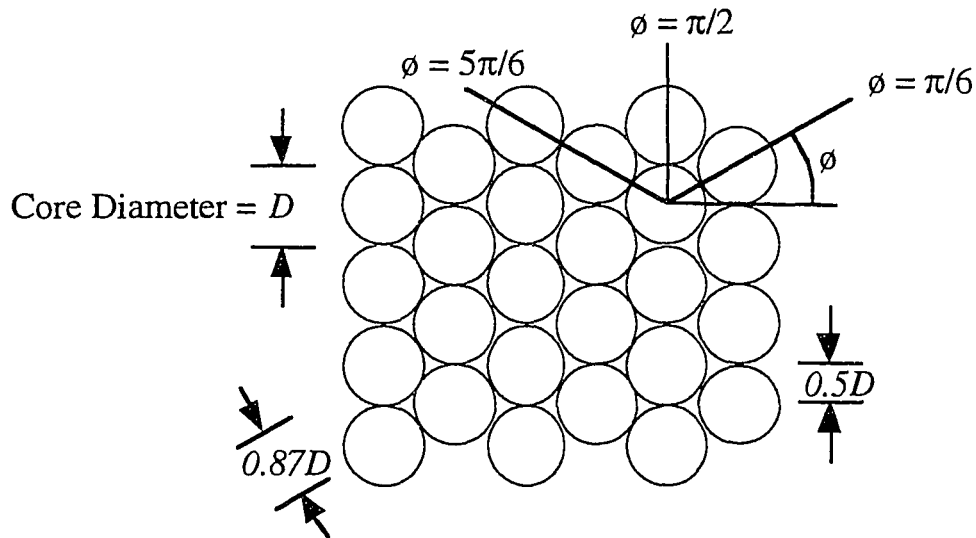


Figure 4.3. Hexagonal close-packed fiber model used to estimate resolution (after Kapany⁷¹). Orientations $\phi = \pi/6$, $\pi/2$, and $5\pi/6$ yield the fundamental sampling frequency of the bundle, while orientations $\phi = 0$, $\pi/3$, and $2\pi/3$ yield a higher sampling frequency.

Kapany also used the sampling frequency in later work to estimate the static-scanning cutoff frequency to be $f = 1/(2D)$ in one of the two directions of closest packing in a square fiber array.⁷⁸ He noted that a hexagonally close-packed bundle yields a smaller sampling interval of $0.87D$ (see Figure 4.3) and, therefore, a higher cutoff frequency of $f = 1/(1.73D)$. He also pointed out intermediate orientations of the bundle at which even higher spatial frequencies might be transmitted, albeit with reduced contrast. These orientations correspond to $\phi = 0$, $\pi/3$, and $2\pi/3$ in Figure 4.3 and have a sampling interval of $0.5D$.⁷¹

Drougard showed that for a perfect hexagonally close-packed bundle, the optical-transfer-function in the static-scanning case will vary between a maximum of $[2J_1(\pi fD)/(\pi fD)]$ and a minimum of $[2J_1(\pi fD)/(\pi fD)]\cos^2(\pi\sqrt{3}fD/2)$, depending on the orientation and phase shift of the object with respect to the bundle.⁷⁷ This corresponds to spatial frequencies of $f = 1.22/D$ and $f = 1/(1.73D)$ at the first zeros of the transfer function for the maximum and minimum cases, respectively. She also showed that for randomly distributed fibers in the bundle, a space-invariant static-scanning transfer function exists. As seen in Figure 4.4, and in a recent paper by Conde, et. al.,⁵⁷ there is an ordering of the fibers in commercial imaging bundles, and a model assuming random fiber positions will not be valid.

Drougard pointed out substantial difficulties in measuring imaging bundle modulation-transfer-functions. She examined two cases: 1) a sine wave image scanned across the entrance face of a fixed bundle with a fixed detection slit at the other end of the bundle, and 2) a fixed sine wave imaged onto the bundle, with a detection slit scanned across the other end of the bundle. The performance was significantly better in the first case, although the reason for this is unclear. For a shift-invariant imaging system, these two cases would yield identical results.

In commenting on the work of Kapany and Drougard, Siegmund noted the significant uncertainties inherent in calculating and measuring the modulation-transfer-function of the static-scanning fiber bundle. He suggests that a good rule of thumb for the resolution limit of a fiber bundle is between $f = 1/(3d)$ and $f = 1/(2d)$.^{37,67,76}

Vanwormhoudt and DeKinder discuss the resolution of static-scanning fiber bundles in terms of the space-variance and conclude that the usual concepts of transfer functions are not valid except at low spatial frequencies.⁷⁹ Thus, for example, the various line-spread-functions possible with a fiber bundle cannot simply be Fourier transformed to obtain the modulation-transfer-function of the bundle.

Marhic, et. al. proposed a statistical approach to explain the deviations of measured static-scanning modulation-transfer-functions from theoretical predictions.⁸⁰ They showed that the effect of misaligned fibers is to generate a space-invariant line-spread-function whose corresponding modulation-transfer-function is given by the product of the average modulation-transfer-function for a perfectly aligned bundle with a misalignment term having a normal statistical distribution:

$$H(f) = [2J_1(\pi fD)/(\pi fD)]^2 \exp(-2\pi^2 f^2 \sigma^2). \quad (4.3)$$

However, the amount of misalignment required to match the theoretical and experimental data was $\sigma = 0.51D$. Each core must have a substantial amount of area through which it can wander in order to allow this amount of misalignment.

Assuming each (round) core in a hexagonal arrangement can move a maximum of 2σ in any direction requires hexagonal cells of dimension $d = 3D$ (see Figure 4.2). This results in a core packing fraction of $[\pi(D/2)^2]/[\sqrt{3}(3D)^2/2] = 10\%$, far below that found in commercial imaging bundles. Thus, while this statistical model may be able to account for the discrepancy between theoretical and experimental modulation-transfer-functions, it does not do so in a manner consistent with actual bundles.

Csorba described the point-spread-function of a fiber bundle in terms of equal "disks of confusion" at the input and output end of the bundle, resulting in a cylindrical intensity distribution of diameter equal to two fiber diameters, and a modulation-transfer-function of $[2|J_1(2\pi fD)/(2\pi fD)|]$.⁸¹ While the average extent of the intensity distribution will be two fiber diameters, there is no apparent reason to expect the shape of the distribution to be cylindrical. In fact, the average point-spread-function in the static-scanning case is equivalent to the actual point-spread-function in the dynamic-scanning case, shown by Drougard to be the autocorrelation of a cylinder function.

Eberhardt pointed out substantial discrepancies between the experimental results of Drougard⁷⁷ and Allen,⁸² and suggested two alternative modulation-transfer-function approximations which are better suited to analytical calculations.⁸³

Most recently, Player has analyzed the "long slit" line-spread-function (LSF) of a fiber bundle.⁸⁴ Following Drougard and Eberhardt, he describes the input from a line illumination into a fiber in terms of a chord function that depends on the relative position of the line with respect to the fiber center. For a sufficiently long line of illumination such that many fibers are illuminated, there will be an average line-spread-function that is a function of the fiber core diameters only. He concludes that for object spatial frequencies that are low with respect to the sampling frequency, the average line-spread-function can be used to estimate the bundle modulation-transfer-function (valid only at these low frequencies). However, at higher spatial frequencies, the sampling nature of the bundle must be taken into account and the modulation-transfer-function cannot be written explicitly.

Dynamic scanning

The dynamic-scanning optical-transfer-function was initially derived and measured by Kapany.⁷⁸ He found that the object spectrum was multiplied by the frequency response of a disk of fiber diameter, D , resulting in an optical-transfer-function of $[2J_1(\pi f D)/(\pi f D)]$. This results in a cutoff frequency of $f = 1.22/D$, more than twice as high as the static-scanning cutoff frequency of either hexagonal or square fiber arrays. He confirmed this prediction experimentally below the cutoff frequency, but was not able to show the phase reversal above $f = 1.22/D$ predicted by this transfer function.

Kapany states in a later paper that the "dynamic point-spread function is a bell-shaped function with 2-fiber diameter width."⁷⁰ This is twice the width of the point-spread-function derived by him previously. Roetling and Ganley pointed out this contradiction, and suggested that with both ends of the fibers scanning with respect to the point source and the image recording device (photographic plate), the resulting image will be two fiber diameters wide.⁸⁵ They noted that for a non-tapering bundle with no crosstalk, the transfer function derived by Kapany in a third paper⁷¹ simplifies to $[2J_1(\pi f D)/(\pi f D)]^2$. This is consistent with the two fiber diameter width demonstrated by Kapany, and is somewhat bell shaped. Drougard later derived the same dynamic-scanning modulation-transfer-function.⁷⁷

4.3. Imaging bundle types

Flexible imaging bundles

Flexible imaging bundles are usually constructed as wound, leached, or multi-core fiber bundles. They are typically made of silica, compound glass, or plastic.

Bundle construction

Wound bundles

Early fiber bundles were made by continuously winding a single fiber onto a spool to produce an aligned array of fibers of the desired cross-section.⁷⁶ The fibers were then clamped together according to the desired bundle length, removed from the spool, and cut and polished. The length of wound bundles is limited by the size of the spool.

Current wound fiber bundles are typically constructed by assembling multi-fiber elements of between 5x5 and 10x10 individual fibers, which are then fused together to make a much larger bundle. A disadvantage to this technique is that entire multi-fiber elements may break or be misaligned during the manufacturing process, leading to potentially significant distortion or dark spots. Additionally, the underlying structure of the multi-fiber elements may be visible in the bundle, diminishing the image quality. Recently, the idea of using fractal multi-fiber shapes has been employed in making rigid fiber faceplates without the visible underlying structure of the multi-fibers.⁸⁶ This may find use with flexible bundles in the future as well.

Leached bundles

Leached bundles are composed of fibers that are aligned at the ends but allowed to float freely in the middle of the bundle, resulting in a highly flexible bundle. These bundles are manufactured by drawing a rigid bundle of fibers from a pre-assembled preform composed of fibers with an acid soluble cement between the fibers. The ends of the bundle are then placed in a fixture, and the middle of the bundle soaked in acid

to leach the cement from the center of the bundle. Through this technique, it is possible to obtain a bundle with negligible distortion and somewhat arbitrary length.⁷⁶

Multi-core fiber bundles

Multi-core fiber bundles are similar in manufacture to leached bundles, with the exception that the leaching stage is omitted, resulting in a semi-flexible bundle. This type of bundle is typically made with silica by Japanese manufacturers (Sumitomo, Fujikura, Olympus, and Mitsubishi). Reflection images of three silica multi-core fiber bundles are shown in Figures 4.4. The three bundles shown are the Sumitomo Electric Corp. IGN-05/10 (Fig. 4.4a), the Fujikura Ltd. FIGH-03-300C (Fig. 4.4b), and the Sumitomo Electric Corp. IGN-10/13 (Fig. 4.4c). The white bar in each image is 5 μm long. Based on these images, it appears that the two Sumitomo bundles have nothing separating the cladding regions of the individual fibers, and therefore are composed of many cores in what is essentially a single continuous cladding. The Fujikura bundle appears to have a separation between the cladding of individual fibers, but it is not known whether this is a material which has been added, or is an artifact of the manufacturing process. Thus, it is unclear whether the Fujikura fibers share a common clad.

Due to errors in the manufacturing process, multi-core fiber bundles typically have some degree of misalignment of the fiber elements.⁵⁷ This misalignment can vary from negligible to severe, and affects the imaging performance of the bundle (although not necessarily adversely, as discussed above regarding Moiré fringes and as pointed out by Drougard in terms of the space-variance of static-scanning imaging).

(a)

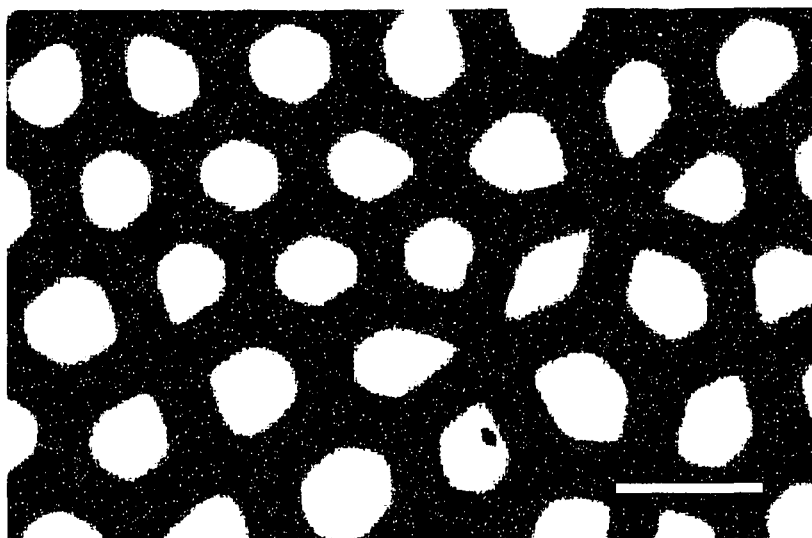
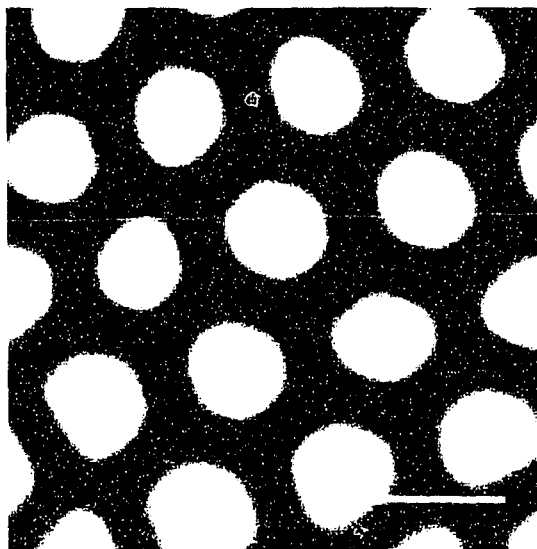


Figure 4.4. Reflection images of small sections of three silica multi-core fiber-optic imaging bundles. a) Sumitomo Electric Corp. IGN-05/10, b) Fujikura Ltd. FIGH-03-300C, and c) Sumitomo Electric Corp. IGN-10/13. The white bar in each image is 5 μm long. (Continued on the following page).

(b)



(c)

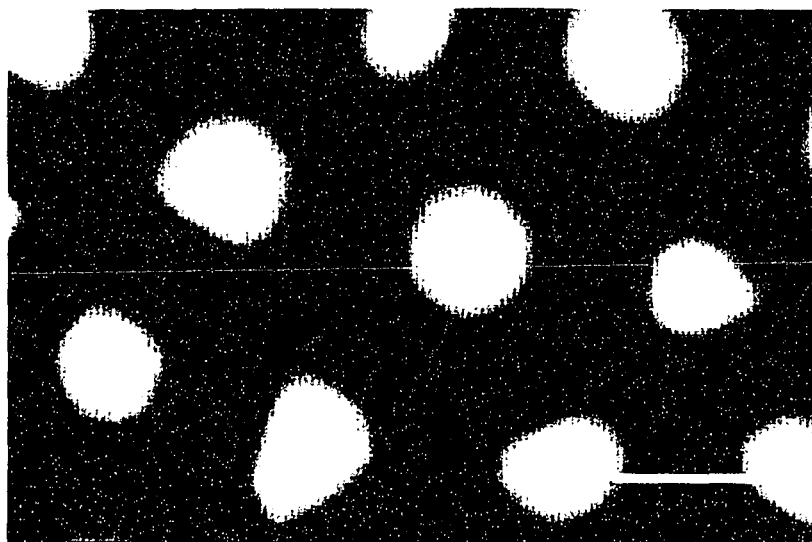


Figure 4.4. (Continued)

Materials

Silica image bundles

Silica bundles provide the highest resolution and lowest loss of the flexible image bundles. They are available in arbitrary lengths and a variety of thicknesses. Pixel (fiber) counts in silica bundles vary from several hundred up to tens or even hundreds of thousands. Attenuation in multi-mode silica bundles is less than 0.2 dB/m in the visible spectrum.^{42,43} The stiffness of silica bundles increases rapidly with bundle diameter. Silica bundles are available with center-to-center core spacings of 3 - 8 μm .^{51,59,60,61}

Both the core and cladding are typically pure or doped silica. The core index can be boosted with a dopant such as germanium, while the cladding index can be reduced with a dopant such as fluorine, yielding numerical apertures in the range of 0.2 to 0.45.^{42,43,87,88}

Silica bundles composed of single-mode fibers (at visible wavelengths) have been produced, but are not commercially available.⁵⁸ Fiber cores in these bundles are 1.0 to 1.4 μm in diameter and are spaced 1.7 to 2.9 μm center-to-center. Due to their small fibers, single-mode silica bundles are likely to allow bundles with tens of thousands of elements while remaining reasonably flexible. A substantial disadvantage to these bundles, however, is the inefficiency of coupling into their single bound mode, which results in substantially higher losses than in multi-mode bundles.

An advantage of silica bundles is the possibility of using equipment designed for telecommunications fibers. Recently, a 125 μm diameter silica rod lens and 125 μm

diameter (700 fiber) silica imaging bundle were fused together using an arc fusion splicer, rather than the more conventional technique of optical cement.⁸⁹

Compound glass bundles

Compound glass (also referred to as soft glass) bundles are manufactured from conventional crown and flint glasses. These bundles are manufactured using leached and wound techniques with core spacings of 8 to 25 μm (center-to-center).^{45,60,62 - 66} Compound glass bundles suffer from losses on the order of 3 dB/m in the visible spectrum, which are significantly higher than silica bundles.

Plastic image bundles

High resolution plastic image bundles are relatively new, and are both highly flexible and potentially cheaper than glass.^{46,48,90} Absorption losses are on the order of 0.5 - 2 dB/m in the visible spectrum, with the highest losses below 500 nm. Bundles with 7 μm cores spaced 9 μm center-to-center have been built.

Specialty materials for infrared and ultraviolet transmission

Imaging bundles have been built with special materials for thermal imaging in the infrared.^{91,92} Silica bundles are likely candidates for use in the ultraviolet, although none appear to have been designed specifically for this purpose. Silica imaging bundles with germanium doped cores are suitable over a limited wavelength range due to their tendency to color with exposure to ultraviolet light (primarily at 193 nm and 248 nm⁹³). However, radiation resistant bundles with pure silica cores have been built and may be usable at these wavelengths.⁴²

Rigid image bundles

Rigid image bundles are typically composed of many short fibers, and are used in applications such as microchannel plates, fiber-optic faceplates, and image reducers. Large core-clad refractive index differences are used to obtain numerical apertures on the order of 1.0.⁶⁷ Extra Mural Absorption (EMA) is often added between the fibers to reduce crosstalk in the bundle, whereas it is rarely used in flexible image bundles. Due to the large size of many rigid fiber bundles, a multi-fiber arrangement is often used, such as described above for wound bundles.

Rigid image bundles are of little use in confocal microscopy due to their inflexibility. It is possible to heat and bend the bundles into a fixed shape (e.g. with a 90 degree bend), which may be useful for applications with specimens in confined locations. Such applications are likely to be few, however, as a free-space optical path may also be used to reach the sample space.

4.4. Evaluation of three flexible silica multi-core imaging bundles

This section describes the experimental evaluation of three silica multi-core fiber bundles. The bundles tested are the Sumitomo Electric Corp. IGN-05/10, the Fujikura Ltd. FIGH-03-300C, and the Sumitomo Electric Corp. IGN-10/13. Included in this section are specified and measured parameters of core size, core center-to-center spacing, packing fraction, core and clad refractive indices, numerical aperture, bound modes, and crosstalk.

Sumitomo makes two series of imaging bundles. The smaller, high-resolution bundles have between 2,000 and 10,000 elements (fiber cores) with $\sim 4\text{ }\mu\text{m}$ core center-to-center spacing, while the larger bundles have 13,000 to 50,000 elements with 8 - 9 μm core center-to-center spacing.⁵¹

The IGN-05/10 is the largest of the Sumitomo high-resolution bundles, with 10,000 elements in a $\sim 0.45\text{ mm}$ picture diameter.⁷³ The cores are silica doped with GeO_2 to raise the refractive index, while the cladding is silica doped with Fluorine to lower the index. The numerical aperture is 0.35. An image of a section of the Sumitomo IGN-05/10 is shown in Figure 4.4a.

The IGN10/13 is one of the larger Sumitomo bundles with 13,000 elements in a $\sim 0.9\text{ mm}$ picture diameter. The cores are doped with GeO_2 and the cladding is pure silica, yielding a numerical aperture of 0.3. An image of a section of the Sumitomo IGN-10/13 is shown in Figure 4.4c.

Fujikura makes three series of image bundles: S, N, and C.⁵⁹ The S series has the highest resolution with 3.0 - 3.7 μm core center-to-center spacing, as compared to 3.8 - 5.2 μm and 3.9 - 6.0 μm for the N and C series, respectively. All three bundle types are available with 1,600 to 6,000 elements, and the N type is also available with 10,000 elements. It is not known if the material parameters differ between the bundle types.

The Fujikura FIGH-03-300C has 3,000 elements in a 270 μm picture diameter. The numerical aperture is 0.4 nominal.⁹⁴ An image of a section of the Fujikura FIGH-03-300C is shown in Figure 4.4b.

The Sumitomo IGN-05/10 has been the primary imaging bundle used in this project, due largely to availability (rather than technical superiority). Therefore, more data is available on this bundle than any other. Two 10-foot lengths of the bundle were purchased. No effort was made to track which test results (or images in the following chapter) corresponded to which of these two bundles. A single 3-foot piece of each of the other two bundle types was tested.

Table 4.1 summarizes the specified parameters of the three bundles used in this work.

Bundle	Fibers	Bundle Diameter	Picture Diameter	Core Spacing (center-to-center)	Cores	Cladding	NA
Sumitomo Electric Corp. IGN-05/10	10,000	0.5 mm	~ 0.45 mm	~ 4 μm	GeO ₂ doped Silica	F doped Silica	0.35
Fujikura Ltd. FIGH-03-300C	3,000	0.3 mm	270 ± 15 μm	not specified	(doped?) Silica	(doped?) Silica	0.4
Sumitomo Electric Corp. IGN-10/13	13,000	1.0 mm	~ 0.9 mm	8 - 9 μm	GeO ₂ doped Silica	Pure Silica	0.3

Table 4.1. Specified parameters of three silica imaging bundles discussed in this section.

Refractive indices and numerical aperture

A technique for measuring the refractive indices of optical fibers and imaging bundles is described in the appendix and was used to examine these bundles. Figure 4.5 shows the refractive indices of a few fibers in the Sumitomo IGN-05/10 (Figure 4.5a), Fujikura FIGH-03-300C (Figure 4.5b), and Sumitomo IGN-10/13 (Figure 4.5c) imaging bundles. All three of these bundles have gradient-index cores (see Figure 3.1).

The clad and peak core refractive indices were estimated for each bundle, resulting in the values shown in Table 4.2 (identical to Table A.1 in the Appendix).

Bundle	Specified Numerical Aperture	Measured Clad Index	Measured Peak Core Index	Measured Numerical Aperture
Sumitomo Electric Corp. IGN-05/10	0.35	1.454	1.498	0.36
Fujikura Ltd. FIGH-03-300C	0.4	1.446	1.500	0.40
Sumitomo Electric Corp. IGN-10/13	0.3	1.454	1.496	0.35

Table 4.2. Expected and measured parameters of three silica fiber-optic imaging bundles.

(a)

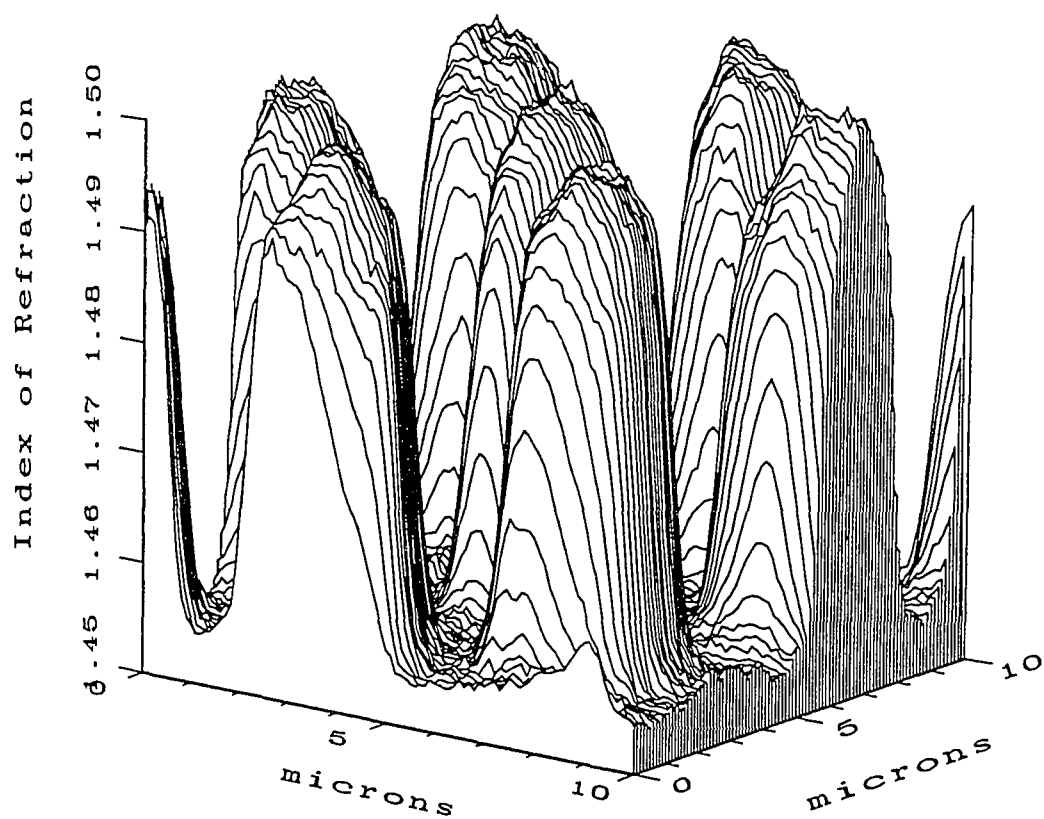


Figure 4.5. Index of refraction of small regions of a) Sumitomo Electric Corp. IGN-05/10, b) Fujikura Ltd. FIGH-03-300C, and c) Sumitomo Electric Corp. IGN-10/13 silica imaging bundles.

(b)

94

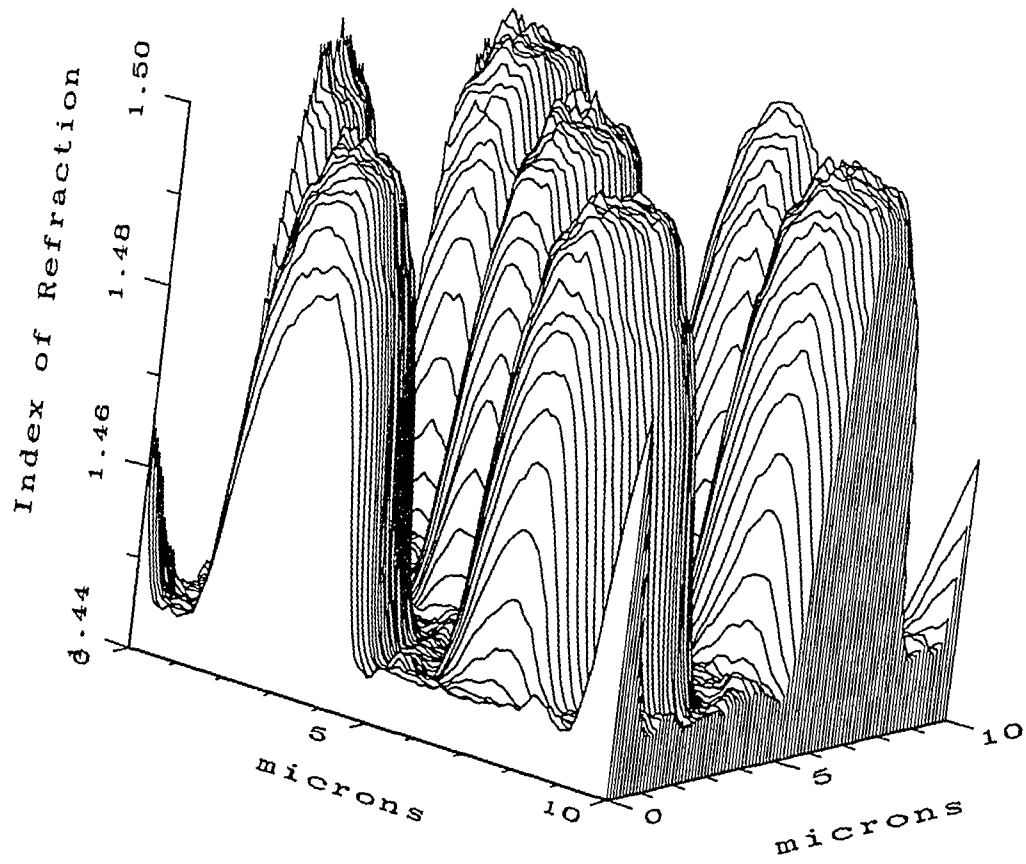


Figure 4.5 (Continued).

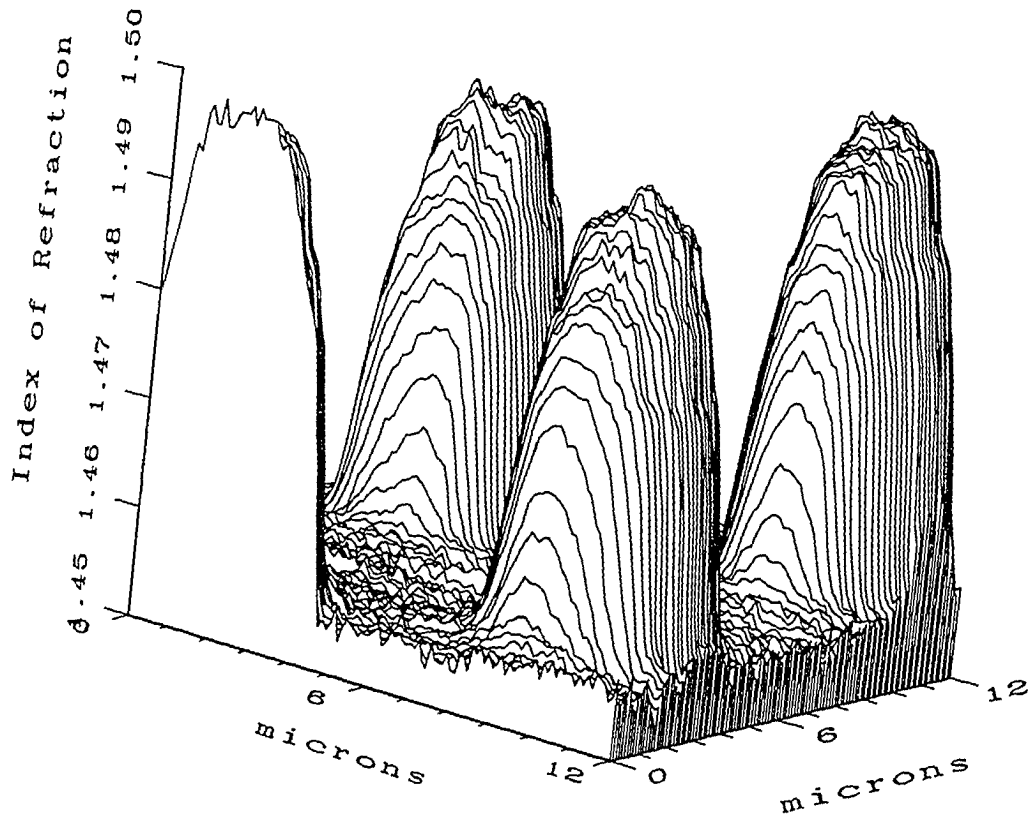


Figure 4.5 (Continued).

Profiles through one of the cores of each bundle are shown in Figure 4.6. Each profile has been fit with a curve described by

$$n(r) = n_{core} - (n_{core} - n_{clad})(r/R)^3, \quad (4.4)$$

where n_{core} and n_{clad} are the values given in Table 4.2, R is the radius of the core profile in Figure 4.6, and r is the radial coordinate (μm). The oscillatory nature of the data at high index values is due to an unknown idiosyncrasy of the Zeiss LSM10 confocal microscope used to collect these images (visible as faint vertical lines in the fiber cores in Figures 4.4).

All three of the bundles can be described as having power law refractive index profiles.^{31,95} This can also be predicted for the Sumitomo IGN-05/10 based on a Sumitomo publication.⁴³ A power law fiber has a refractive index which is maximum at the center of the core and decreases according to

$$n(r) = \sqrt{n_{core}^2 (1 - 2\Delta\rho^q)}, \quad (4.5)$$

where n_{core} is the peak index at the center of the core, $2\Delta = NA^2/n_{core}^2$, $\rho = (r/R)$ is a normalized radial coordinate (unity at the core-clad interface), and q is the (positive) power of the profile.³¹ The refractive index is constant in the clad. In the case of weakly guiding fibers, this becomes

$$n(r) \approx n_{core} (1 - \Delta\rho^q), \quad (4.6)$$

where $\Delta \approx (n_{core} - n_{clad})/n_{core}$ (essentially equivalent to Gloge's definition of $\Delta = (n_{core} - n_{clad})/n_{clad}$)³⁵). For the three bundles evaluated here, $q = 3$.

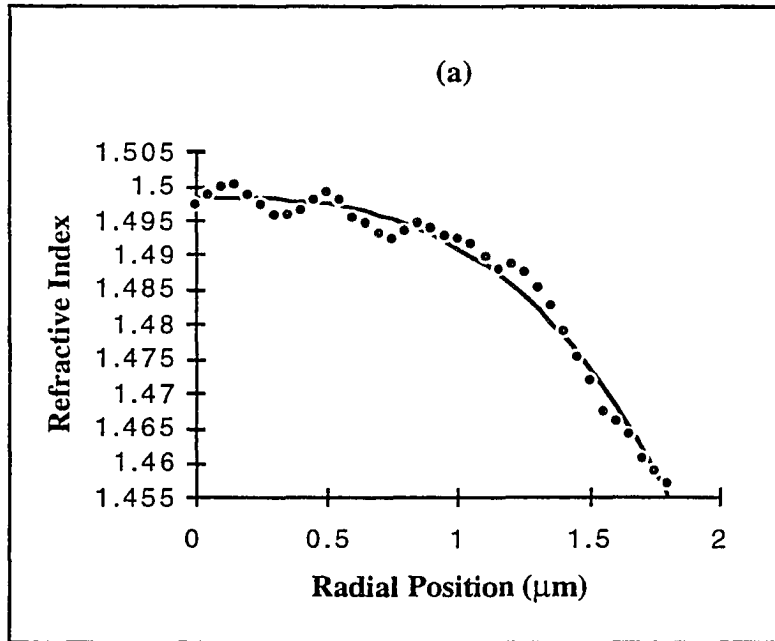


Figure 4.6. Refractive index profiles of a single core in each of three silica fiber-optic imaging bundles. a) Sumitomo Electric Corp. IGN-05/10, b) Fujikura FIGH-03-300C, and c) Sumitomo Electric Corp. IGN-10/13. Each profile has been fitted with a curve described by equation (4.4). (Continued on the following page).

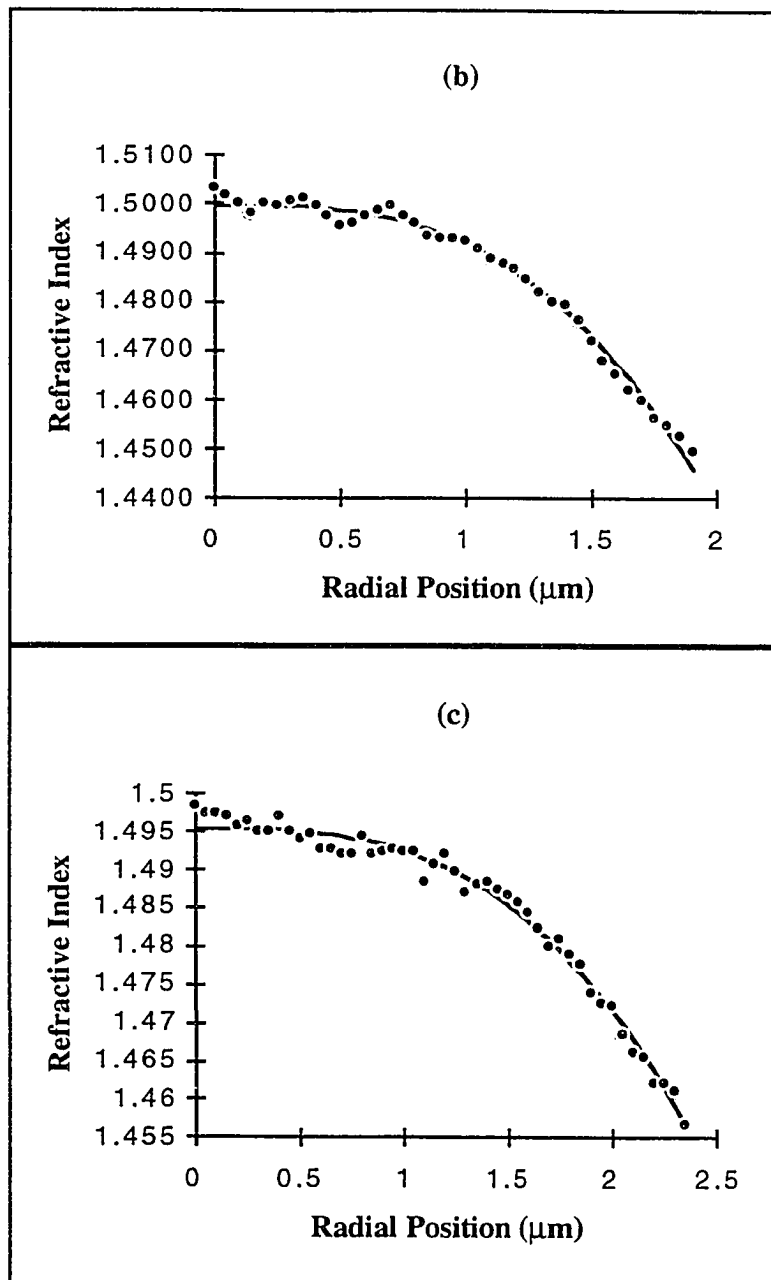


Figure 4.6 (continued).

Core spacing

The resolution of a fiber bundle is a function of several factors, including core size and spacing, crosstalk, fiber misalignment, and cladding modes. For a high-quality bundle with minimal crosstalk, misalignment, and cladding modes, the most important parameter is the core spacing, which determines the sampling frequency of the bundle. The core spacing can be estimated from the number of fibers and picture diameter, and can also be readily measured.

Each of these three bundles is hexagonally packed. The average core center-to-center spacing can be calculated from the manufacturers' specifications with

$$d = \sqrt{\pi(\text{picture diameter})^2 / 2\sqrt{3}(\# \text{ of pixels})}. \quad (4.7)$$

Experimental values can be calculated from images such as those shown in Figure 4.4 with a similar method. Results of these calculations are given in Table 4.3.

Bundle	Specified Core Spacing (center-to-center)	Calculated Core Spacing from Bundle Spec's (picture diam. and # of fibers)	Measured Core Spacing (center-to-center)
Sumitomo Electric Corp. IGN-05/10	~4 μm	~4.3 μm	4.4 μm
Fujikura Ltd. FIGH-03-300C	not specified	4.3 - 5.0 μm	4.7 μm
Sumitomo Electric Corp. IGN-10/13	8 - 9 μm	~7.5 μm	7.8 μm

Table 4.3. Average core spacing in three silica imaging bundles.

Core size and packing fraction

Core size impacts bundle performance in several ways. In general, it is best to have the largest core size possible for a given core spacing. This results in the most bound modes and highest packing fraction, both of which impact the coupling of light into the bundle.

The size of the cores is difficult to measure due to the continuous index of the graded core fibers and noise in the index measurements. The core-clad interface is actually located at the point where the index changes from a constant value in the clad to an increasing value in the core. However, this point cannot readily be determined in the refractive index plots of Figure 4.5. For this reason, an initial index value slightly above that of the clad was chosen as the threshold between core and clad, and a biased packing fraction determined. This biased packing fraction value was then corrected for the error resulting from the initial refractive index threshold being somewhat higher than the actual core-clad interface index, and the core diameter determined using the corrected packing fraction.

The initial (biased) index value separating core and clad was set at approximately 11% of the way from the constant clad refractive index to the maximum core refractive index for each of the bundles (e.g. for the Sumitomo IGN-05/10, peak core index = 1.498, clad index = 1.454, threshold index = 1.4587). This value was chosen empirically based on excluding the majority of the noise in the cladding regions. The biased packing fraction is determined by counting the number of pixels inside the cores (above the threshold value) and dividing by the total number of pixels in the

image. Since each bundle has a known core index profile, the error due to the 11% threshold level can be corrected using equation (4.4) to obtain

$$n(r) = n_{core} - (n_{core} - n_{clad})(r/R)^3 = n_{core} - (n_{core} - n_{clad})(0.89), \quad (4.8)$$

resulting in $(r/R) = 0.96$. The actual packing fraction is then obtained by dividing the measured packing fraction by $(r/R)^2$.

The average core diameter is calculated from the packing fraction, picture diameter, and number of pixels. Assuming round cores in a hexagonally packed bundle, this is given by

$$D = 2R = (\text{picture diameter})\sqrt{\text{packing fraction}/\# \text{ of pixels}}. \quad (4.9)$$

The results of these measurements and calculations are summarized in Table 4.4.

Bundle	Packing Fraction	Core Diameter (Measured, Average)	V ($\lambda = 500\text{nm}$)	Number of Bound Modes ($\lambda = 500\text{nm}$)
Sumitomo Electric Corp. IGN-05/10	52%	3.4 μm	7.5	17
Fujikura Ltd. FIGH-03-300C	60%	3.8 μm	9.6	27
Sumitomo Electric Corp. IGN-10/13	47%	5.6 μm	10.6	33

Table 4.4. Packing fraction, average core diameter, and bound modes of three silica imaging bundles.

Bound modes

For power law profile fibers, the number of bound modes is approximately

$$N_{bm} = \left(\frac{V^2}{2} \right) \left(\frac{q}{q+2} \right), \quad (4.10)$$

where $V = (\pi D/\lambda)NA$, q is the power of the index profile (3 for the bundles discussed here), D is the core diameter, λ is the wavelength, and NA is the fiber numerical aperture.³¹ This is a more general definition than the one given in chapter 3 for a step index fiber, which is the $q = \infty$ case.

For the values tabulated above and a wavelength of 500 nm, the V parameters and number of bound modes in the fibers of these bundles are given in Table 4.4. These values are for circular fibers, and are likely to be slightly different for the somewhat non-circular fibers in these bundles. However, the number of bound modes still serves as a useful metric for comparison of coupling efficiency into these bundles.

For a weakly guiding circular fiber, the linearly polarized modes with the lowest cutoffs were tabulated by Okoshi⁴⁴ (following the work of Gloge³⁵). The fibers in the Sumitomo IGN-05/10 have approximately 17 bound modes. For a circular fiber this would yield LP_{01} , LP_{11} , LP_{21} , LP_{02} , and LP_{31} (lowest 16 modes, with degeneracies). Due to the somewhat hexagonal shape of the fiber cores in the Sumitomo bundle, it is likely that these modes are altered somewhat or perhaps excited with different efficiency than they would be in a round fiber.

The intensity patterns corresponding to the bound modes of the Sumitomo IGN-05/10 are shown in Figure 4.7. In Figure 4.7a, the LP_{01} mode is clearly visible, having been excited by a 0.1 NA illumination beam. Figures 4.7b and 4.7c show higher order modes being successively excited by 0.2 NA and 0.5 NA illumination beams, respectively (Figure 4.7c is identical to Figure 3.5). The fiber NA is 0.35, so the 0.5 NA case is overfilling the fiber, and demonstrates the result for any illumination beam ≥ 0.35 NA. The higher order modes appear to have four and six maxima as a function of azimuthal angle, and are perhaps LP_{21} , and LP_{31} , respectively. Alternatively, they may be some combination of LP_{11} and LP_{21} (these figures were obtained using an unpolarized, white-light source, and therefore all the modes are excited). The fiber modes are wavelength dependent, and therefore these images really represent some composite of the modes for visible wavelengths.

These images were obtained with a 60x/1.4NA Zeiss plan-apochromat microscope objective and a white light source illuminating a 1.1 inch piece of fiber bundle. The unbound modes should be negligible with this length of fiber (see chapter 3), leaving only the bound modes. An approximate (ideal) point spread function for an 0.35 NA beam was deconvolved from the data to obtain the images shown here. The 0.35 NA beam was chosen to correspond to the NA of the fiber bundle, as no light will be exiting the fiber at steeper angles (except some amount in skew rays, which is neglected). The point-spread-function used for deconvolution is only approximate because the beam numerical aperture varies from a minimum of 0.1 to a maximum of 0.35 in Figures 4.7a through 4.7c, respectively, and, therefore, the actual point-spread-function varies between the images. Additionally, the point-spread-function used for deconvolution assumes an evenly illuminated objective pupil, which is unlikely.

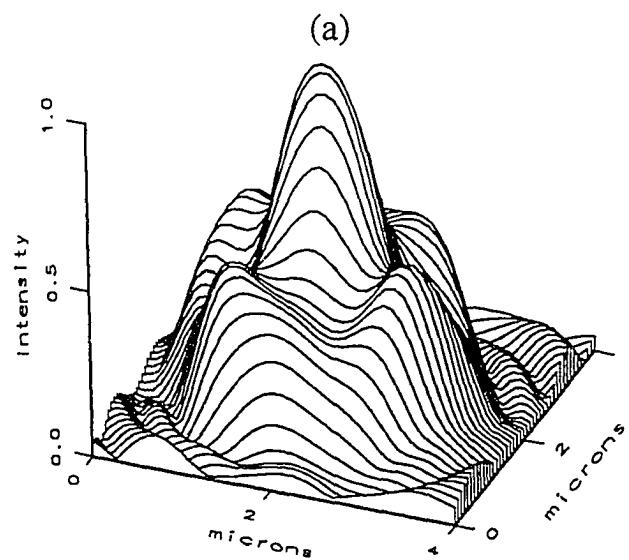


Figure 4.7. Intensity patterns corresponding to the bound modes of a fiber in a Sumitomo Electric Corp. IGN-05/10 0.35 NA fiber-optic imaging bundle. a) 0.1 NA white-light illumination exciting primarily the lowest order mode, b) 0.2 NA illumination exciting several modes, and c) 0.5 NA illumination beam overfilling the fiber and probably exciting all the bound modes.

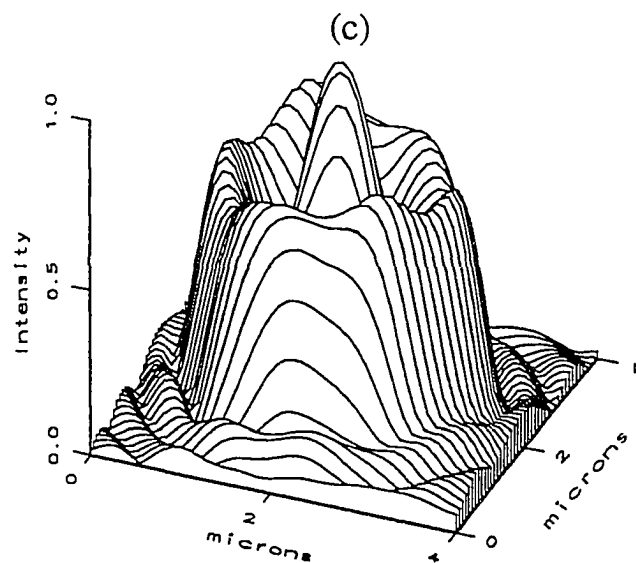
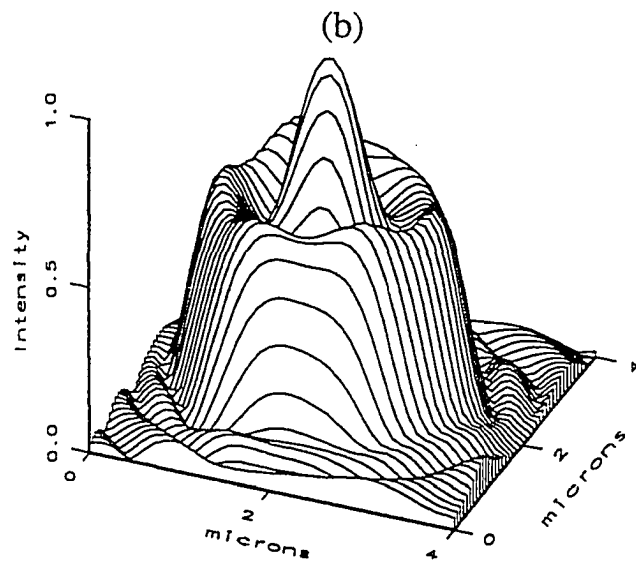


Figure 4.7 (continued).

Coupling

Coupling of light into the Sumitomo IGN-05/10 bundle is angle dependent due to the local numerical aperture (discussed in chapter 3) and the limited number of bound modes. The bound modes of a fiber can be related to the angle of the rays in the fiber, with higher order modes corresponding to steeper ray angles.

This can be modeled for the case of many modes by calculating the core area into which light will be bound as a function of incidence angle. The local numerical aperture at a radius, r , in the core is related to the angle, θ , of the steepest bound ray incident on the fiber by

$$NA(r) = \sin(\theta), \quad (4.11)$$

where the fiber is assumed to be immersed in air ($n = 1$). The local numerical aperture can also be written in terms of the nominal fiber numerical aperture (at the center of the fiber) and the normalized radius, $\rho = (r/R)$, of the portion of the core into which light of this angle, θ , will be bound. This yields, using equations (3.2), (3.3), and (4.5),

$$\begin{aligned} NA(r) &= \sqrt{n(r)^2 - n_{clad}^2} \\ &= \sqrt{n_{core}^2 (1 - 2\Delta\rho^q) - n_{clad}^2} . \\ &= \sqrt{NA^2 (1 - \rho^q)} \end{aligned} \quad (4.12)$$

Equations (4.11) and (4.12) can be combined and rearranged to obtain

$$\rho = q \sqrt{\frac{NA^2 - \sin^2(\theta)}{NA^2}}. \quad (4.13)$$

The coupling efficiency as a function of angle, θ , is determined by the fraction of the core within the normalized radial coordinate, ρ . This can be written

$$\eta(\theta) = PF \left[\frac{\pi r^2}{\pi R^2} \right] = PF[\rho^2] \quad (4.14)$$

where the bundle packing fraction PF has been included to account for light which is coupled into the clad and thereby lost. The predicted coupling efficiency for the Sumitomo IGN-05/10 imaging bundle ($NA = 0.35$, $q = 3$, $PF = 0.52$) is shown in Figure 4.8 (dashed line). The maximum angle of 20 degrees is approximately the steepest angle at which light is coupled into the bundle, based on the specified numerical aperture of 0.35. An experimental plot of the coupling efficiency of a collimated 633 nm beam into this bundle is also plotted in Figure 4.8 (curve marked with solid boxes).

The measured coupling efficiency into this bundle is somewhat higher on-axis than predicted by equation (4.14), and falls off faster with angle than predicted. There are several humps in the experimental result that probably correspond to coupling into each of the bound modes. If the bundle had constant refractive index cores (step index in Figure 3.1) and many modes, the coupling efficiency would be approximately constant up to the angle corresponding to the numerical aperture, and then drop

quickly to zero. The on-axis performance in Figure 4.8 may indicate that the ray model is inadequate to describe this bundle.

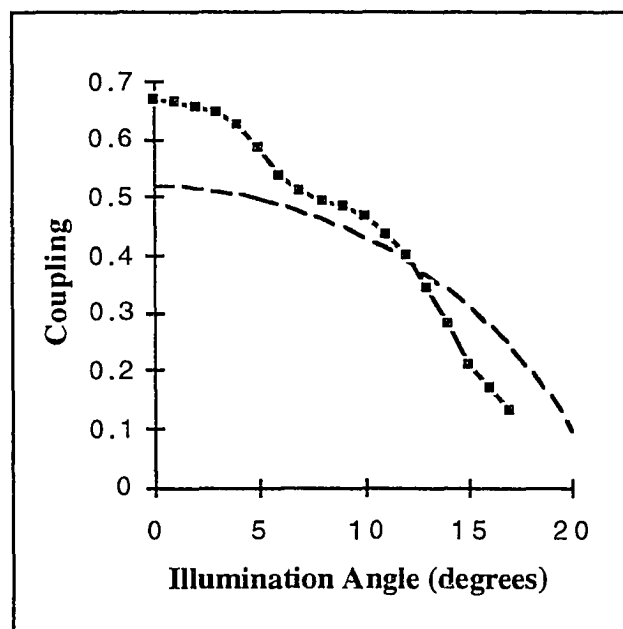


Figure 4.8. Predicted and measured coupling of collimated light into a Sumitomo Electric Corp. IGN-05/10 0.35 NA silica imaging bundle. Illumination angle varies from 0 degrees (on-axis) to 20 degrees, corresponding approximately to the steepest meridional ray bound by the fiber ($\sin(20^\circ) = 0.34$). The predicted coupling is shown with a dashed line and is calculated assuming many modes. The experimental result is marked with solid boxes. Humps in the experimental curve probably correspond to coupling into the few bound modes of the fibers in the bundle. The experimental result was obtained with a 633 nm He-Ne laser.

Crosstalk

We have found experimentally that crosstalk between the elements of a Sumitomo Electric Corp. IGN 05/10 silica imaging bundle is substantially less than predicted by theoretical calculations for a bundle of identical fibers. Figure 4.9 shows the output

intensity from a few fibers in a 2.5 meter long bundle for two different illumination conditions. A 0.3 NA, 633 nm beam was focused onto a single fiber in the bundle to obtain the image in Figure 4.9a. The same illumination beam was defocused slightly to obtain the image of Figure 4.9b. Light in this case is exiting from several fibers. Figures 4.9a and 4.9b are otherwise identical. This shows that negligible crosstalk is occurring.

It is assumed that the lack of crosstalk is due to significant variations in the geometry of the individual fibers in the Sumitomo bundle, as can be seen in Figure 4.4a. It is not known whether the Fujikura bundles will have comparable crosstalk performance.

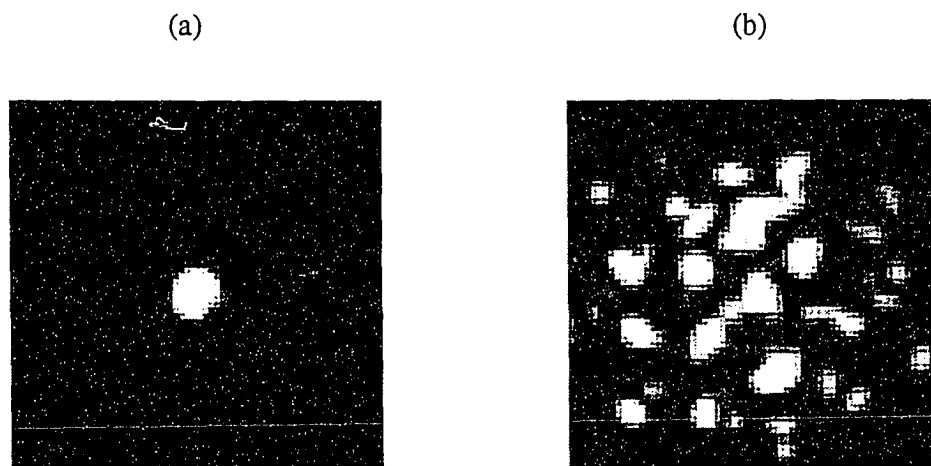


Figure 4.9. Absence of crosstalk in a 2.5m long Sumitomo IGN-05/10 imaging bundle. Figure 4.9a shows the output intensity for a 0.3NA, 633 nm beam focused into a single fiber in the bundle. Figure 4.9b shows the output intensity from the same bundle for a defocused input beam.

Stray light and/or cladding modes

Light that is coupled into the cladding of the bundle may propagate as cladding modes. Cladding modes occur due to a lower refractive index in the buffer surrounding the bundle than in the clad. Light that is focused onto the end of the Sumitomo bundle, but is incompletely coupled into one of the cores, often exits the bundle in a zig-zag like pattern through the cores. This is shown in Figure 4.10, where light is exiting from cores that are not adjacent to the fiber that was primarily illuminated. It is not known whether this is due to cladding modes or simply unbound light which has not reached the buffer. This light exits the bundle at positions related in some complex, unknown manner to the input positions, and, therefore, represents background noise.

Conclusion of bundles evaluation

Based on these results, it appears that the Sumitomo IGN-05/10 and Fujikura FIGH-03-300C bundles should give similar resolution, while the Sumitomo IGN-10/13 will be significantly worse. If substantial crosstalk occurs in the FIGH-03-300C and other Fujikura high-resolution bundles, then their resolution will be inferior to that of the Sumitomo IGN-05/10. The efficiency of the Fujikura high-resolution bundles will be better than that of the Sumitomo bundles due to the higher packing fraction and higher numerical aperture. These two parameters work together to make more bound modes available for light transmission for bundles of comparable diameter and pixel count.

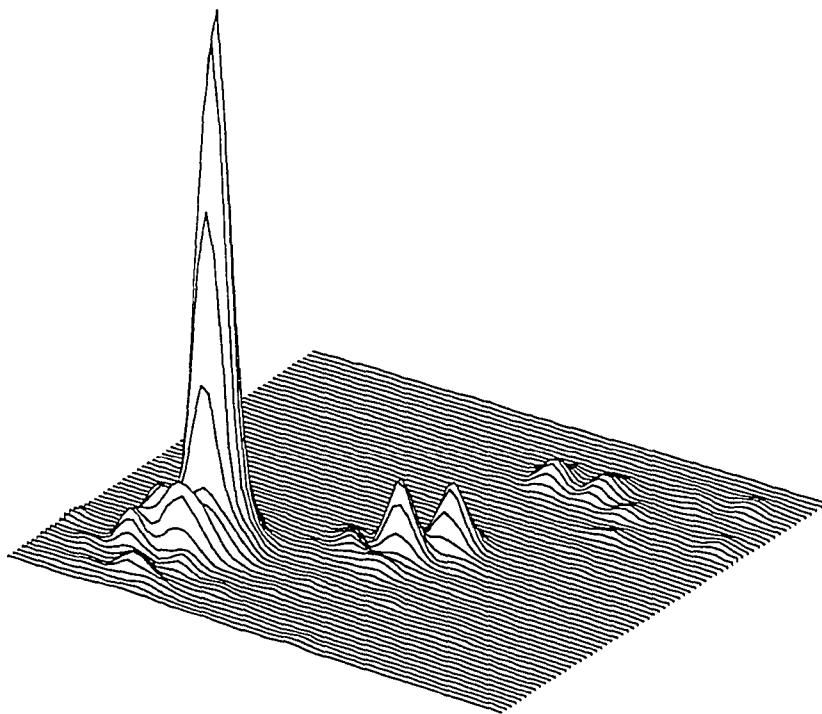


Figure 4.10. Stray light and/or cladding modes in a Sumitomo Electric Corp. IGN-05/10 fiber-optic imaging bundle. Light is exiting from fibers in the imaging bundle that are not adjacent to the fiber that was primarily illuminated.

5. FIBER-OPTIC IMAGING-BUNDLE CONFOCAL MICROSCOPE

This chapter discusses the implementation of confocal microscopy through a fiber-optic imaging bundle. The influence of the imaging bundle on the system performance is described. Two systems have been built and their design and performance are discussed. One system is a modified Zeiss LSM10 beam-scanning confocal microscope. The Zeiss system scans images of the source and detector pinholes across the sample in a two-dimensional raster scan. Because of the long frame time (≥ 2 seconds), this is suitable primarily for examination of fixed samples. The second system is a real-time (thirty frames per second) slit-scanning design. This system scans a line of illumination across the sample and collects the resulting reflected or fluorescent light with a row of detectors. The rapid image acquisition of this system comes at the cost of reduced optical-sectioning performance.

The fiber-optic imaging-bundle confocal microscope was depicted in Figure 1.4. The fiber bundle in this system relays the images of the confocal source and detection pinholes from the original sample plane of an epi-illumination confocal microscope to a new sample plane at the distal end of the fiber bundle. The goal of this design is to gain the benefits of confocal microscopy without being restricted to samples that can be placed on a microscope stage. This allows inspection of biological and industrial samples in restricted environments. Possibilities include environmental chambers and in-vivo medical imaging, potentially even in a body cavity. This holds promise beyond that of conventional endoscopy due to the optical-sectioning effect. The optical-sectioning effect allows in-vivo subsurface imaging to be performed by

eliminating out-of-focus light from the intervening tissue, as shown in Figure 2.7. Perhaps the most exciting possibility is the potential for performing in-vivo optical biopsies, enhancing conventional pathology techniques.

Confocal microscopy is an atypical application for flexible imaging bundles, which are usually used for endoscopy. It is generally desirable in endoscopy to image a large field-of-view at low magnification and with a large depth-of-field. This requires a distal objective that magnifies the end of the fiber bundle several times.^{96,97} The optical-sectioning effect is inversely proportional to depth-of-field, being most pronounced in high NA systems. To obtain adequate numerical aperture for good optical sectioning, it will be necessary to demagnify the end of the fiber bundle several times (e.g., approximately three times for an 0.35 NA imaging bundle and desired object space NA of 1.0). Thus, while in endoscopy the field may be several times larger than the bundle diameter, in confocal microscopy it will typically be several times smaller than the bundle diameter. The design considerations for the distal imaging lens in the two applications are therefore quite different.

As discussed in the previous chapter, fiber-optic image-bundles are space-variant imaging devices. Therefore, the fiber-optic imaging-bundle confocal microscope will also have space-variant imaging performance.

5.1. Fiber-optic confocal microscope (single fiber)

Fiber-optic confocal microscopes have been built using a single optical fiber.^{3,4,5,6} In this type of system, depicted in Figure 5.1, the optical fiber acts as both the source pinhole and the detection pinhole. The modes and flexibility of the optical fiber yield

some advantages over confocal microscopes that use physical apertures for the pinholes. When combined with micro-optics for the final objective, the size and flexibility of the fiber allows confocal microscopy to be implemented in a variety of locations that would otherwise be inaccessible.

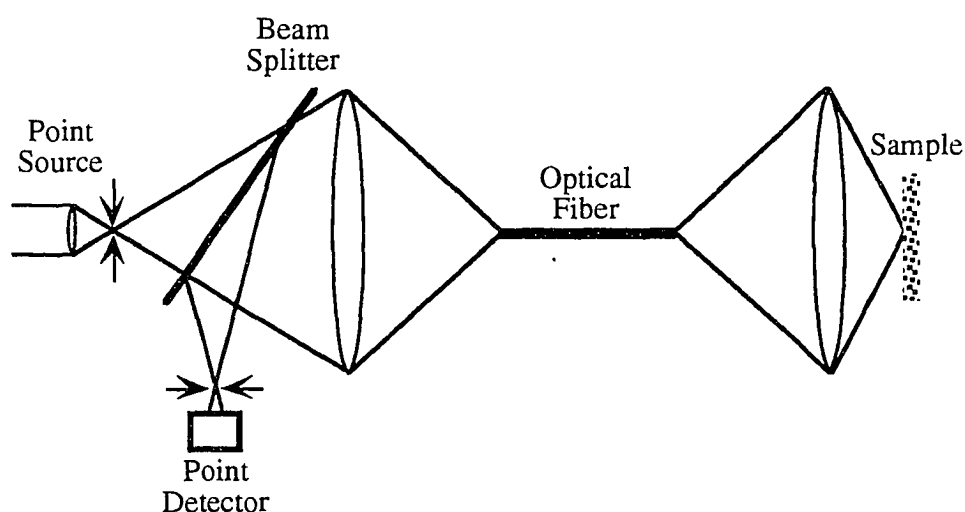


Figure 5.1. Fiber-optic confocal microscope (single fiber).

A second, more subtle, effect with optical fibers is the effective geometry of the pinholes obtained due to the bound modes of the fiber. The field distribution of the source and detection "pinholes" is a function of these modes, as well as their coupling to the physical source and detector at the other end of the fibers. The lowest bound mode in round optical fibers is approximately Gaussian.³¹ Thus, the use of single-mode optical fibers as source and detection pinholes yields approximately Gaussian pinhole images at the sample. More sophisticated effects such as differential phase or differential amplitude measurements can be obtained by using the higher order modes of the fiber.^{98,99}

The fiber-optic confocal microscope (single fiber) has one major disadvantage compared to the fiber-optic imaging-bundle confocal microscope. In order to collect an image, it is necessary to scan the fiber, imaging lens, or sample at the distal end of the fiber. Thus, the mechanism in the region of the sample must be more complicated than in the fiber-optic imaging-bundle design. It is necessary in both designs to incorporate a focusing mechanism at the distal end of the fiber or fiber-bundle to image a specific plane within the sample.

5.2. Fiber-optic imaging-bundle confocal microscope

As described in chapter 2, the unique optical-sectioning capability of confocal microscopy relies on the combined effect of source and detection apertures (pinholes and/or slits) imaged onto the same location in the test sample. The fiber-optic imaging-bundle confocal microscope accomplishes the same thing, but in locations restricted only by the ability to position the distal fiber end and imaging lens.

We have implemented the fiber-optic imaging-bundle confocal microscope by modifying a Zeiss LSM10 confocal microscope as shown in Figure 5.2.^{100,101,102} A Sumitomo Electric Corp. IGN-05/10 imaging bundle (10,000 fibers, 0.35 NA, ≈ 3.4 μm core diameter, ≈ 4.4 μm core spacing center-to-center) was used in this system. Figure 5.3 shows a set of images obtained through the imaging bundle. The microscope was operated in fluorescence mode, where a dichroic beamsplitter and/or a long-wave pass filter is used to screen out reflected illumination light and detect only fluorescent light. Low resolution images of a business card coated with fluorescent ink were obtained in both confocal and conventional (non-confocal) modes. The distal lens, L2, was implemented with a back-to-back pair of microscope objectives. Lens

L2 had a magnification of approximately 0.3x, a final NA at the sample of 0.07 (limited by one of the objectives), and a field-of-view 1.5 mm in diameter. This is a very low numerical aperture for a confocal microscope, but still demonstrates the optical-sectioning effect. Argon laser illumination at 488 nm and 514 nm was used for this experiment.

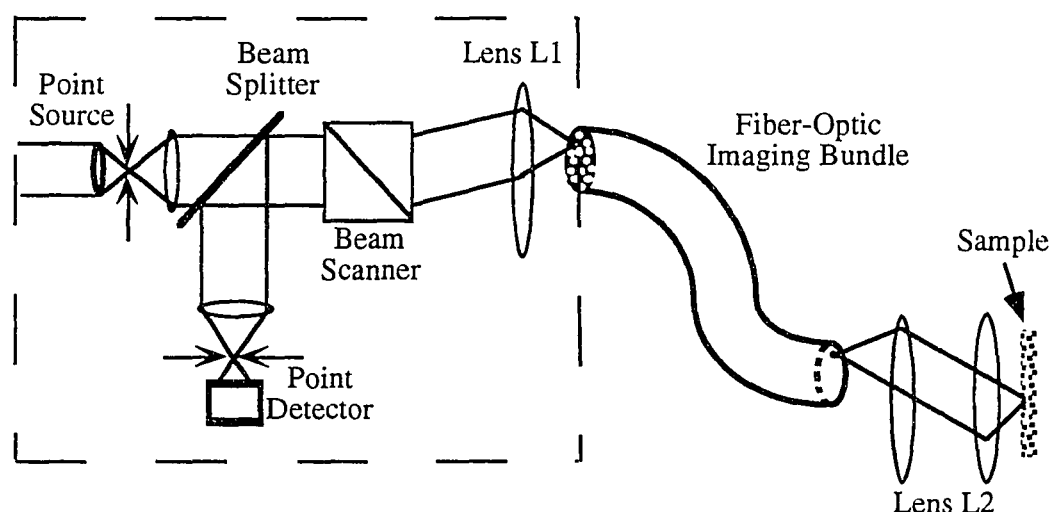


Figure 5.2. Modification of a commercial epi-illumination confocal microscope to include a fiber-optic imaging-bundle. The components inside the dashed box represent a simplified diagram of a Zeiss LSM10 confocal microscope.

Figures 5.3a and 5.3b show images of the business card collected in the confocal scanning mode of the Zeiss LSM10. Figure 5.3a is an in-focus image, while Figure 5.3b is an out-of-focus image. The amount of light present in Fig. 5.3b has fallen off significantly with defocus, demonstrating the optical-sectioning effect. Figures 5.3c and 5.3d show the corresponding images collected in the non-confocal scanning mode. The non-confocal scanning mode is obtained by increasing the detection pinhole diameter as much as possible, approximating the system shown in Figure 2.2. Figure

5.3c is the in-focus image and resembles the in-focus confocal image of Fig. 5.3a. Fig. 5.3d is the out-of-focus image, and shows a loss of high spatial-frequency information (blurring of fine detail), but roughly the same amount of light as the in-focus image. Fig. 5.3c. Figures 5.3b and 5.3d are defocused by the same amount relative to Figures 5.3a and 5.3c, respectively.

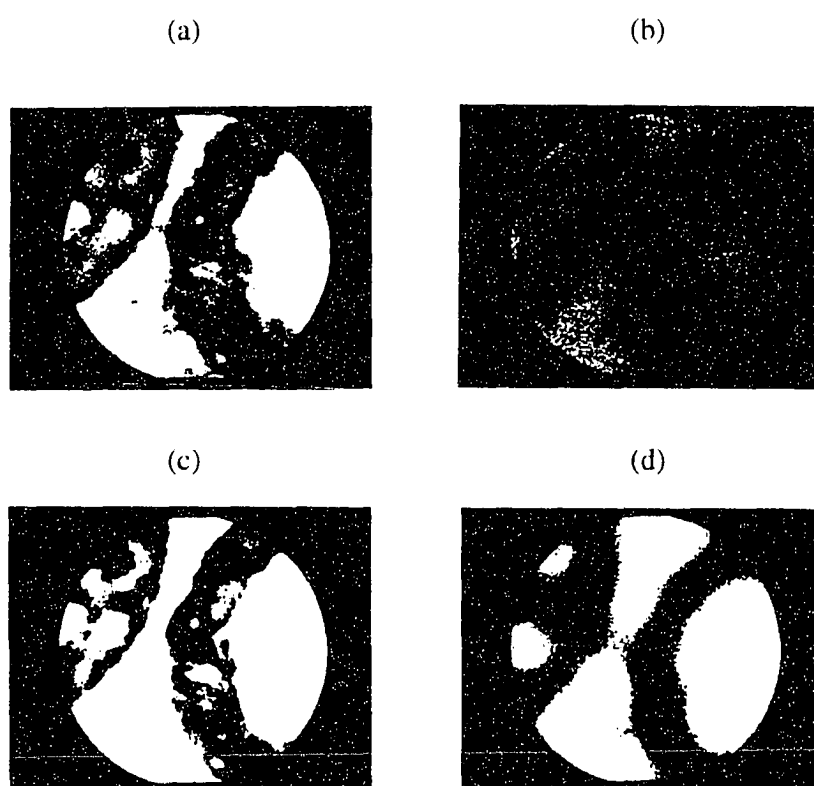


Figure 5.3. Comparison of confocal and non-confocal microscope images collected through a fiber-optic imaging bundle (system description is in the text). Sample is a business card coated with fluorescent ink. Figure 5.3a is the in-focus confocal image and Figure 5.3b is the out-of-focus confocal image. Figure 5.3c is the in-focus non-confocal image and Figure 5.3d is the out-of-focus non-confocal image. Figures 5.3b and 5.3d are defocused by the same amount relative to Figures 5.3a and 5.3c, respectively.

The imaging performance of the fiber-optic imaging-bundle confocal microscope is determined primarily by how well the imaging bundle relays the images of the source and detection apertures (pinholes and/or slits) from the nominal sample plane at the proximal end of the bundle to the new sample plane at the distal end of the bundle. The ideal bundle would have a large number of fiber elements of very small size and spacing (e.g. less than a wavelength), high packing fraction, high coupling efficiency, and negligible transmission losses. Such a bundle would allow the source and detector aperture images to be well sampled and therefore accurately relayed to the new sample plane. It is the deviation of fiber-optic imaging bundles from this ideal condition that limits the imaging performance of this system.

As discussed in the previous chapter, a fiber-optic imaging bundle is an array of fibers in fixed relative positions. It is tempting to assume that the analysis of the fiber-optic confocal microscope can be extended to an array of such devices to describe the imaging-bundle system. In order for this to be the case, it would be necessary to couple identically (or at least with known efficiency) to the bound modes of each fiber within the bundle. This could be accomplished with a system that scans carefully across the bundle, precisely imaging the source and detector pinholes onto each fiber. Although such a system could be implemented, it is unlikely that scanning can be performed rapidly enough for an in-vivo system. An industrial inspection tool or biological research instrument might benefit from such a scan system if the speed requirements for image acquisition are modest.

There are four disadvantages of the fiber-optic imaging-bundle confocal microscope as compared to a conventional confocal microscope. They are the optical-sectioning

performance limitation due to the fiber size and spacing in the bundle, the lateral-resolution limitation due to the fiber spacing in the bundle, field-of-view limitations due to the limited number of fibers in the bundle, and radiometric losses.

Modification of a confocal microscope for fiber-optic imaging bundle operation

The implementation of confocal microscopy through a fiber-optic imaging bundle can be accomplished by a relatively simple modification to an epi-illumination confocal microscope. Since the imaging bundle relays the nominal sample plane of the microscope to some other location, the proximal end of the bundle is mounted in the microscope in place of the sample holder. The distal end of the bundle and the final lens can now be placed as desired, independent of the location of the microscope (within the limits of length and flexibility of the bundle and size of the distal lens).

This is shown in Figure 5.2, where the components within the dashed box are those of a Zeiss LSM10 beam-scanning confocal microscope (simplified diagram). The Zeiss' sample stage has been replaced with a stage in which one end of the imaging bundle is mounted. The other end of the bundle is then imaged onto the new sample plane with a pair of infinity-corrected microscope objectives placed back-to-back.

A 10x / 0.3NA Zeiss Plan-Neofluor objective (lens L1) was used to couple light to the imaging bundle. The source pinhole in the Zeiss confocal microscope is implemented with a collimated laser beam, yielding a diffraction limited illumination spot on the face of the imaging bundle. The detection pinhole is significantly larger, such that its projected image is determined by geometrical demagnification, rather than being diffraction limited. A second 10x / 0.3NA infinity corrected Zeiss Plan-Neofluor objective was used to collimate the light leaving the bundle at the sample end, and the

final (infinity corrected) objective adjacent to the sample was chosen to yield the desired magnification.

When adapting a microscope for imaging-bundle operation, the numerical aperture of the illumination beam on the proximal end of the bundle should be less than, or equal to, the NA of the fibers. Overfilling the fibers will result in lost light due to the inability of the fibers to guide the steepest rays. There may be an advantage in illumination efficiency when the bundle is underfilled. Figure 4.8 shows that the coupling efficiency into the Sumitomo IGN-05/10 imaging bundle falls off quickly with incidence angle. Therefore, reducing the numerical aperture of the illumination beam may reduce the coupling losses.

The numerical aperture of the detection beam should generally match or exceed the NA of the bundle. This maximizes the coupling efficiency from the bundle to the detector. Light loss in the illumination arm can be accommodated by using a brighter source. However, because there is usually a limit to the irradiance that a sample can tolerate, the efficiency of the detection path is very important.

The field-of-view of the microscope being modified for image-bundle operation needs to be at least the size of the fiber bundle. In a beam-scanning system, this may be smaller than what is normally obtained with a given objective. The Sumitomo IGN-05/10 imaging bundle used in modifying the Zeiss microscope has a numerical aperture of 0.35 and a diameter of 0.5 mm. The field-of-view of the Zeiss microscope with a 10x / 0.3NA objective is approximately 2 mm in diameter. The scan range can be cut down by a factor of four from the design conditions for this objective.

Therefore, the objective needs to be well corrected for aberrations over a smaller field than is normally required.

Bundle characteristics

Fiber size and spacing

As indicated above, the imaging performance of the fiber-optic imaging-bundle confocal microscope is determined by how well the imaging bundle relays the images of the source and detection pinholes. This depends on the relative sizes of the fibers and the pinhole images. There are three possible conditions: 1) the fibers are smaller than the pinhole images; 2) the fibers are larger than the pinhole images; 3) the fibers and the pinhole images are approximately the same size.

In order to accurately transmit the images of the source and detector apertures, the individual fiber elements in the bundle should be several times smaller than the source and detector aperture images (condition 1). There are two disadvantages to this condition. First, fibers that are sufficiently small to meet this criteria are likely to be single-mode, and will suffer from high input coupling losses.⁵⁸ Second, it significantly increases the number of fibers necessary to collect an image due to the use of several fibers per pixel.

Fiber core diameters can be decreased without reducing the number of modes by increasing the index difference between the core and cladding. This also results in an increased fiber NA. The maximum lossless magnification at the distal end of the bundle is now limited by the higher NA (unless the bundle is underfilled, which results again in fewer modes). Fiber core diameters can also be decreased without a reduction

in the number of bound modes by using a shorter wavelength. However, many applications of confocal microscopy rely on fluorescent dyes that require specific illumination wavelengths. Furthermore, losses in imaging bundles appear to increase rapidly in the ultraviolet, limiting the potential usefulness of shorter wavelengths.^{42,45}

High-resolution flexible silica bundles such as those made by Sumitomo and Fujikura have at most 10,000 elements, and therefore can transmit an image of up to 10,000 pixels (e.g. 100 x 100). The Zeiss LSM10 confocal microscope, by comparison, readily collects 512 x 512 images for a total of 262,144 pixels. The number of pixels available in the fiber-optic imaging-bundle confocal microscope will be even more severely limited if multiple fibers are used to sample the pinhole images at each scan position.

It is also possible to use a bundle with fiber elements that are larger than the pinhole images (condition 2). This reduces both the resolution and radiometric performance of the system. The resolution is reduced due to the increase in size of the pinhole images when they are relayed by the bundle. A pinhole image that is smaller than a single fiber will be relayed to the other end of the bundle with an effective size approximately equal to that of the fiber. This results in an increase in the normalized radial parameter, v_p , and the resulting loss in axial resolution discussed in chapter 2. The radiometric degradation arises because the detector pinhole will be imaged onto a small portion of a single fiber element, while the collected light will be emitted from the entire element. Thus, much of the light will be rejected by the detector pinhole and the signal will be reduced.

Based on the above discussion, we have concluded that the optimum condition for this system is pinhole image sizes that are approximately equal to the size of the fibers (condition 3). This maximizes the available number of pixels and, apart from field-of-view, does not significantly degrade the resolution of the system.

Numerical aperture

The numerical aperture of the light in the fiber bundle will impact the optical-sectioning and radiometric performance of the system. It is possible to underfill the fibers, and, therefore, the beam NA is more relevant than the bundle (fiber) NA. The optical-sectioning performance is determined by the beam NA in conjunction with the size of the source and detection pinhole images at the sample. As shown in chapter 2, the optical-sectioning performance of a confocal microscope is determined by the normalized radial parameter, v_p , and the normalized axial parameter, $u = \frac{8\pi}{\lambda} \sin^2\left(\frac{\alpha}{2}\right)z$, where $NA = n\sin(\alpha)$ (see Figure 2.3). In order to obtain the thinnest optical section possible, we would like to minimize v_p while maximizing the numerical aperture at the sample (to obtain a large variation in u for a small variation in axial position, z). With minimum pinhole images equal to the size of a fiber in the bundle, this can be accomplished by underfilling the fiber and maximizing the distal lens magnification. The lateral resolution (sampling interval of the fibers) also increases with the distal magnification, albeit at the expense of field-of-view.

The coupling efficiency into a Sumitomo IGN-05/10 imaging bundle is shown as a function of incidence angle in Figure 4.8. Based on these results, it appears that the system efficiency may be increased by underfilling the bundle. This increased coupling efficiency is due to the local numerical aperture of the gradient-index core

fibers in the bundle. Light that is incident at shallow angles effectively "sees" a larger diameter core into which it can be bound than light that is incident at steep angles.

Bundle size

The number of fibers in the imaging bundle provides an upper limit to the number of pixels in an image collected through the bundle. The Sumitomo IGN-05/10 imaging bundle has 10,000 fibers, which is a small fraction of the number of pixels in typical confocal systems. It is desirable to obtain a bundle with the largest possible number of fibers. The upper limit on the desired number of fibers in the bundle will be determined primarily by mechanical constraints. Thick bundles will be able to reach fewer locations than thin bundles. This is particularly important in applications where space is limited, such as catheter-based medical devices. Additionally, the stiffness of silica bundles increases quickly with bundle diameter, making all but the thinnest bundles impractical for some applications. Silica imaging bundles with at least 250,000 fibers have been built and were used in an industrial application where size and flexibility were not crucial.⁴³ Leached image bundles are highly flexible, and may be suitable in applications where a large number of fibers is necessary.

Bundle materials

It is important in the fiber-optic imaging-bundle confocal microscope to use the highest resolution bundles available. This provides the best optical-sectioning performance for a given distal lens magnification. Of the bundle types discussed in chapter 4, silica imaging bundles have a higher resolution than the soft glass or plastic bundles. Soft glass bundles have core center-to-center spacings as small as 6 μm , which is somewhat inferior to the 4.4 μm spacing measured for the Sumitomo IGN-

05/10 silica bundle. Plastic imaging bundles have a minimum fiber spacing of 9 μm . The low cost and high flexibility of plastic imaging bundles may make them a logical choice if higher resolution bundles become available. If the distal magnification could be set arbitrarily, then the bundle resolution would be less important, and the fiber material could be chosen based on flexibility, losses, and cost (although bundle size may still be a limitation in some applications).

Scanning

As discussed in chapter 2, it is necessary to scan the source and detection pinhole images across the sample in order to form an image in the confocal microscope. Since the proximal end of the bundle is located in the nominal sample plane, any of the schemes used for scanning in confocal microscopy may be used.

It should be noted that scanning the bundle ends to operate in the dynamic-scanning mode (described in chapter 4) is not as difficult as scanning a single optical fiber far enough to implement confocal microscopy. In order to effectively implement dynamic scanning, it is necessary to laterally scan the bundle ends through a distance of approximately four fibers.⁷⁸ For a high-resolution silica imaging bundle with center-to-center fiber spacing of 4 - 5 μm , this requires a scan range of approximately 16 - 20 μm . In a fiber-optic confocal microscope (single optical-fiber), the required scan range is the product of the diameter of the field and the magnification of the optics at the distal end of the fiber. For reasonable values of field and distal magnification, say 100 μm and 10x, respectively, this requires a scan range of 1 mm. This is two orders of magnitude greater than necessary for dynamic scanning of an imaging bundle. A magnification of 10x is typical of what would be required to obtain a numerical

aperture at the sample on the order of 1.0 when using a single-mode fiber with NA = 0.1.

Even so, dynamic scanning is not likely to be a useful technique in the fiber-optic imaging-bundle confocal microscope, because it is necessary to scan the two ends of the bundle rapidly, and in unison, during the collection of each pixel. This will add a great deal of mechanical complexity to the system, and will be unrealistic in most designs.

Optical sectioning (axial resolution)

The axial resolution of a confocal microscope depends on the size of the source and pinhole images at the sample. As discussed above and in chapter 2, the optimum optical-sectioning performance comes about with small pinhole images and high numerical apertures. In this section, we compare the optical-sectioning performance of the Zeiss LSM10 modified to include an imaging bundle (Figure 5.2) with the performance of the unmodified Zeiss.

The axial resolution of a confocal microscope varies inversely with the normalized pinhole radius parameter, v_p , as discussed above and in chapter 2. We would like to minimize this parameter as much as possible without negatively impacting other important parameters such as field-of-view and radiometric performance. The parameter v_p (repeated here for convenience) is given by

$$v_p = \frac{2\pi}{\lambda} \sin(\alpha) r_p = \frac{2\pi}{\lambda_o} (NA) r_p, \quad (5.1)$$

where $NA = n \sin(\alpha)$ and r_p = pinhole radius. The NA in this equation is the numerical aperture of the beam, which is not necessarily equal to the NA of the fiber bundle.

Several silica imaging bundles were evaluated in the previous chapter. Two of these bundles are among the highest resolution bundles that are commercially available. The Sumitomo Electric Corp. IGN-05/10 was found to have an average core diameter of $3.4 \mu\text{m}$, core spacing (center-to-center) of $4.4 \mu\text{m}$, numerical aperture of 0.35 (specified), and approximately 17 bound modes ($\lambda = 500 \text{ nm}$). The Fujikura Ltd. FIGH-03-300C has an average core diameter of $3.8 \mu\text{m}$, core spacing of $4.7 \mu\text{m}$, numerical aperture of 0.4 (specified) and 27 bound modes ($\lambda = 500 \text{ nm}$). The Sumitomo bundle has 10,000 fibers, while the Fujikura bundle has 3,000 fibers. Similar Fujikura bundles with up to 10,000 fibers in an approximately 0.5 mm diameter bundle are available.⁵⁹ We discuss below the relaying of the pinhole images in terms of these bundles.

The minimum v_p in the fiber-optic imaging-bundle confocal microscope is limited by the fiber core diameter. The v_p parameter can be calculated from the average core radii and bundle NA (assuming the fibers are not underfilled, which is discussed below). The minimum value at $\lambda = 500 \text{ nm}$ is $v_p = 8$ for the Sumitomo bundle and $v_p = 10$ for the Fujikura bundle. These values of normalized pinhole radii are somewhat larger than optimum for good optical sectioning in a confocal microscope.¹² For example, the refractive index measurements described in appendix A were performed with a diffraction-limited ($v_p = 0$) source pinhole image and a $v_p = 4$ detection pinhole image.

The normalized pinhole radius can be reduced by using an imaging bundle with smaller fiber cores. Silica image bundles with core diameters as small as 1 micron and core spacings (center-to-center) as small as 1.7 micron have been produced. These core sizes yield single-mode operation at visible wavelengths.⁵⁸ The minimum normalized v_p parameter at $\lambda = 500$ nm for a pinhole size of one fiber ($r_p = 0.5$ microns) is $v_p = 2.5$. These values are significantly better than what we obtained with the multi-mode bundles and good resolution (both axial and lateral) can be expected with these single-mode imaging bundles. One disadvantage of single-mode bundles is high input coupling losses which may result in a low SNR. Losses of these single-mode bundles are discussed in the paper by Kiat, et. al.⁵⁸ These bundles are not commercially available, and an attempt to obtain one for this project was unsuccessful.

Reflection-mode axial resolution

To evaluate the optical-sectioning performance of the imaging bundle system of Figure 5.2, the Zeiss LSM10 was operated in the **x-z** mode with a front-surface mirror in the sample plane. In the **x-z** mode, the microscope scans a single line (**x**) in the image while axially scanning the mirror through focus (**z**). Figure 5.4a shows the result of this experiment with the unmodified microscope and Figure 5.4b shows the result when the imaging bundle is included in the system. In both cases, a bright line can be seen in the center of the image when the mirror passes through focus (at a slight angle because the mirror is tilted). However, there is significant spatial variation in the image obtained with the bundle. The vertical lines through the image correspond to individual fibers within the bundle, and the variations between them depend on the coupling efficiency into the fibers.

Figure 5.5 shows the sectioning performance of the two systems at a single point in the center of the field. The data plotted in this figure come from the vertical lines delineated by arrows in Figures 5.4a and 5.4b. The curve marked with triangles is the performance of the unmodified LSM10 and the curve marked with circles is the performance of the LSM10 equipped with the fiber-optic imaging bundle. Helium-neon laser illumination at 543 nm was used in this experiment. For the microscope alone (without the fiber bundle), a 20x / 0.5NA objective was used. In this case, the diffraction-limited ($v_p = 0$) source pinhole image is approximately 1.3 μm in diameter and the $v_p \approx 4$ detector pinhole image is approximately 2.5 - 3 μm in diameter. When the imaging bundle is included in the system, a 10x / 0.3NA objective on the Zeiss LSM10 projects onto the bundle face source and detection pinhole images approximately 2.2 μm and 4 μm in diameter, respectively. Both pinhole images will be approximately 3.4 μm in diameter at the distal end of the bundle (the size of a single fiber core). A 10x / 0.3NA and 20x / 0.5NA pair of objectives was used to image the distal end of the bundle onto the sample, demagnifying these projected pinholes to slightly over 1.7 μm in diameter (due to the finite point-spread-function of the 10x / 20x lens pair). This results in normalized source and detection pinhole image radii of $v_p \approx 5$.

As seen in Figure 5.5, the optical-sectioning performance is almost identical at these points in the two images, showing that good sectioning can be obtained through the imaging bundle. The sectioning performance shown in Figure 5.5 is worse than the ideal performance obtainable in confocal microscopy due to the relatively large

pinhole images used. However, the comparison is valid because approximately the same pinhole image sizes were used with and without the bundle.

(a)

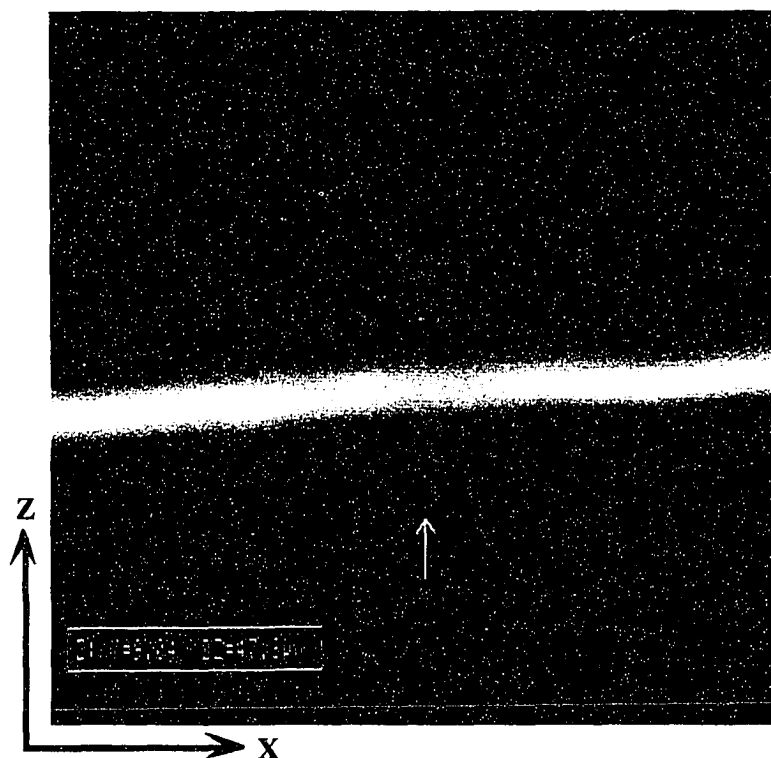


Figure 5.4. Optical-sectioning performance of the Zeiss LSM10 confocal microscope with and without a fiber-optic imaging bundle. Figure 5.4a shows the performance of the commercial microscope. Figure 5.4b shows the performance of the system when modified to include a fiber-optic imaging bundle. (xz scans). (Continued on next page).

(b)

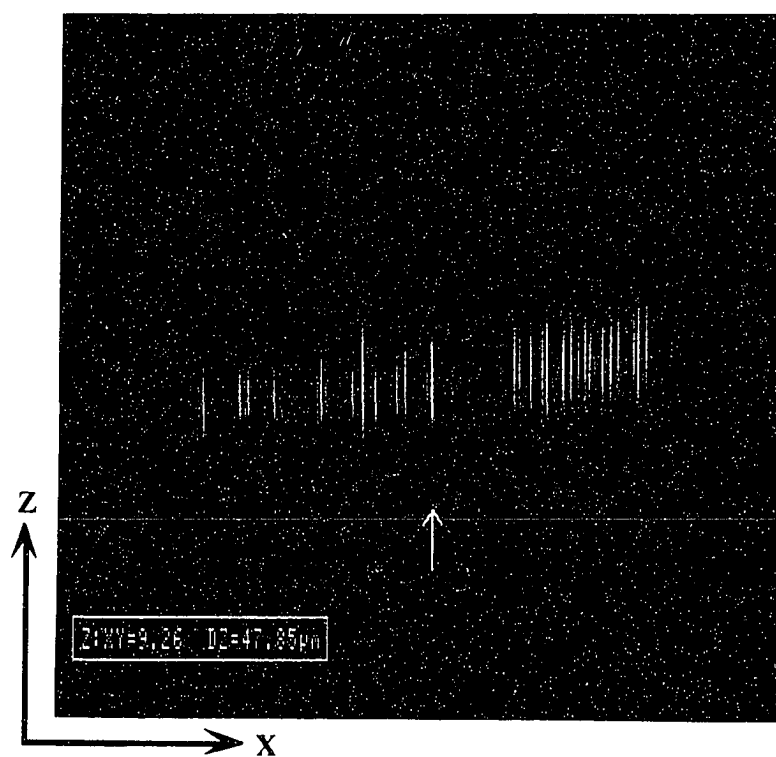


Figure 5.4 (continued).

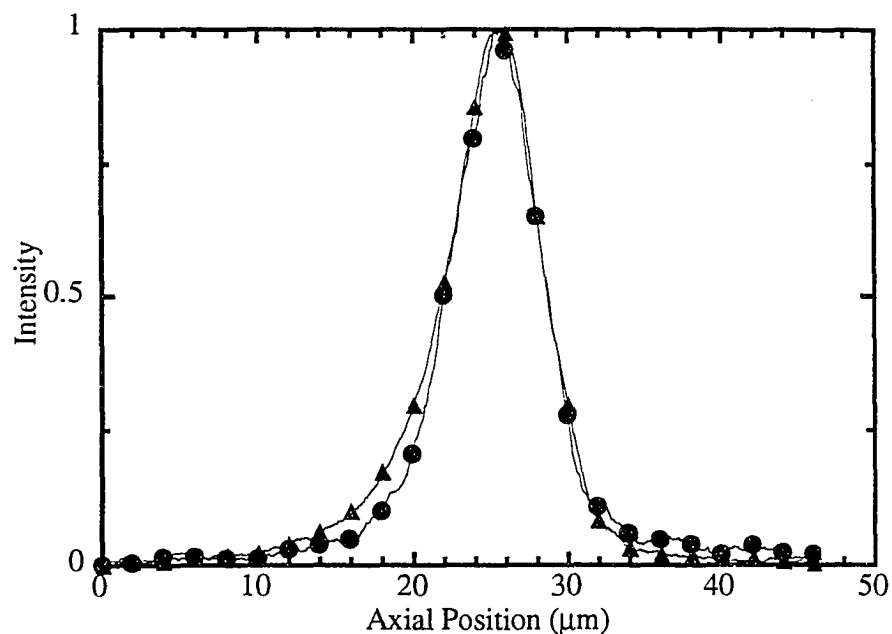


Figure 5.5. Optical-sectioning performance at the center of the field in the Zeiss LSM10 confocal microscope. Comparison of system with (circles) and without (triangles) a fiber-optic imaging bundle.

This experiment was repeated with the system shown in Figure 5.6. This system allows precise positioning of the pinhole images onto a single fiber in the fiber bundle, and greater control over the optical elements of the system than in the modified Zeiss LSM10. The only difference between the systems of Figure 5.6a and 5.6b is the inclusion of the imaging bundle; all other components are identical. The optical-sectioning performance for a front-surface mirror scanned through focus is shown in

Figure 5.7b shows the response of the system with the fiber bundle. The scale in Figures 5.7a and 5.7b is $1.2\ \mu\text{m}$ of axial mirror scan per division of the oscilloscope trace.

The optical-sectioning performance in Figure 5.7 is significantly better than in Figure 5.5. In the case of Figure 5.7b, the source and detector pinhole images were carefully imaged onto a single fiber at the proximal end of the bundle. This differs from the case of Figure 5.4b, where the Zeiss LSM10 pinhole images are scanned across the proximal face of the bundle without regard for their exact position with respect to the fibers. Objectives #2 and #3 in Figure 5.6 are $10\times / 0.25\text{NA}$ and $40\times / 0.66\text{NA}$, respectively, producing a demagnification of four times. Both objectives are infinity corrected. The geometrical images of both pinholes in this case are approximately $0.85\ \mu\text{m}$ in diameter ($3.4\ \mu\text{m}$ core diameter fibers demagnified four times). This yields normalized pinhole radii (both source and detector) of $v_p \approx 3.4$ at $514\ \text{nm}$, which is somewhat better than the case of Figure 5.4b. The smaller normalized pinhole radii used in the system of Figure 5.6 more closely approximate the ideal case of $v_p = 0$, and the response to a plane mirror scanned through focus deviates less from the sinc^2 response described in chapter 2. The asymmetry of the curves in Figure 5.7 is typical of spherical aberration. This is due to the omission of microscope cover slips which are required for the $10\times$ and $40\times$ objectives. The oscillations present in Figure 5.7b are due to noise. This noise is visible in Figure 5.7b, but not in Figure 5.7a, because of the signal reduction resulting from inclusion of the imaging-bundle.

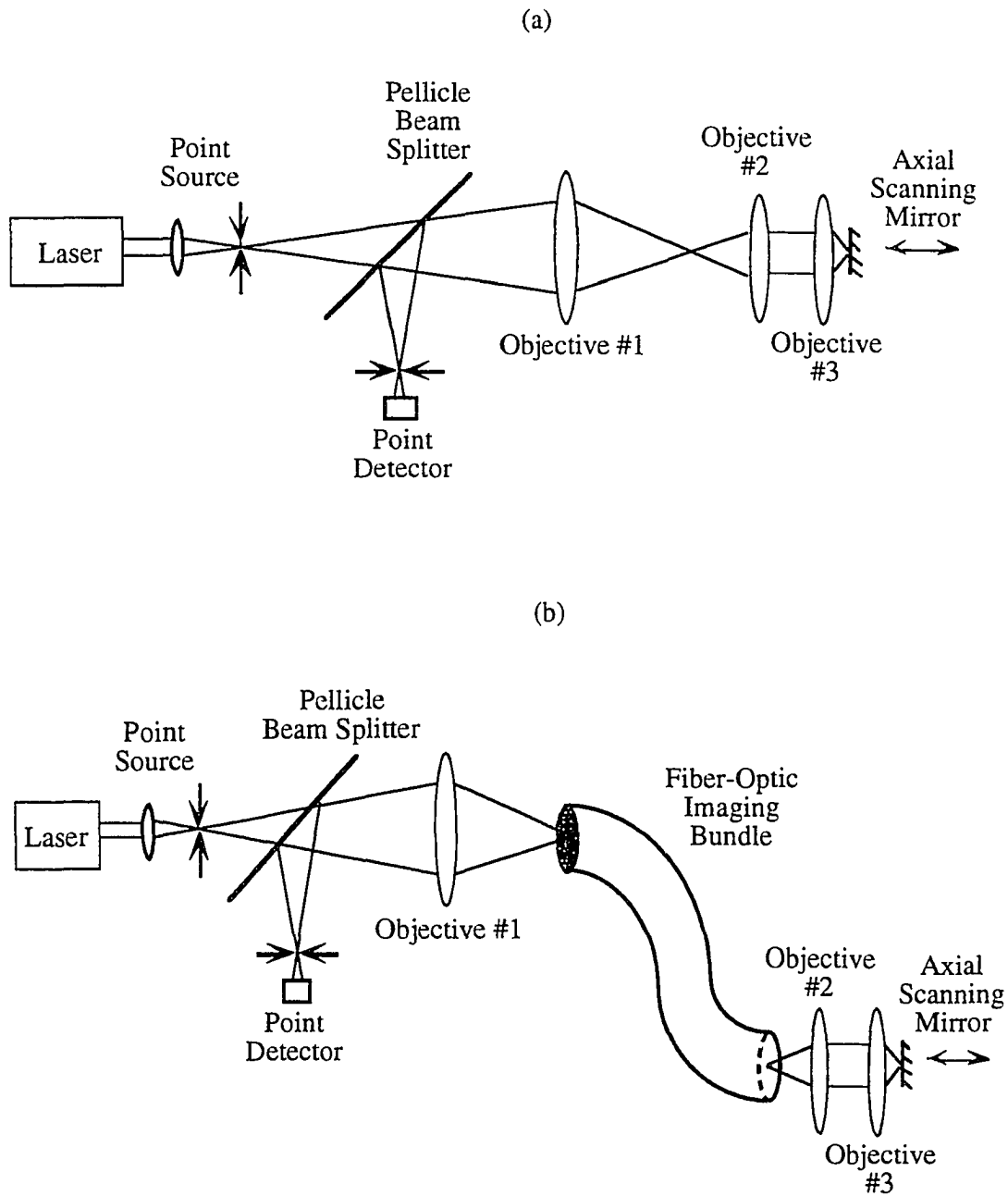
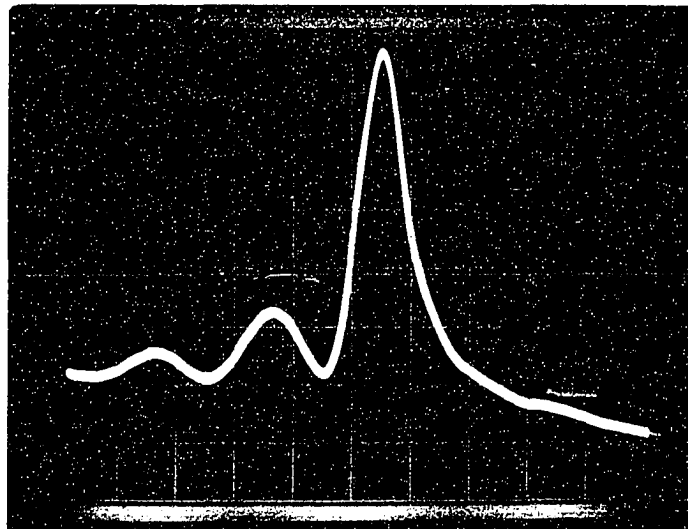


Figure 5.6. Experimental setup for comparison of the optical-sectioning performance of a confocal microscope (Fig. 5.6a) and a fiber-optic imaging-bundle confocal microscope (Fig. 5.6b). This setup allows precise alignment of the pinhole images onto the bundle fibers.

(a)



(b)

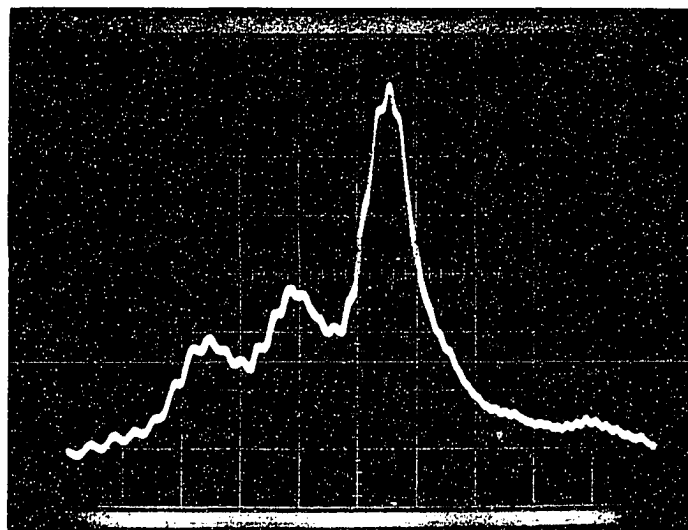


Figure 5.7. Comparison of the optical-sectioning performance of a confocal microscope with (Fig. 5.7b) and without (Fig. 5.7a) a fiber-optic imaging bundle. The experimental setup for this test is shown in Figure 5.6. The scale in Figures 5.7a and 5.7b is $1.2\text{ }\mu\text{m}$ of axial mirror scan per division of the oscilloscope trace.

Fluorescence-mode axial resolution

The axial resolution of the modified Zeiss system was also measured in fluorescence mode. It is difficult to implement a "planar" fluorescent object of negligible thickness. We have instead measured the step response of the system to a semi-infinite fluorescent object scanned through focus, and differentiated the result to obtain the fluorescence-mode optical-sectioning performance. The semi-infinite test object is shown in Figure 5.8.

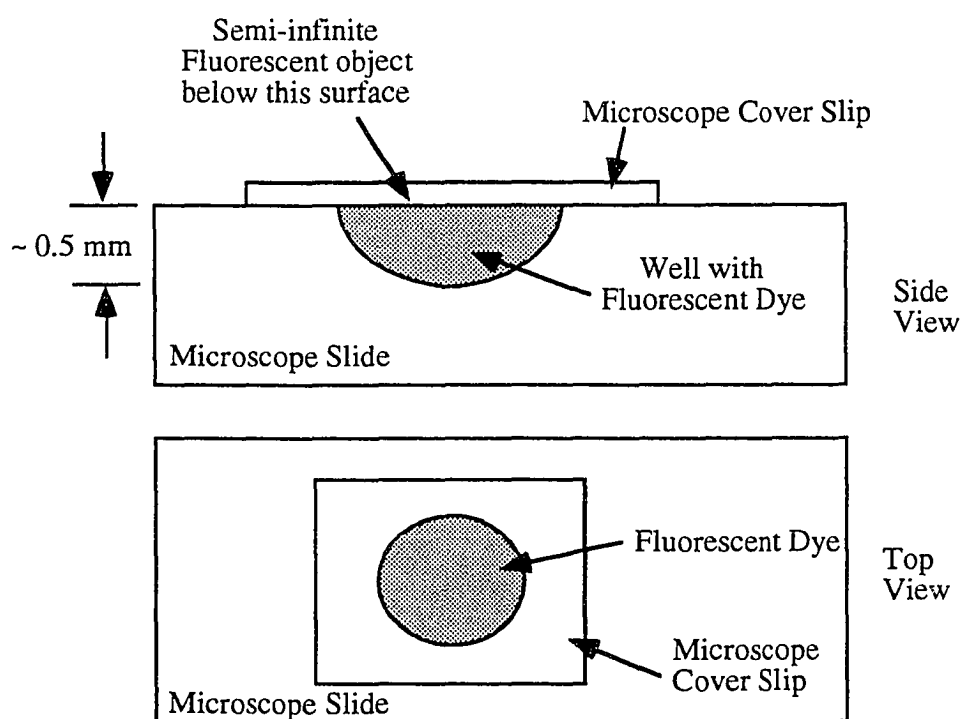


Figure 5.8. Semi-infinite fluorescent sample for evaluation of the fluorescence-mode optical-sectioning performance of a confocal microscope.

The step response of the Zeiss LSM10 to the test object of Figure 5.8 is shown in Figure 5.9 (xz scans). The response of the Zeiss LSM10 alone is shown in Figure 5.9a, while the response of the system with the imaging bundle is shown in Figure 5.9b. Argon laser illumination at 514 nm and a 63x / 1.4 NA oil immersion objective were used to obtain the response of the Zeiss microscope. In the modified system, 10x / 0.3 NA objectives were used to couple light into and out of the bundle. A 63x / 1.4 NA objective was used as the final objective to maintain the same magnification as without the bundle.

The images of Figure 5.9 are noisy. It is necessary to average over a range of lateral and axial positions in order to get reasonable results from the differentiation of these images. This was implemented with a smoothing filter that is 80 μm in the lateral (x) direction by 2 μm in the axial (z) direction. Axial averaging with a 2 μm window increases the width of the measured optical-sectioning curve, but does not prevent comparison of the system response with and without the bundle. Lateral averaging results in an average sectioning performance over the bundle that includes both core and cladding regions. The 80 μm window averages over approximately 12% of the lateral field visible in Figure 5.9a and over approximately 20% of the bundle diameter in Figure 5.9b. The resulting averaged step responses were then differentiated to obtain the optical-sectioning performance.

(a)

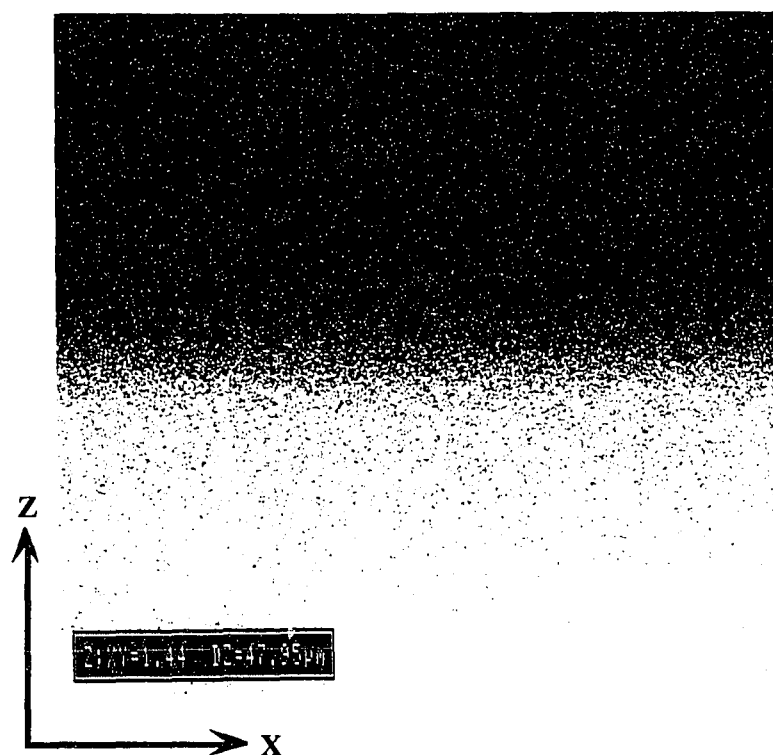


Figure 5.9. Fluorescence-mode axial step response of the Zeiss LSM10 confocal microscope. The semi-infinite object of figure 5.8 is scanned through focus. Figure 5.9a shows the performance of the commercial microscope. Figure 5.9b shows the performance of the system when modified to include a fiber-optic imaging bundle. (*xz* scans). The bright line on the right side of Figure 5.9b is specular reflection from the proximal end of the fiber bundle, outside the image region. (Continued on following page).

(b)

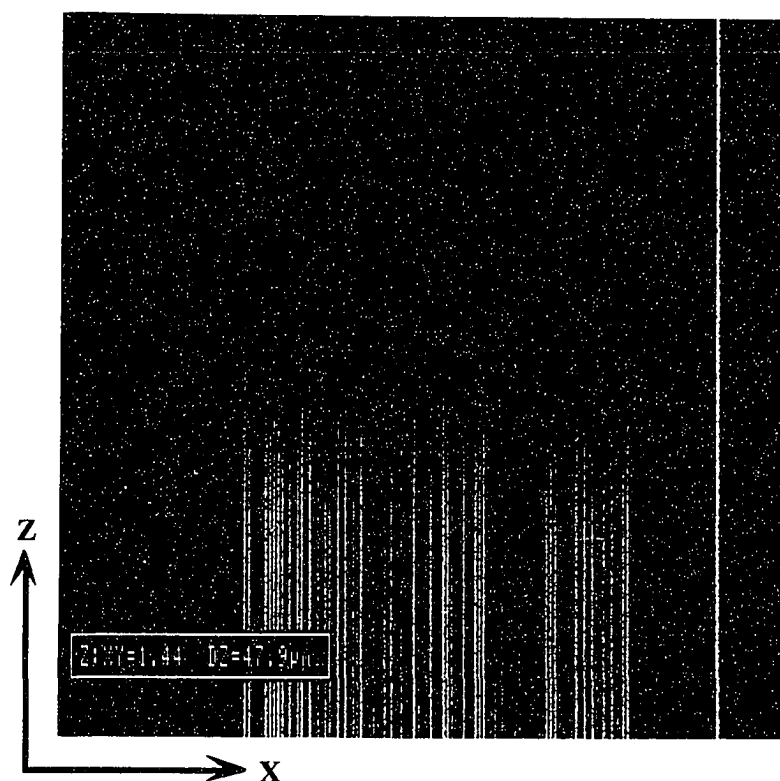


Figure 5.9. (continued).

Figure 5.10 shows the fluorescence-mode optical-sectioning performance of the Zeiss LSM10 with (dashed line) and without (solid line) the imaging bundle. The full width at half maximum (FWHM) of these curves is approximately $6\text{ }\mu\text{m}$ and $4\text{ }\mu\text{m}$ with and without the bundle, respectively. It is not known why the signal in the imaging-bundle

system (dashed curve) does not return to its original level on the right side of the trace. The sample plane in this case is below the surface of the fluorescent object, implying inadequate rejection of out-of-focus light from the upper portions of the fluorescent object.

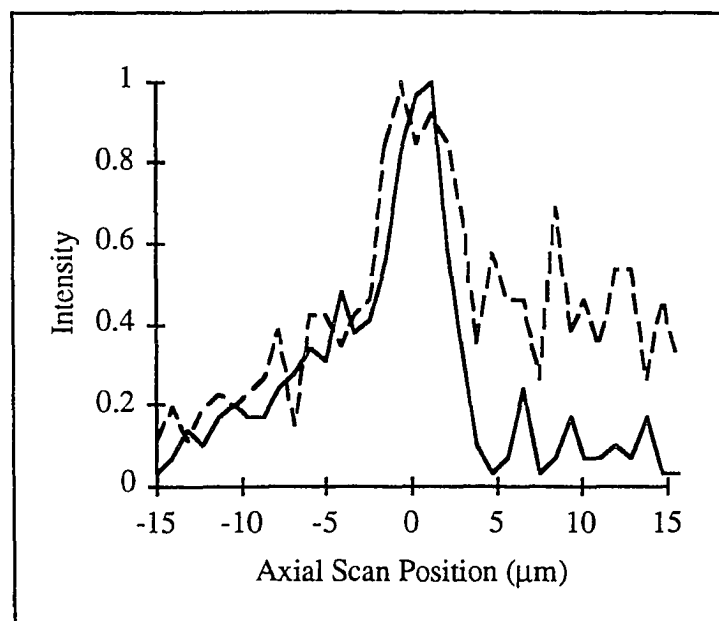


Figure 5.10. Average fluorescence-mode optical-sectioning performance over a region of the step response of Figure 5.9. The step response is averaged for a lateral (x) range of approximately 12% of the field visible in Figure 5.9a and 20% of the bundle diameter in Figure 5.9b. This step response is then differentiated to obtain the sectioning performance shown here. Comparison of system with (dashed line) and without (solid line) the fiber-optic imaging bundle.

Two sets of through-focus images of insulinoma cells (cancerous insulin cells) are shown in Figures 5.11 (Zeiss LSM10) and 5.12 (LSM10 equipped with imaging bundle) to further demonstrate the fluorescence-mode performance of the fiber-optic imaging-bundle confocal microscope. Figures 5.11 and 5.12 are images of different

cells in a single sample. The insulin granules in these cells have been tagged with fluorescent dye, while the nuclei they surround are untagged. These cells are fixed, stained, and mounted on microscope slides. The horizontal scale shown in the lower right corner of each set of images applies to all the images within the figure. The images are axially separated by $1.0\text{ }\mu\text{m}$, yielding a scan range of $8\text{ }\mu\text{m}$ between images (a) and (i) in each case. To obtain clear images through the bundle, it was necessary to average eight times for Figure 5.12. The Zeiss LSM10 scans the field-of-view in a raster pattern, and can scan each line several times before moving on to the next line. No averaging was necessary in the unmodified system (Figure 5.11). The restricted field-of-view due to the imaging bundle is seen in Figure 5.12.

The optical-sectioning ability of the confocal microscope can be seen in both cases, where the sample passes through focus in an axial scan range of approximately $6\text{ }\mu\text{m}$. The fluorescent tagged insulin granules are easily distinguishable from the nuclei. Additionally, it is possible to distinguish some granules as being above or below other granules based on when they come into focus. This is seen by comparing images (c) and (f) in both Figures 5.11 and 5.12. There are granules in Figure 5.11c that have disappeared by Figure 5.11f, indicating that they are located in the lower portion of the sample (scanning in these figures is from the bottom of the sample to the top). Equivalently, there are granules appearing in Figure 5.12f that have not yet appeared in Figure 5.12c, again demonstrating the quality of the optical-sectioning available through the imaging bundle.

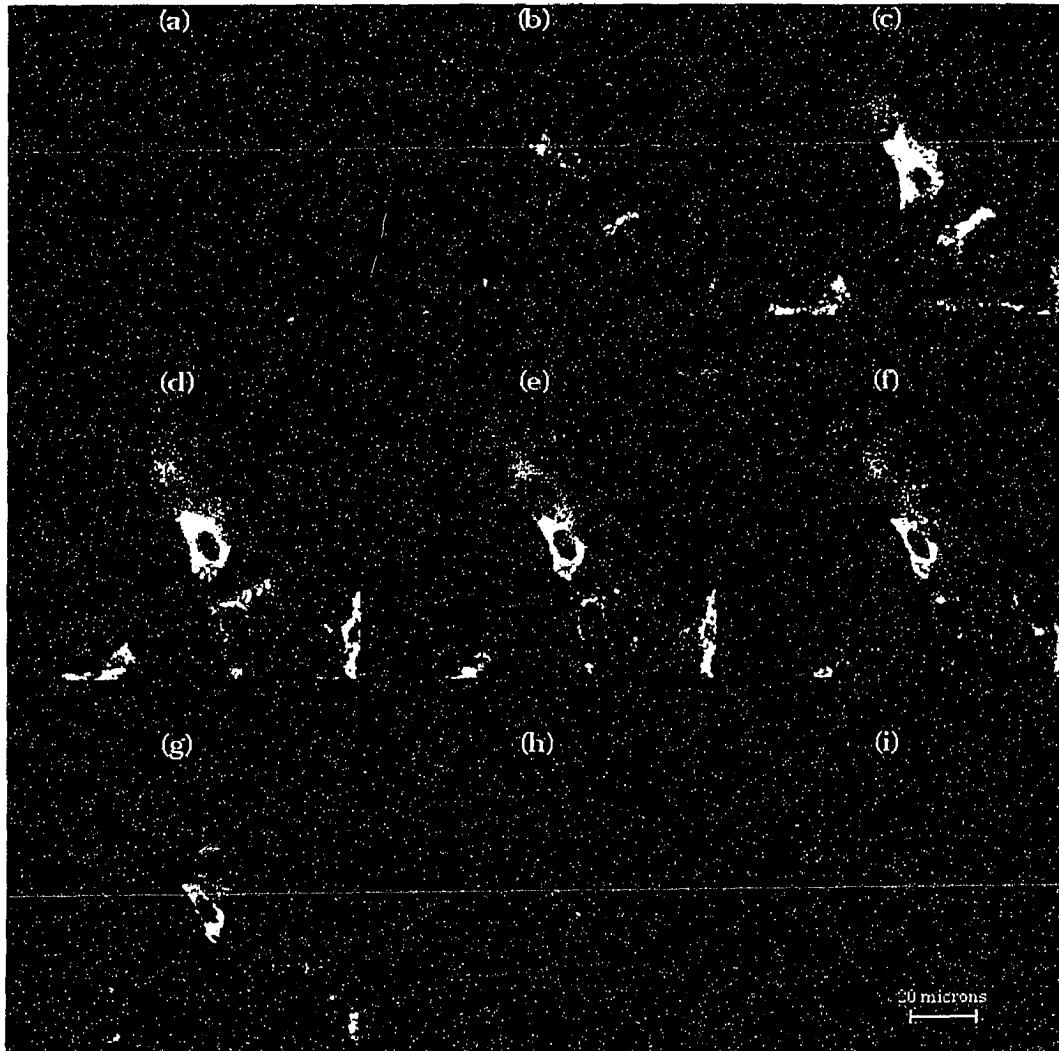


Figure 5.11. Set of through-focus images of insulinoma cells collected with the Zeiss LSM10 confocal microscope. The insulin granules have been tagged with fluorescent dye while the nuclei they surround are untagged. The axial spacing between images is $1\text{ }\mu\text{m}$. The horizontal scale in image (i) applies to all the images in the series.

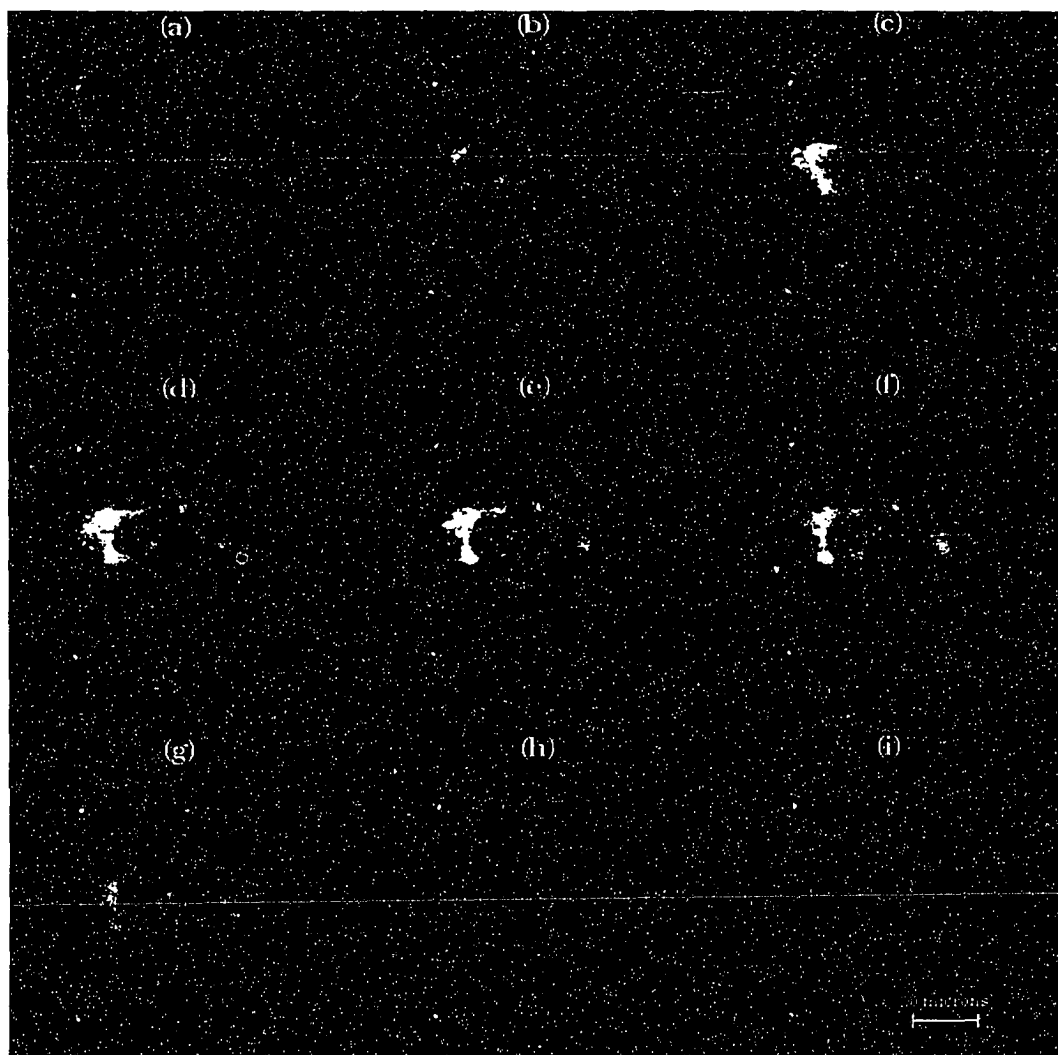


Figure 5.12. Set of through-focus images of insulinoma cells collected with the fiber-optic imaging-bundle confocal microscope. The insulin granules have been tagged with fluorescent dye while the nuclei they surround are untagged. The axial spacing between images is $1\ \mu\text{m}$. The horizontal scale in image (i) applies to all the images in the series, and is the same as the scale of the images in Figure 5.12.

Lateral resolution

There are a number of theories describing the lateral resolution of imaging bundles. These were discussed in some detail in chapter 4. The theories can be divided roughly into those that calculate a bundle modulation-transfer-function based on an average line-spread-function and those that describe the lateral resolution in terms of the sampling frequency of the fibers.

The line-spread-function is equal to a projection of the point-spread-function. In rotationally symmetric systems, a single line-spread-function fully describes the system. Fiber-optic imaging bundles are highly space-variant imaging devices, and it is not clear how accurately the average line-spread-function will predict the imaging of a pinhole by the bundle. For this reason, we use the more straightforward technique of describing the bundle lateral resolution in terms of the fiber spacing. Siegmund suggested a maximum resolvable spatial frequency of $1/3d$ to $1/2d$, where d is the fiber spacing in the bundle.^{37,67,76}

Space variance

The fiber-optic imaging-bundle confocal microscope is a space-variant imaging system. Some points on the object will be essentially undetectable if they are imaged onto a cladding region of the bundle between the cores. This is seen in Figure 5.13, which shows an image of a 15 micron diameter fluorescent sphere. Figure 5.13a shows the sphere as imaged with the Zeiss LSM10 confocal microscope. Figure 5.13b shows a similar sphere imaged through the imaging bundle with the modified Zeiss

microscope. The object is readily seen in both cases. However, several deficiencies appear due to inclusion of the imaging bundle.

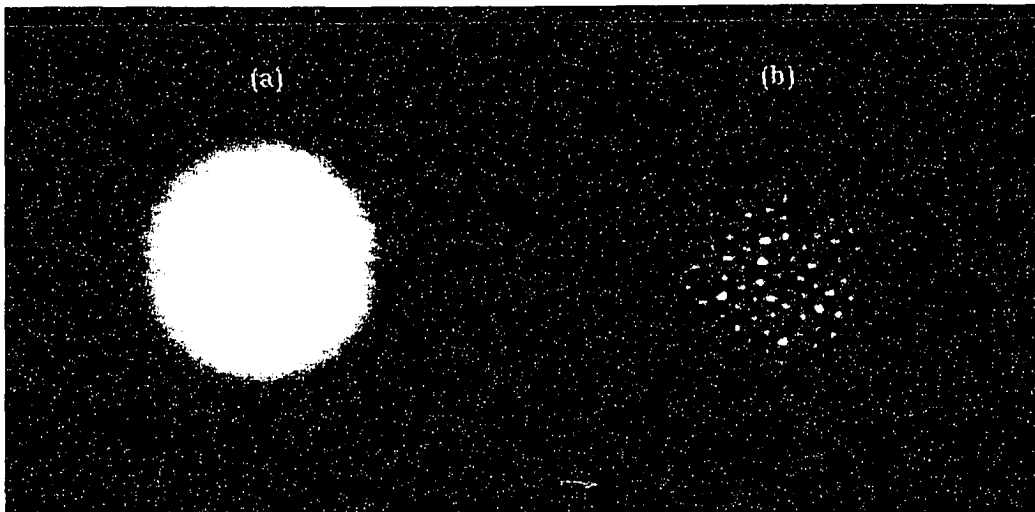


Figure 5.13. Images of a 15 μm diameter fluorescent microsphere obtained with the Zeiss LSM10 confocal microscope with (b) and without (a) the fiber-optic imaging bundle.

The visibility of the fiber elements in Fig. 5.13b indicates that the imaging properties of the system are space-variant. The system will be relatively insensitive to object points that fall in the bundle cladding. The spatial variation due to the pattern of fiber elements is distracting and is a disadvantage of the fiber-bundle system. This problem can be minimized by enlarging the pinhole images projected onto the bundle, but results in a loss of optical-sectioning performance and lateral resolution, as described above.

Three-dimensional plots of the microsphere images (Figure 5.14) show significant fiber-to-fiber variation in sensitivity in the imaging-bundle system. In the image obtained with the unmodified microscope (Figure 5.14a), the fluorescent sphere appears to have approximately uniform intensity in the center. In the image obtained through the imaging bundle (Figure 5.14b), there are significant variations at the center of the sphere.

The fibers all have comparable radiometric efficiency. Figure 5.15 shows a transmission image of several fibers in the same type of bundle (Sumitomo IGN-05/10). The fibers were evenly illuminated and overfilled with a white light source and 0.5 NA condenser. The transmitted intensity is reasonably uniform across the fibers in this figure.

The intensity variations observed in Figures 5.13b and 5.14b are due to variations in the coupling efficiency of the pinhole images to the fibers as the pinhole images are scanned across the face of the bundle. The images in Figure 5.13 were collected with a 10x / 0.3 NA objective coupling light into the bundle. The diameter of the source pinhole image on the proximal bundle face is on the order of 2.2 microns, approximately two-thirds the diameter of the fiber cores. As this focused beam is scanned across the proximal face of the bundle, the output from the distal end of the bundle varies significantly. This indicates that the coupling of the source to the fibers varies considerably. This is less of a problem with coupling of the collected light through the detector aperture, as the image of the detector pinhole is slightly larger than a single fiber.

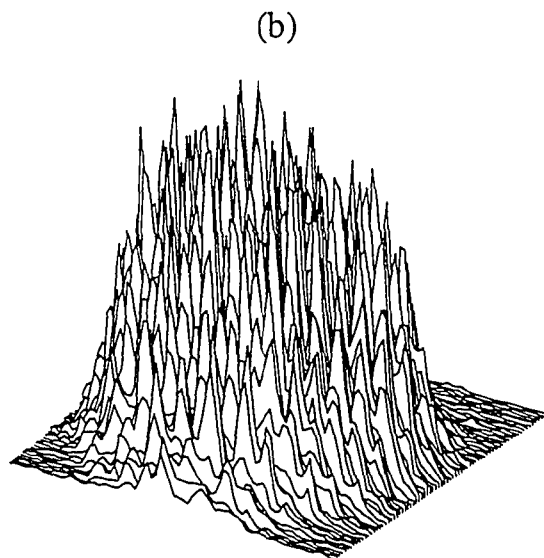
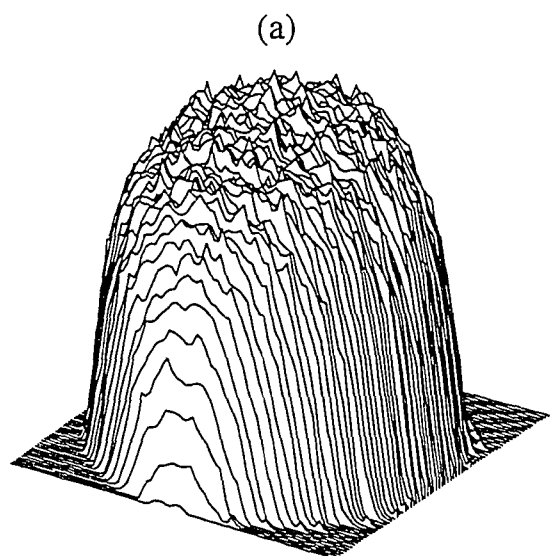


Figure 5.14. Intensity plots of the fluorescent microsphere images of Figure 5.13. Figure 5.14a is obtained with the unmodified Zeiss LSM10 confocal microscope. Figure 5.14b is obtained with the modified system of Figure 5.2.

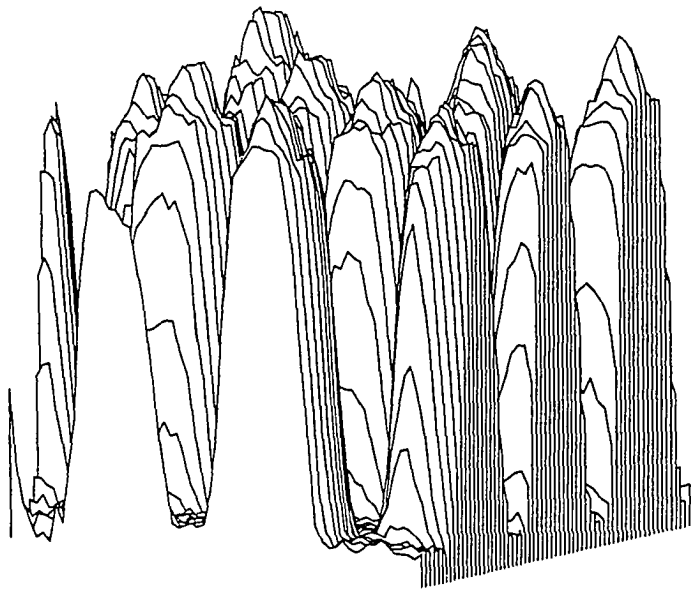


Figure 5.15. Intensity plot of light transmitted through an overfilled imaging bundle (Sumitomo IGN-05/10) for comparison with Figure 5.14b.

Radiometry

Inclusion of an imaging bundle in the confocal microscope significantly impacts the radiometric performance of the system. This includes coupling losses into and out of the bundle, as well as transmission losses. Reflections from the additional surfaces, particularly the bundle faces, increase the background noise level above that of the conventional confocal microscope.

Figure 5.16a shows the effect of the reduced radiometric performance on the signal-to-noise ratio (SNR) in images obtained with the imaging-bundle system. The image shows insulinoma cells again, where the insulin granules have been tagged with fluorescent dye. This image was collected using the same conditions as Figure 5.11, except for inclusion of the imaging bundle and distal lens. No signal averaging was performed during the collection of the images in Figures 5.11 or 5.16a. The poor signal-to-noise ratio seen in Figure 5.16a makes it difficult to see the nuclei or the fluorescent granules. Figure 5.16b shows an image obtained by line averaging during the collection of images. In this case, each line is averaged eight times. As expected, the resulting image has an improved signal-to-noise ratio. An additional advantage of averaging is that the fiber structure seen in Figure 5.13b is smeared out by of the slight mechanical jitter between successive line scans, making the imaging more space-invariant. Figures 5.16a and 5.16b show different cells within a single sample.

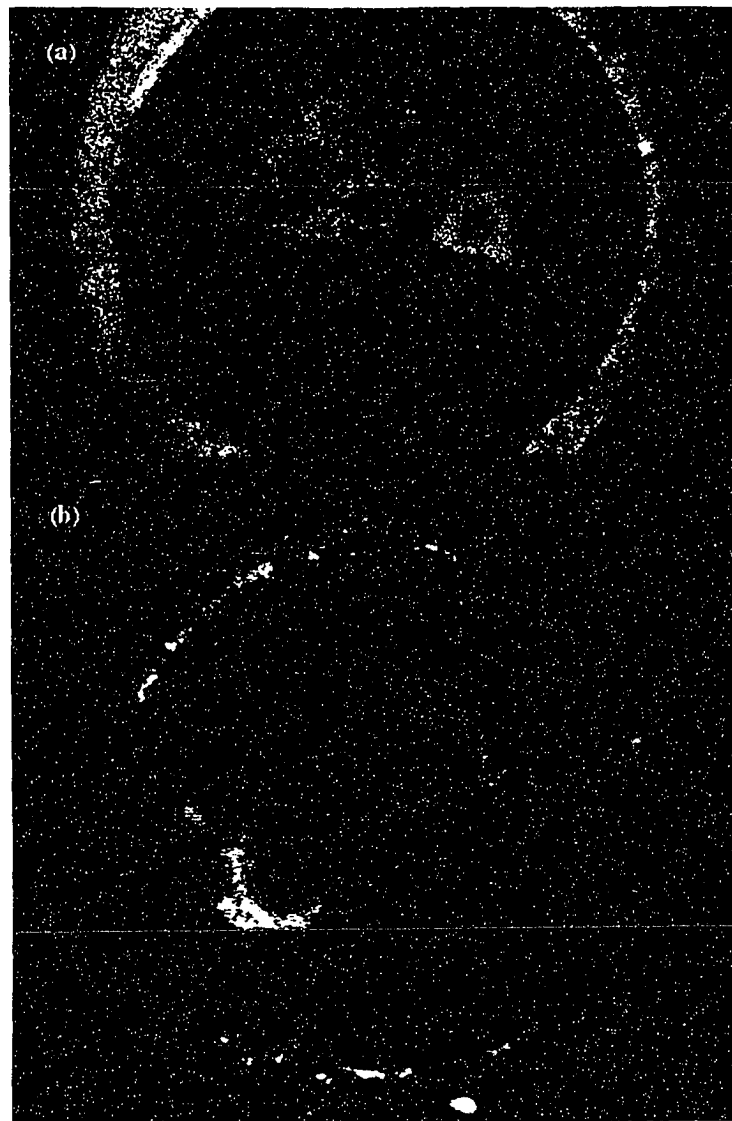


Figure 5.16. Low signal-to-noise ratio image collected with the fiber-optic imaging-bundle confocal microscope (a) and improved signal-to-noise ratio image obtained through line averaging (b). Figures 5.16a and 5.16b show different cells within a single sample.

Losses

The major loss mechanism in the fiber-optic imaging-bundle confocal microscope is coupling of light into the imaging-bundle. Losses in coupling light out of the bundle are minimal (Fresnel reflections from the end face).

At a wavelength of 488 nm, transmission of the scanned source pinhole image through the Sumitomo IGN-05/10 bundle was found to be approximately 20% (including coupling and transmission losses). This measurement was made by scanning the focused illumination beam across a region in the center of the bundle face containing several thousand fibers. The scan pattern is unrelated to the fiber positions, and the focused spot is imaged onto many positions in the cores and cladding during its scan range. This measurement, therefore, reflects the average coupling and transmission losses for a 0.3 NA input beam.

Transmission losses are minimal (< 0.2 dB/m) in the visible spectrum for silica imaging bundles (see chapter 4), and will generally be much less significant than coupling losses. Soft glass and plastic bundles exhibit somewhat higher transmission losses, but are not good candidates for use in the fiber-optic imaging-bundle confocal microscope due primarily to inadequate resolution. Bending losses are of minimal importance in silica bundles due to the relative stiffness of these bundles (they break before substantial loss occurs).

Losses in the distal imaging lens (L2 in Figure 5.2) have also been significant when implemented with a pair of microscope objectives. This can be improved with a lens

designed specifically for this system. The transmission of the microscope objectives used to implement lens L2 was measured. The 10x / 0.3 NA objective facing the bundle has a transmission of approximately 70%. The 63x /1.4 NA objective facing the sample has a transmission in the illumination path of approximately 30%, which includes loss due to vignetting. The 63x objective is designed to collect light from its front focal plane, not focus a beam entering the objective through the rear. When used to focus light collimated by the 10x objective, the entrance pupil of the 63x objective is too small to capture the entire beam. An estimate of the effect of this vignetting is

$$T_{vignetting} = \begin{cases} \left(\frac{NA_{final}}{(M_{distal})(NA_{beam})} \right)^2 & ; \quad NA_{final} \leq (M_{distal})(NA_{beam}) \\ 1 & ; \quad NA_{final} > (M_{distal})(NA_{beam}) \end{cases} \quad (5.3)$$

where M_{distal} is the magnification of the distal lens, NA_{distal} is the numerical aperture of the final objective, and NA_{beam} is the numerical aperture of the light exiting the bundle or the numerical aperture of the 10x objective facing the bundle, whichever is smaller. The vignetting loss for the 10x / 63x combination is on the order of 50%. Therefore, the transmission of this objective when collecting light should be on the order of 60% (with no vignetting).

This calculation will overestimate the vignetting loss. As seen in Figure 5.8, the coupling efficiency into the fibers of the bundle decreases with incidence angle. The beam exiting the fiber has the greatest intensity at shallow angles, and the lowest intensity at steep angles. The outer portion of the collimated beam is truncated by the

63x objective. The actual loss is, therefore, somewhat overestimated by equation (5.3), which assumes a uniform beam.

The total loss due to the imaging bundle and lens L2 in the current implementation of this system can be calculated by combining the two losses. The transmission of the bundle and distal lens in illumination is

$$\begin{aligned} T_{illun} &= (T_{bundle})(T_{10x})(T_{63x})(T_{vignetting}) \\ &= (0.2)(0.7)(0.6)(0.5) \\ &= 0.04 \end{aligned} \quad (5.4)$$

The transmission of the distal lens and bundle in detection is

$$\begin{aligned} T_{det} &= (T_{bundle})(T_{10x})(T_{63x}) \\ &= (0.2)(0.7)(0.6) \\ &= 0.08 \end{aligned} \quad (5.5)$$

This results in approximately 96% and 92% loss in the illumination and collection directions, respectively. The combined loss due to inclusion of the imaging bundle and distal lens is on the order of 99.5%.

Background noise

Background noise in the fiber-optic imaging-bundle confocal microscope is greater than in the conventional confocal microscope due to the inclusion of additional elements that increase the amount of scattered and reflected light. This is less of a problem in the fluorescence mode, where a dichroic beamsplitter and/or a long-wave pass filter are used to eliminate the illumination wavelengths from the detected signal.

Fresnel reflections at the entrance and exit faces of the fiber bundle are a significant issue in the fiber-optic imaging-bundle confocal microscope. The faces of the bundle are at intermediate image planes in the system, so reflections from these surfaces are in-focus at the detector aperture. In the brightfield mode, a 4% reflection from the proximal bundle face can be an order of magnitude stronger than the signal from even the brightest objects (whose signal is diminished significantly by losses in the system).

There are several ways to reduce reflections from the bundle faces. A microscope cover slip can be cemented onto the ends of the fiber bundle. This moves the Fresnel reflections to another plane (approximately 0.17 mm away from the bundle face for a #1.5 cover slip). While the total reflection is unchanged, it is no longer in focus at the detector aperture and therefore contributes less background signal. It is also possible to cement lenses (e.g. gradient index lenses) to the face of the fiber bundle to reduce the Fresnel reflections.

The cover slip or lens must be glued carefully to the fiber bundle to avoid the effect shown in Figure 5.17. This is an image of cancer cells (round objects) and fibroblasts (elongated objects). The cancer cells have been labeled with the fluorescent dye FITC, while both the cancer cells and the fibroblasts are labeled with the fluorescent dye Texas Red. Figures 5.17a and 5.17c were obtained with argon laser illumination at 514 nm; Figures 5.17b and 5.17d were obtained with argon laser illumination at 488 nm. The sample was imaged with the Zeiss LSM10 confocal microscope with (Figs. 5.17c and 5.17d) and without (Figs. 5.17a and 5.17b) the fiber-optic imaging-bundle.

The right side of the image in Figure 5.17c (514 nm illumination) has a bright crescent. The crescent is much less apparent in Figure 5.17d (488 nm illumination). It is likely that a small gap remains in this region between the face of the fiber bundle and the cover slip. The reflections due to this error are highly wavelength sensitive, and are probably due to multiple reflections (a Fizeau fringe). The microscope was operated in the fluorescence mode to collect these images, and the reflection from the bundle face is so strong that the spectral filter in the detection arm is inadequate to eliminate this signal.

The bundle faces can be anti-reflection coated to reduce reflections. This has not been attempted, although it is a viable solution. It is also possible to use oil immersion lenses to couple the light into and out-of the bundle with lower Fresnel reflections.

Distal objective lens

The distal objective lens is an important issue in the fiber-optic imaging-bundle confocal microscope. The most difficult system to build will be for applications where the lens diameter is restricted to the diameter of the fiber bundle. This is achievable in conventional endoscopy with gradient-index lenses, and is desirable to give access to the maximum number of sample locations (e.g. via a catheter in in-vivo medical applications).

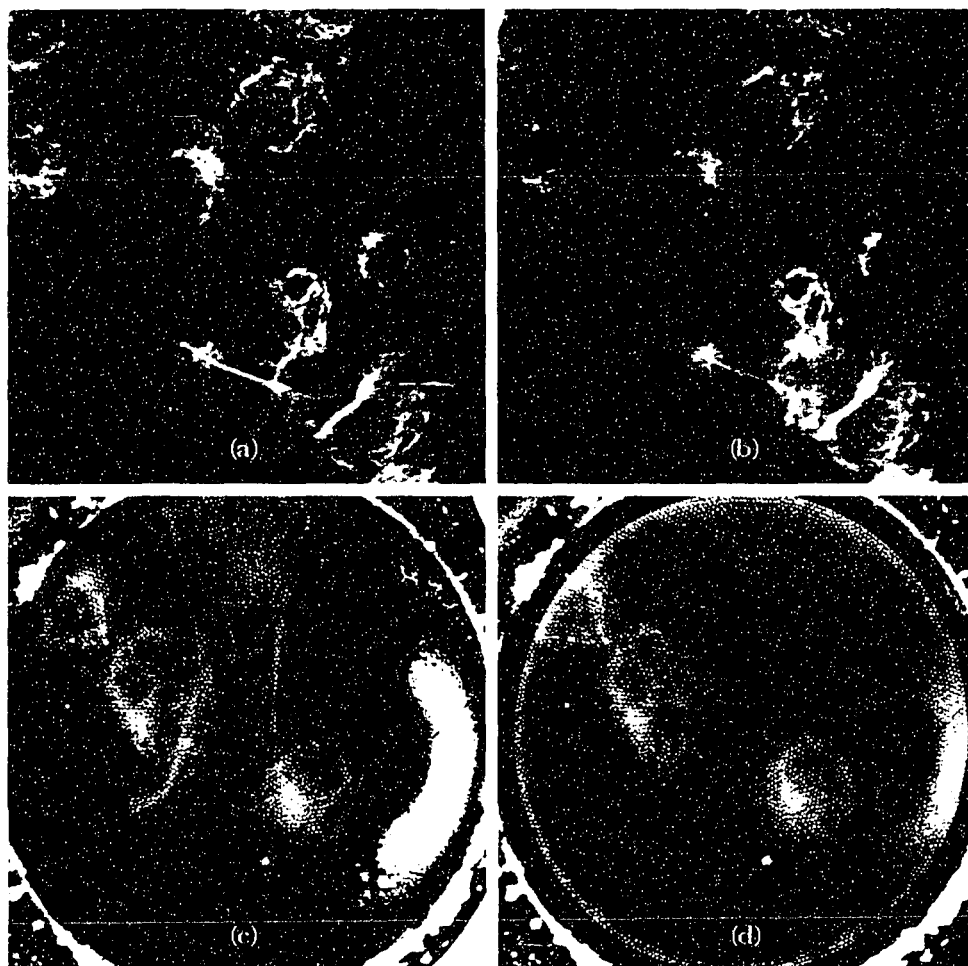


Figure 5.17. Confocal images of cancer cells (round objects) and fibroblasts (elongated objects). 5.17a and 5.17b are fluorescent images acquired with the Zeiss LSM10 with 514 and 488 nm illumination, respectively. Figs. 5.17c and 5.17d are the corresponding images collected through the fiber-optic imaging-bundle confocal microscope. The bright crescent on the right side of Fig. 5.17c is due to a poorly glued microscope cover slip.

In this section, we briefly describe some of the issues that need be addressed in the design of the distal objective lens for this system. All the experimental results presented in this dissertation were obtained with a pair of back-to-back microscope objectives serving as the distal imaging lens (L2 in Figure 5.2). This has allowed us to implement confocal microscopy through a fiber bundle, and obtain data on system performance. The next major step in this project is the miniaturization of the distal imaging lens to begin meeting realistic size constraints. A gradient-index lens design is described.

Magnification

In endoscopy, the distal objective typically images a large field onto the end of the bundle, and, therefore, the final numerical aperture of the beam (at the sample) will be smaller than at the bundle. This is accompanied by a depth-of-focus of several millimeters to tens of millimeters.⁹⁶ In the fiber-optic imaging-bundle confocal microscope, however, a high final numerical aperture (at the sample) is necessary to obtain good optical sectioning (small depth-of-focus). This will generally require a magnifying, rather than demagnifying, objective at the end of the bundle. The numerical aperture of the beam at the sample will be higher than the numerical aperture in the bundle. For example, a 4x objective will image the Sumitomo IGN-05/10 bundle onto the sample with 0.85 μm diameter images of the cores and a final NA of 1.4 (assuming the bundle is not underfilled). The minimum spot size at the sample will be approximately 1 μm in diameter, whereas it would be on the order of one-third this diameter in a high-quality 1.4 NA microscope objective.²³ The sampling interval (core spacing) in the image will be on the order of 1.1 μm .

The magnification of the distal objective will generally be limited by the beam NA in the bundle (may be less than the bundle NA due to underfilling) and the immersion medium refractive index. The maximum NA at the sample is restricted to be somewhat less than the refractive index of the immersion medium (the 63x / 1.4 NA oil-immersion objective is designed for use with oil having $n = 1.518$). The situation is even more restrictive in the case of water immersion ($n = 1.33$) or air immersion ($n = 1.0$). In-vivo medical applications may include air, water, or oil immersion. For example, a body cavity might be filled with air or saline during an examination. Alternatively, the refractive index of human skin is closely approximated by the index of oil, making this a possible design condition for dermatology systems.²⁴

It is possible to further increase the resolution of the system in exchange for reduced radiometric performance. The sampling interval at the sample is the core spacing of the bundle divided by the magnification of the distal lens. The 10x / 63x objective pair discussed above has a magnification of 6.3x, and will produce a sample spacing of $0.7 \mu\text{m}$. This is somewhat finer than obtained with a 4x lens. The illumination beam will be vignetted in this "over-magnification" case according to equation (5.3). The fiber bundle will also be underfilled by the light collected from the sample, but this will not cause light loss. Resolution cannot be increased arbitrarily with this technique. The images of the fiber cores will eventually overlap (due to the point-spread-function of the lens) to the extent that adjacent samples are not independent.

The design of lenses with high numerical apertures generally requires multiple elements, some with diameters larger than the actual field.¹⁰³ While this poses little difficulty in microscope objectives, it may be impractical for fiber bundle systems

with tight size requirements. The magnification of the distal lens in the imaging-bundle confocal microscope may therefore be limited by the size constraints.

Telecentricity

The distal objective lens for the fiber-optic imaging-bundle confocal microscope should ideally be telecentric in both object and image space (doubly telecentric). Telecentricity is necessary on the side of the objective facing the image bundle to ensure proper coupling to the fibers, as shown in Figure 5.18.³² If the objective is not telecentric on this side, then the coupling efficiency will vary across the bundle. The maximum incidence angle of the beam illuminating the fibers will increase with field angle. If the beam NA is equal to, or greater than, the fiber NA, then the coupling will decrease off-axis due to some of the beam being incident on the bundle face at angles too steep to be bound by the fibers. Furthermore, once the incident cone of light has only off-axis components, as shown in Figure 5.18b, the output from the fiber will gain a donut-like appearance.

A similar situation occurs on the proximal end of the imaging bundle, where a telecentric lens produces constant coupling across the fibers of the bundle. This is a less significant issue than the telecentricity of the distal objective due to the field angles involved. When implementing the fiber-optic imaging-bundle confocal microscope, we have used a 10x microscope objective at the proximal end of an 0.5 mm diameter imaging bundle. The focal length of this objective is approximately 16 mm, resulting in a half-angle at the edge of the field of $0.25\text{mm}/16\text{mm} = 0.016$, which is a small fraction of the steepest angle bound in the fibers of the 0.35 NA bundle.

Thus, there will be minimal coupling variation across the bundle due to the use of a non-telecentric lens on the proximal end of the bundle.

The requirement for telecentricity on the object side was described in chapter 2 for specular objects (see Figure 2.7). The majority of applications of the fiber-optic imaging-bundle confocal microscope are likely to be in fluorescence, and the telecentricity requirement on the object side may be relaxed in these cases.

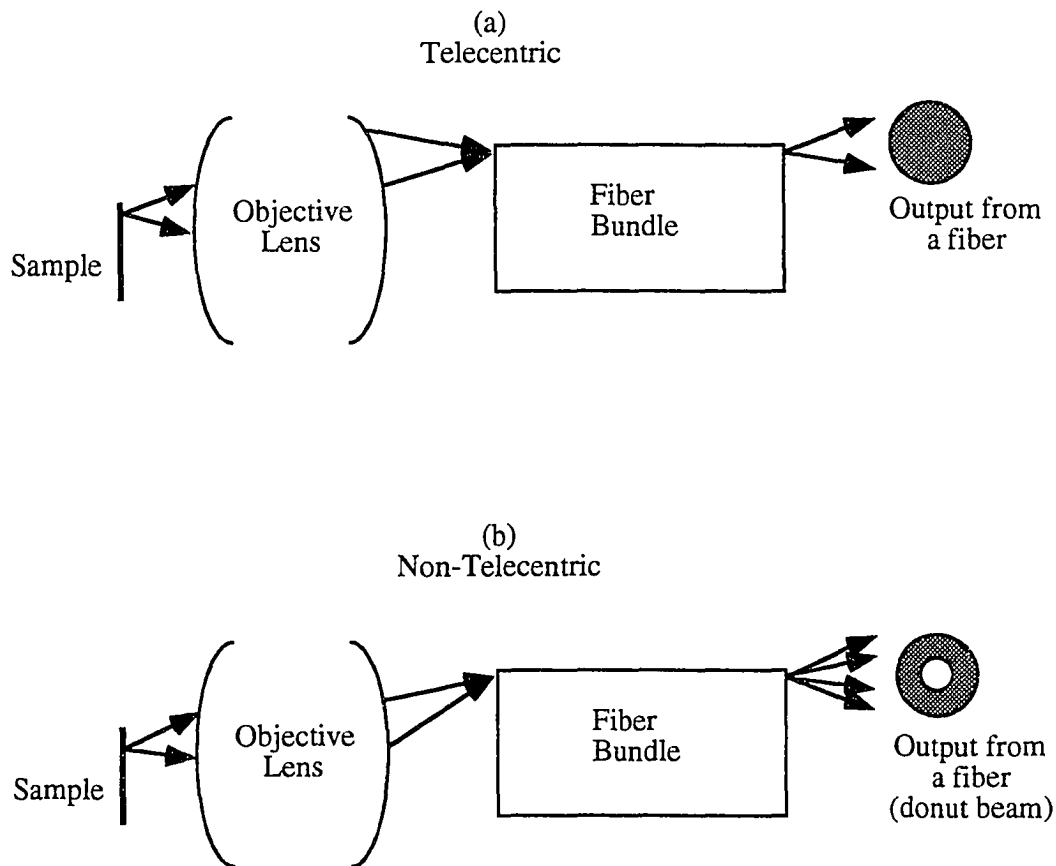


Figure 5.18. Telecentric (Fig 5.18a) and non-telecentric (Fig. 5.18b) distal imaging lenses.

Aberrations

It will be necessary to control chromatic aberration in fluorescence systems. In the presence of longitudinal chromatic aberration, the images of the source and detection pinholes (relayed by the bundle) will be in different axial positions in the sample. This will reduce both the optical-sectioning performance and the sensitivity of the system. Lateral chromatic aberration will cause misregistration of the source and detection pinhole images for off-axis object points.²³

As seen in Figure 5.17, one of the applications of confocal microscopy is the analysis of samples which have been labeled with two or more fluorescent dyes. Multiple images of the sample are collected using different illumination wavelengths. Chromatic aberration will cause misregistration of these images, reducing the accuracy of composite images.

Monochromatic aberrations in the distal lens of the fiber-optic imaging-bundle confocal microscope are likely to be of less concern than mechanical and radiometric issues. The 4x magnification distal objective-lens discussed above produces an image of the Sumitomo bundle with 0.85 μm diameter cores and 1.1 μm core spacing. There is little motivation in such a situation to design an objective whose point-spread-function is significantly smaller than the image of the core diameters. In fact, a fluorescent system might benefit from a larger point-spread-function that blurs the images of the fiber cores across a larger region of the sample. This would be useful in the study of weakly fluorescent or fragile samples where the undetected portions of the sample conjugate to the fiber clad represent lost light (see Figure 5.13b). Therefore,

the aberration correction in the distal lens of this system may be reduced in order to satisfy other requirements.

Potential designs

There are a number of possibilities for the distal imaging lens. This includes modification of conventional microscope and endoscope objective designs. Other possibilities include gradient-index, diffractive, and catadioptric lenses.

Microscope objectives may serve as logical starting points for the design of the distal imaging lens. The microscope objectives used to obtain the results in this dissertation have produced excellent images, but often with significant light loss. It may be possible to simplify these designs, potentially sacrificing field-of-view and aberration correction in order to satisfy size constraints and improve the radiometric performance.

As described above, endoscope objectives are typically designed to image a large field-of-view at low magnification. For an image bundle NA of 0.35, this might result in a sample space NA of less than 0.1. These low NA's make it unlikely that such a design can simply be "flipped around," exchanging object and image positions.

Gradient-index (GRIN) lenses are available in very small sizes. The most common type of index gradient is radial, but axial and spherical gradients are available as well.^{104,105} A preliminary examination of radial GRIN lenses available from Nippon Sheet Glass (NSG) has shown poor performance with a single, unmodified lens.

However, two modified NSG lenses working together appear to give adequate imaging performance.

A lens design employing two modified NSG lenses is shown in Figure 5.19. The lens has a magnification of 2x, object (bundle) diameter of 0.5 mm, and object space NA of 0.3. The specifications for the NSG lenses are for a wavelength of 550 nm (we were unable to obtain dispersion information for these lenses from the manufacturer at the time this lens was designed).¹⁰⁶ This lens was mistakenly designed for a wavelength of 500 nm, rather than 550 nm. With no dispersion specified for the GRIN lenses, they will perform identically at all wavelengths. The other components of the system (a microscope cover slip and an immersion medium simulating the sample) will perform somewhat differently at the two wavelengths, and the predicted performance of this design will be slightly in error.

The imaging bundle is in contact with the first surface of the lens (presumably cemented to reduce Fresnel reflections). An 0.17 mm thick microscope cover slip was included in the design to simulate a protective window at the end of the lens (facing the sample). Schott Glass type K5 was used to simulate a microscope cover slip with $n \approx 1.53$ at 500 nm.¹⁰⁷ The sample is 1.5 μm beyond the end face of the window (although it should really be somewhat further into the sample to simulate subsurface imaging - the main advantage of the confocal microscope). The sample material is Schott Glass type K5, chosen to approximate the refractive index of oil.

The two lenses used in this design are an NSG ILW-1.0 and an NSG ILH-1.0. The ILW-1.0 has a diameter of 1.0 mm, length of 2.95 ± 0.30 mm and a maximum NA of

0.46. The ILH-1.0 has a diameter of 1.0 mm, length of 2.19 ± 0.30 mm and a maximum NA of 0.6.¹⁰⁶ The end surfaces of both lenses are flat. These lenses are designed to image an object several millimeters beyond one end of the lens onto the opposite lens surface. In this design, the lenses were allowed to vary from the manufacturer's specifications according to two criteria. First, the lens can be shortened, but not lengthened. Second, a curvature can be ground on one end of each GRIN lens, with the remaining flat surface facing the bundle or sample.

In the design of Figure 5.19, the ILW-1.0 is in contact with the bundle, while the ILH-1.0 is adjacent to the sample. The ILW-1.0 has been shortened to 1.60 mm and a curvature of $R = -2.49$ mm placed on the inside surface (away from the bundle). The ILH-1.0 has been shortened to 1.68 mm and a curvature of $R = 2.03$ mm placed on the inside surface (away from the sample). The spacing between the GRIN lenses is 1.92 mm, and the total length of the lens is 5.40 mm.

The performance of this design is shown in figure 5.20. A modulation-transfer-function plot of this lens is given in Figure 5.20a, a spot diagram in Figure 5.20b, and distortion and field-curvature plots in Figure 5.20c. The modulation-transfer-function at the three field points of 0.0 mm (on-axis), 0.15 mm, and 0.25 mm (edge of bundle) stays above 0.65 for spatial frequencies below 115 lines/mm. This spatial frequency corresponds to $1/(2d)$ where d is the $4.4 \mu\text{m}$ fiber spacing of the Sumitomo IGN-05/10 imaging bundle. This spatial frequency was suggested by Siegmund as discussed above and in chapter 4 as a reasonable guideline for the maximum spatial frequency that can be transmitted by an imaging bundle.

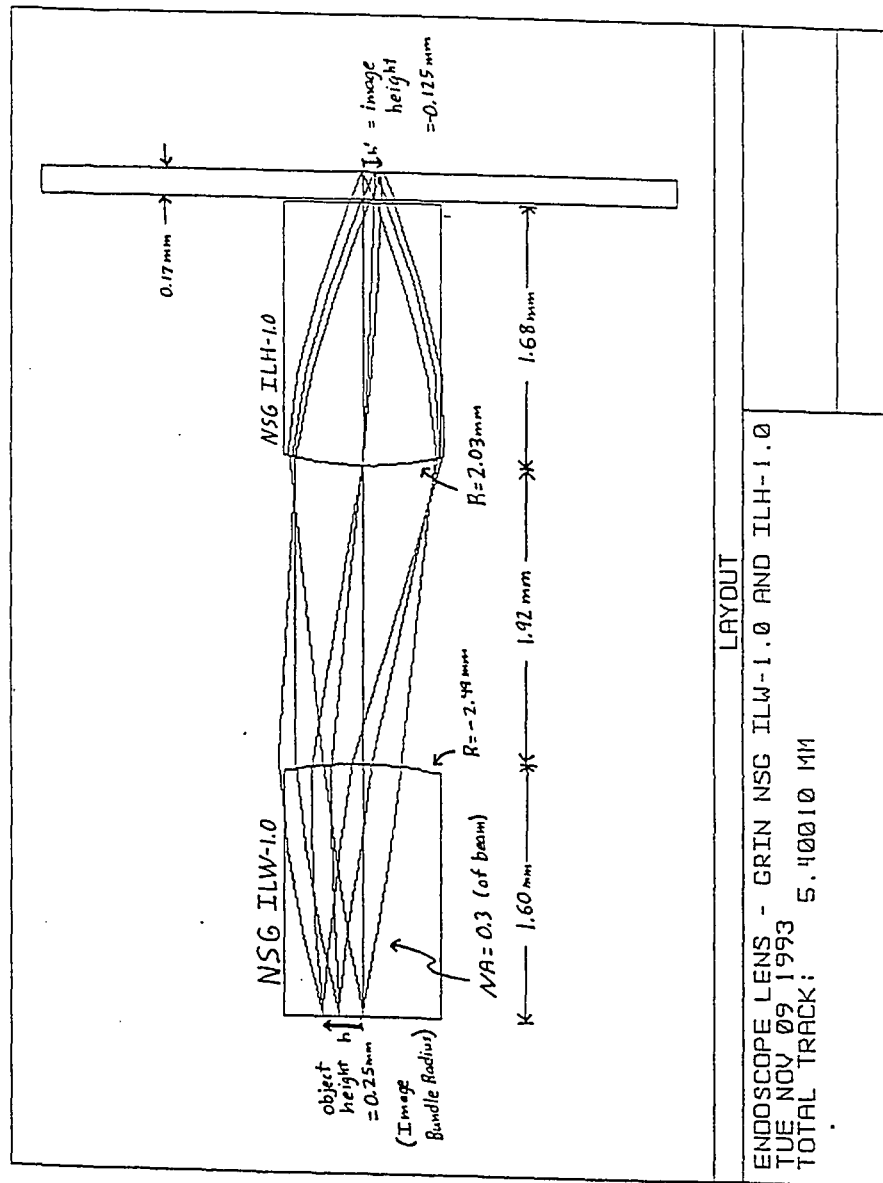
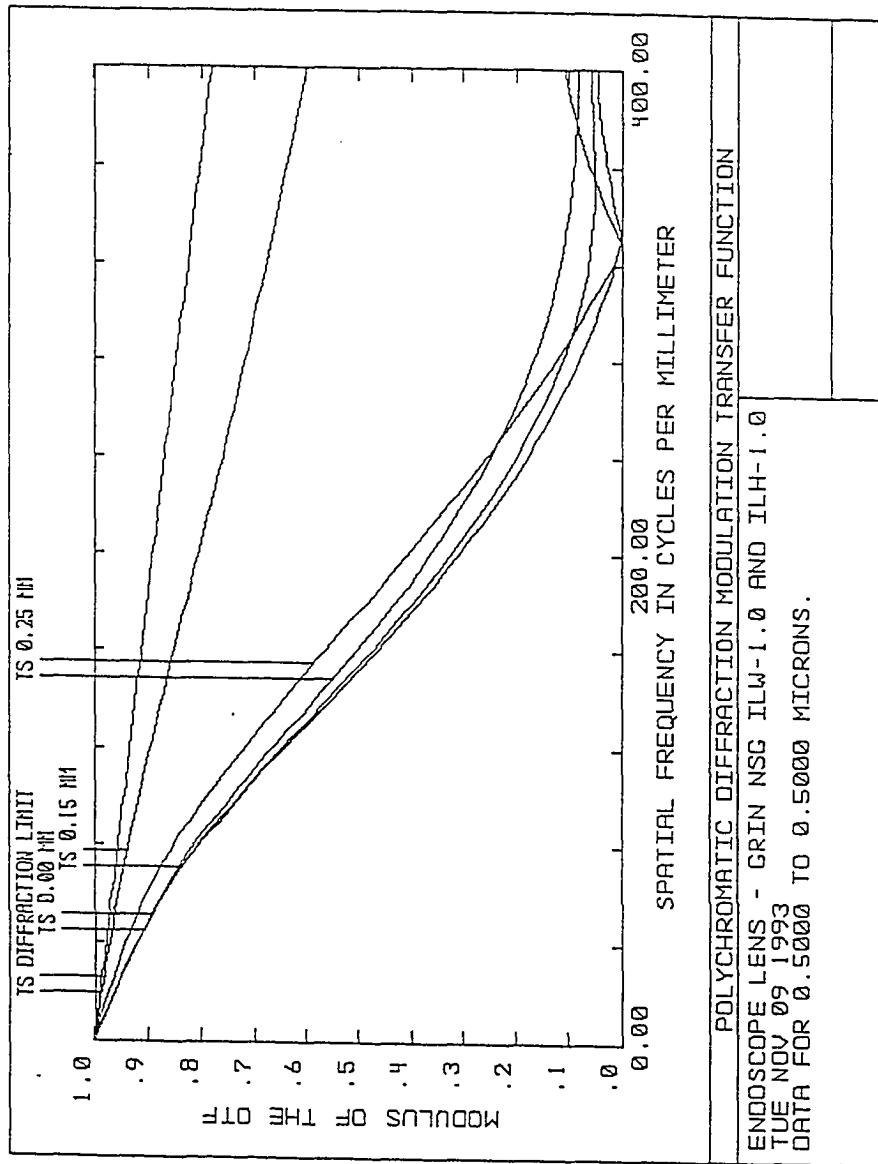


Figure 5.19. Gradient index (GRIN) lens design for the distal imaging lens of a fiber-optic imaging-bundle confocal microscope.



(a)

Figure 5.20. Performance of the GRIN lens design of Figure 5.19. Figure 5.20a is a modulation-transfer-function plot, Figure 5.20b is a through-focus spot diagram, and Figure 5.20c shows distortion and field curvature. (Continued on the following pages).

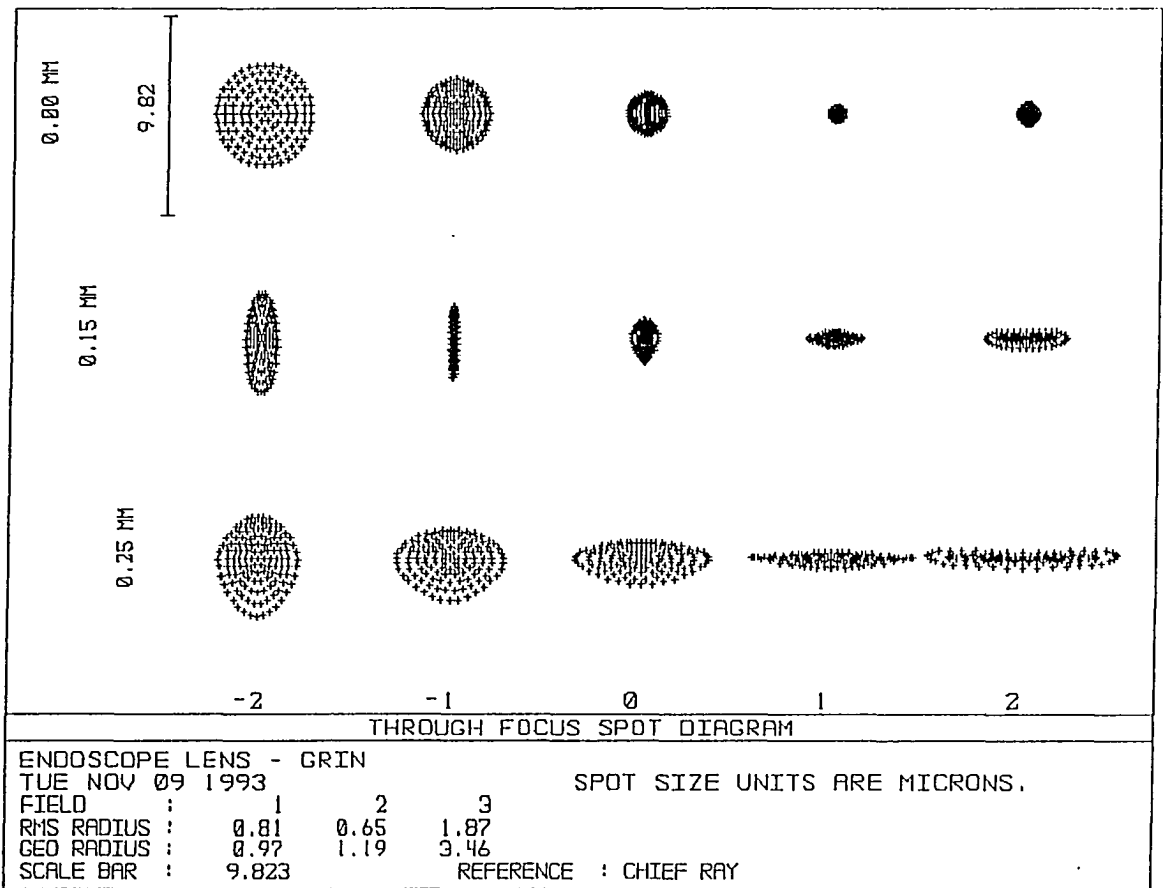


Figure 5.20. (Continued).

(b)

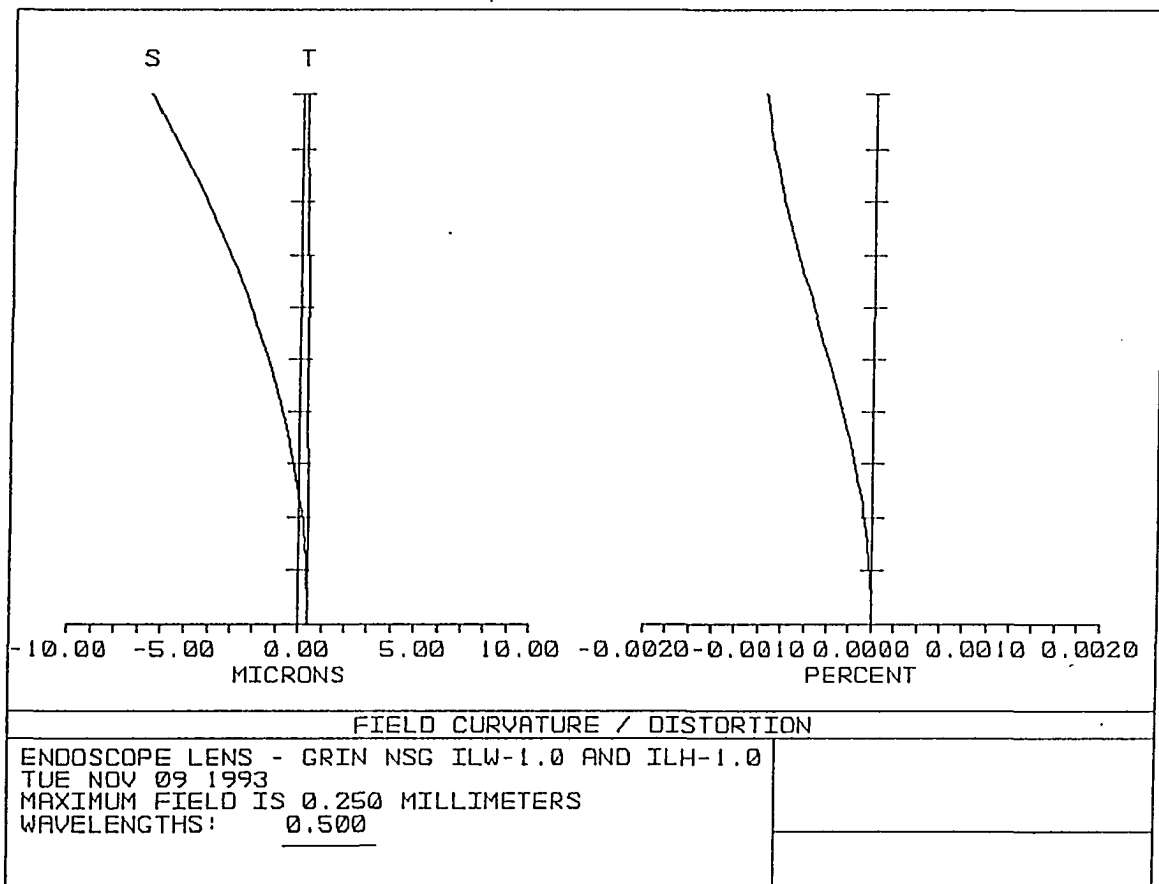


Figure 5.20. (Continued).

(c)

This lens has been designed for a single wavelength. This is appropriate for reflection (brightfield) confocal microscopy. The design may need to be revised for use in fluorescence systems. For example, FITC and Texas Red fluorescent dyes were used to label the sample of Figure 5.17. The absorption and emission peaks of FITC are 492 nm and 520 nm, respectively. The absorption and emission peaks of Texas Red are 596 nm and 620 nm, respectively.¹⁰⁸ The requirements for color correction will vary with application. For an application using a single fluorescent dye, color correction over a range less than 50 nm may be adequate (the absorption and emission spectra of the dyes cover finite wavelength ranges).

Stabilizing and focusing mechanism

A significant challenge in the implementation of confocal microscopy through an imaging bundle is the mechanism for stabilizing and focusing the distal end of the bundle onto the desired sample plane. Confocal microscopy achieves the maximum optical-sectioning effect with high NA beams. In general, this requires a magnifying objective at the distal bundle end with a power on the order of 2x - 4x. Image blurring due to sample motion will be exacerbated by this magnification.

A preliminary focusing-mechanism design is shown in Figure 5.21. The bundle and distal lens system is held in place by simply pressing it against the sample. A fine thread (e.g. 100 threads per inch) is used for coarse focusing of the bundle. A thread of 100 threads per inch yields approximately 1 μm of axial motion per 1.4 degrees of turn. A tube piezoelectric device is used to precisely focus the object plane within the sample. The mechanism shown here may not be adequate for all applications; however, it is a reasonable initial step in miniaturization of the distal objective.

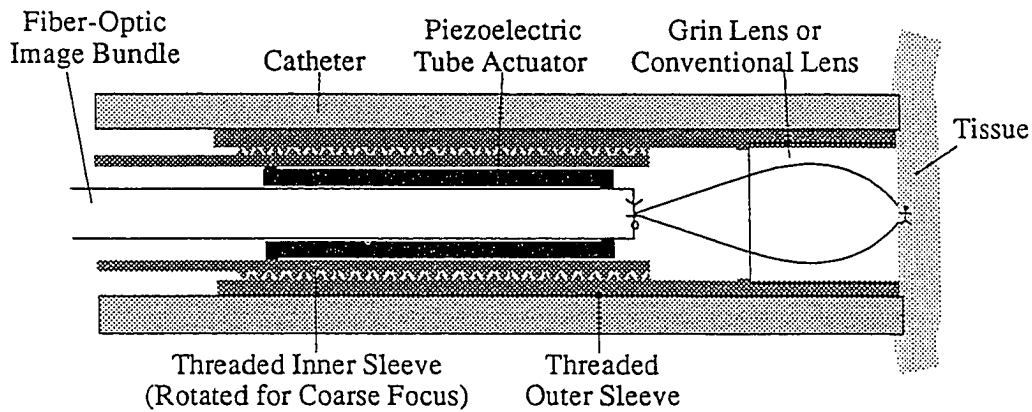


Figure 5.21. Preliminary design of a stabilizing and focusing mechanism for the fiber-optic imaging-bundle confocal microscope.

5.3. Slit-scanning fiber-optic imaging-bundle confocal microscope

One of the reasons for developing a fiber-optic imaging-bundle confocal microscope is for in-vivo medical examinations (optical biopsies). The pinhole-scanning Zeiss LSM10 microscope requires 2 seconds to collect a 512×512 pixel image (two-dimensional raster scan). This is not fast enough for many medical applications. We have developed a slit-scanning system to take advantage of the speed gains described in chapter 2. By scanning in only one-dimension and collecting an entire line of data simultaneously, we can operate the system in real-time (30 frames per second).

System design

The slit-scanning fiber-optic imaging-bundle confocal microscope is shown in Figure 5.22. Unfolded diagrams of the illumination and detection paths are shown in figures 5.23 and 5.24, respectively.

An argon laser beam (514 nm) is spatially filtered and collimated by the beam expander. This collimated beam (diameter ≥ 12.5 mm) is then focused by cylindrical lens, L3 ($f_3 \approx 500$ mm), to a vertical line focus at the 100 micron wide illumination slit. The illumination slit is used to clean up the beam and may not be necessary if a high quality cylindrical lens, L3, is available. The light passing the slit is imaged by lenses L4 ($f_4 = 400$ mm) and L5 ($f_5 \approx 16$ mm) onto the proximal face of the fiber bundle. The light passing the illumination slit is demagnified 25 times by the afocal L4 / L5 lens pair, yielding a vertical line illumination at the bundle that is approximately 4 microns wide and at least 0.5 mm long (the diameter of the Sumitomo IGN-05/10 bundle). The line illumination is relayed to the distal end of the bundle, where it is imaged by lens L9 onto the sample.

The line illumination is scanned across the proximal face of the bundle, and therefore across the sample, by a one-dimensional galvanometer scan mirror. The required mirror scan angle is

$$\theta_{mirror} = \pm \frac{\text{Bundle radius}}{2(f_5)}. \quad (5.6)$$

A mirror scan angle of ± 0.45 degrees is required for a 0.5 mm diameter bundle and Lens L5 focal length of $f_5 = 16$ mm. The galvanometer mirror should, ideally, be located in the entrance pupil of lens L5, or in an image of this entrance pupil, in order to avoid vignetting. Lens L5 has been implemented with a microscope objective, and it is impossible to place the scan mirror in the entrance pupil of this lens. Rather than including a relay lens system to image the scan mirror into the entrance pupil of L5,

we have chosen to place the scan mirror as close as possible to L5 and accept a small amount of vignetting.

The detection slit is located in a conjugate position to the source slit and imaged onto the same point on the proximal bundle face by the afocal lens pair L5 / L6. The detection slit image is scanned by the galvanometer mirror across the proximal end of the fiber bundle, matching precisely the path of the source slit image. Lens L6 ($f_6 = 400$ mm) is identical to lens L4, and the demagnification of the detection slit is also twenty-five times. The width of the detection slit image impacts the degree of optical sectioning, as explained in chapter 2. The $3.4\text{ }\mu\text{m}$ average diameter of the cores in the Sumitomo bundle makes reduction of the detection slit image below this point of marginal use. A narrower slit does not produce an improvement in the axial or lateral resolution, and comes at the expense of increased light rejection, and, therefore, reduced signal. This is due to the fact that the optical-sectioning performance is determined by the size of the source and detection slit image at the sample, which can never be smaller than the images of the fiber cores. Therefore, the minimum practical detection-slit width in this system is on the order of $75 - 100\text{ }\mu\text{m}$.

Light that is collected from the sample and passes the detection slit is imaged by lenses L7 ($f_7 = 400$ mm) and L8 ($f_8 = 254$ mm) onto the CCD array. The light reflects off the scan mirror between lenses L7 and L8. This causes the light collected from the sample and passed by the detection slit to be scanned across the CCD. The CCD is allowed to integrate during the entire scan time and (ideally) is read out during the scan return.

The magnification of the proximal end of the imaging bundle onto the CCD array is a function of lenses L5, L6, L7, and L8. The vertical magnification is given by

$$M_{vert} = \left(\frac{f_6}{f_5} \right) \left(\frac{f_8}{f_7} \right), \quad (5.7)$$

where the two lens pairs L6 / L5, and L8 / L7 are both afocal. The horizontal magnification is determined by the scan angles in conjunction with the focal lengths of lenses L5 and L8. The two beam paths (detection slit imaged onto bundle and detection slit imaged onto CCD) use the same scan mirror, so the horizontal magnification of the bundle image on the CCD array is

$$M_{horiz} = \frac{f_8(\theta_{scan})}{f_5(\theta_{scan})} = \frac{f_8}{f_5}, \quad (5.8)$$

where

$$\theta_{scan} = 2\theta_{mirror}. \quad (5.9)$$

The condition $f_6 = f_7$ is necessary to maintain the correct ratio in the image ($M_{vert} = M_{horiz}$). The image of the bundle on the CCD is magnified by the ratio $(f_8 / f_5) \approx 15.9$. The sizes of the fiber cores in this image are approximately $(15.9)(3.4 \mu\text{m}) = 54 \mu\text{m}$. This is several times the size of the CCD pixels; thus, the CCD will not significantly degrade the resolution.

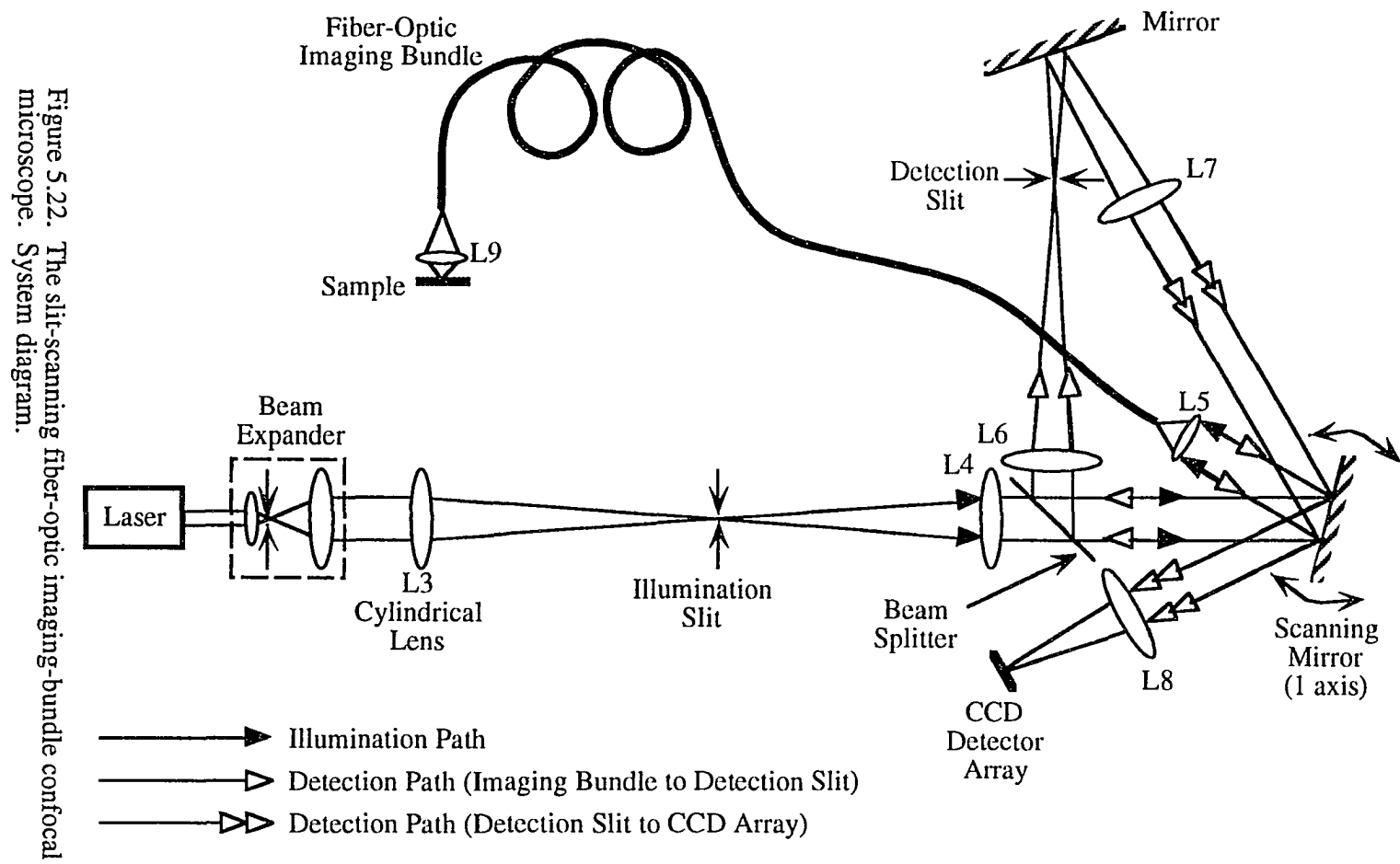


Figure 5.22. The slit-scanning fiber-optic imaging-bundle confocal microscope. System diagram.

Figure 5.23. The slit-scanning fiber-optic imaging-bundle confocal microscope. Unfolded illumination path.

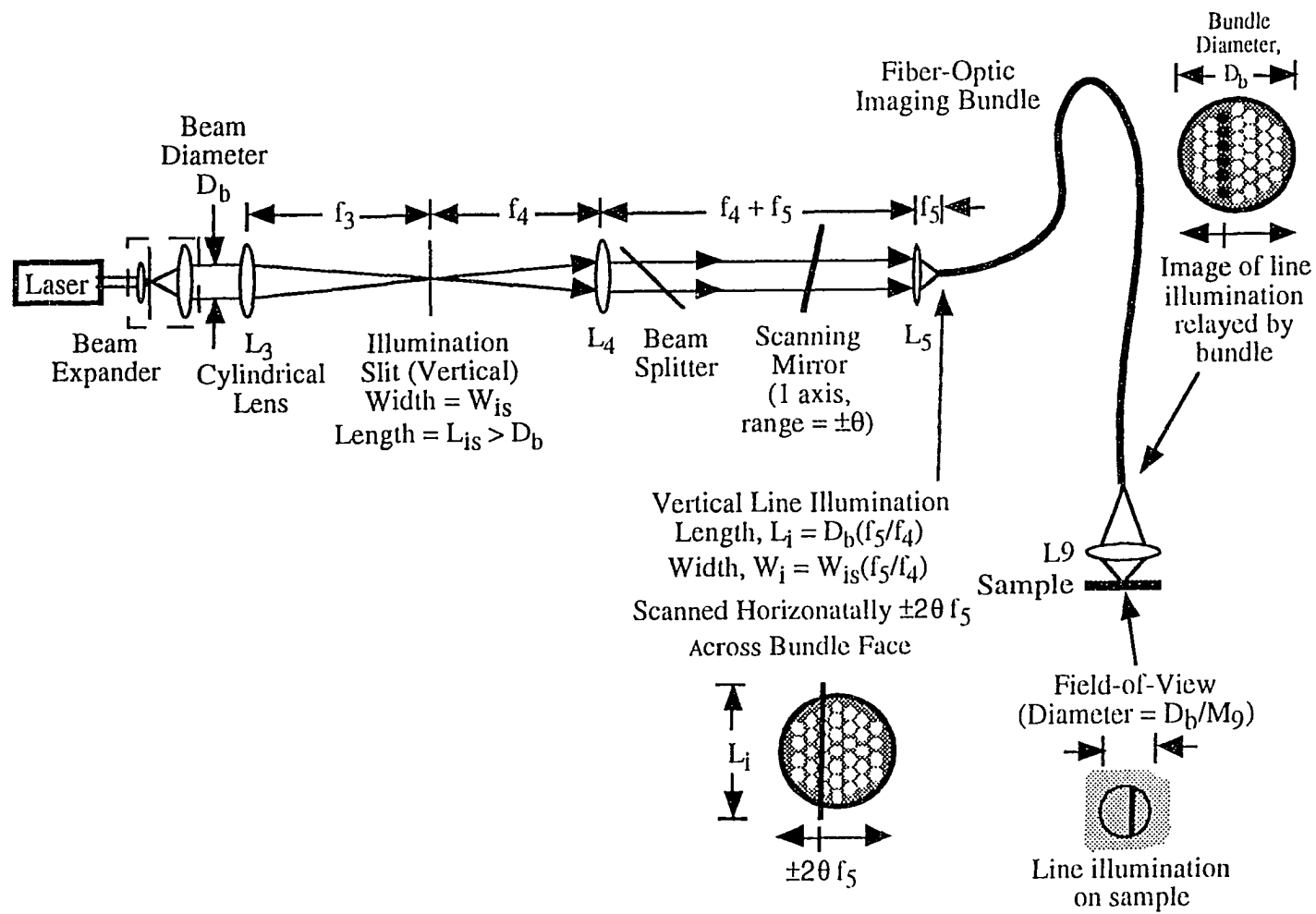
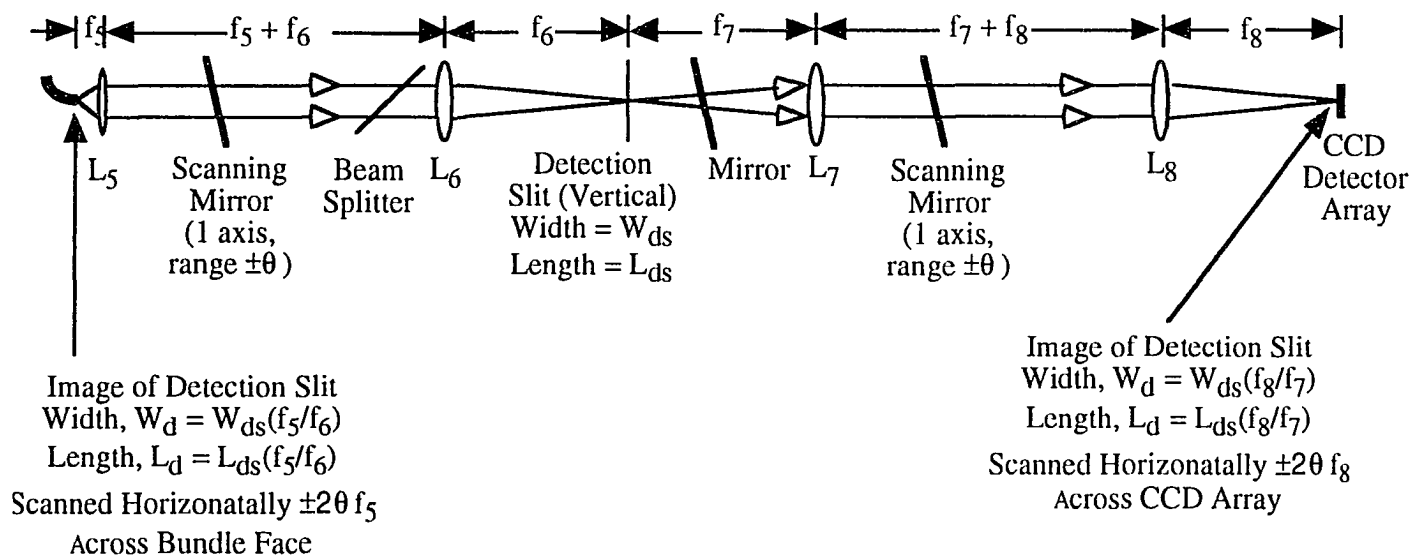


Figure 5.24. The slit-scanning fiber-optic imaging-bundle confocal microscope. Unfolded detection path.



The beamsplitter used to combine the illumination and detection paths should be as thin as possible. As seen in Figure 5.23, the vertical illumination slit is at the front focal point of lens L4. The beam leaving lens L4 is therefore converging to a horizontal line focus at the back focal plane of L4. Inclusion of a tilted plane-parallel plate in this non-collimated beam aberrates the beam, with the amount of aberration proportional to the thickness and tilt angle of the plate. We have used a pellicle beamsplitter to minimize aberration. However, preliminary examination of a 3 mm thick window in place of the pellicle beamsplitter indicates that the line illumination is not significantly degraded. It is not known to what extent a dichroic beamsplitter will degrade the imaging of the CCD detector array onto the fiber bundle. Some dichroics are built with the dielectric layers placed between two thin glass plates. The detection beam in this case will be aberrated by these plates.

The ideal scan pattern for the mirror is a sawtooth wave with the image readout occurring while the mirror returns during the fast-scan portion of the waveform. In this case, scanning is always performed in the same direction, and each portion of the object is sampled at the same interval.

The sawtooth wave puts the maximum demand on the scan mechanism due to the need to quickly return to the start of the scan range. Alternate patterns are triangle and sine waves, where the camera is read out twice per cycle during periods of overscan (when the illumination and detection slit images are scanned beyond the edge of the bundle). These patterns have the advantage that real-time (30 frames per second) operation can be achieved with a fundamental frequency of 15 Hz, rather than the 30 Hz required

with the sawtooth waveform. The higher frequency content is also less with a triangle wave than a sawtooth, and there are no harmonics with a sine-wave.

The maximum scan frequency of a galvanometer scanner is limited by the inertia of the scan mirror and galvanometer armature. The inertia of a uniform thickness round mirror can be calculated by

$$\text{Mirror Inertia} = \left(\frac{\pi D^4 T \rho}{64} \right) + \left(\frac{\pi D^2 T^3 \rho}{48} \right), \quad (5.10)$$

where D , T , and ρ are the mirror diameter, thickness, and density, respectively.¹⁰⁹

We have used a 5 cm diameter, 3.2 mm thick, fused-silica scan mirror (density = 2.2 grams/cc) in the system of Figure 5.22. The inertia of this mirror is 21.7 grams-cm², which limits the maximum sinusoidal scan frequency of the General Scanning G302 galvanometer to approximately 180 Hz (85% of the resonant frequency).¹⁸ The G302 can scan this mirror with sawtooth or triangle waves up to approximately 10 Hz (5% of the resonant frequency). We have found experimentally that a 15 Hz triangle wave produces noticeable scan rate non-linearities across the field. A smaller or lighter mirror would allow this scanner to be operated in real-time with a sawtooth or triangle scan pattern.

The scanner appears to accurately scan a 15 Hz sine wave, which is the condition we have used to collect the images of Figures 5.25 and 5.26. The angular velocity of the mirror, and, therefore, the scan rate of the slit images, varies across the field with a sine-wave scanning pattern. This results in slower scanning at the edges of the field,

which produces an intensity variation but no distortion in the image. While this is not a problem with the samples we have examined, it should be considered in future designs.

Performance

We have collected several images to demonstrate the imaging performance of the slit-scanning fiber-optic imaging-bundle confocal microscope. Figure 5.25a is a confocal image of a portion of a business card coated with fluorescent ink. Figure 5.25b is a non-confocal image of the same portion of the business card, where the detection slit has been opened to at least 10 times the width used for the confocal case. This demonstrates the optical-sectioning capability of the slit-scanning confocal system. The blurry image in Figure 5.25b is due to the thickness of the sample. Light from multiple axial locations is being coupled to the detector, resulting in a blurry image. The detection slit is effectively "sectioning" away light from out-of-focus planes in Figure 5.25a, leaving an image of a single axial plane in the sample. The horizontal lines in Figure 5.25 are generated during the processing of the images. The pixels in the CCD camera have an aspect ratio of 1.67:1, and the images were resized to recover the original image proportions. These lines were not present in the original image.

Figure 5.26 is a reflection image of a U.S. Air Force bar target. Spatial frequencies of the bars in the image vary from 128 lines/mm to 228 lines/mm.¹¹⁰ The magnification of the distal lens was approximately 2x. This results in a range of spatial frequencies at the bundle of 64 lines/mm to 114 lines/mm. 115 lines/mm is the predicted upper limit for the lateral resolution of the bundle based on sampling. The highest spatial frequency bars (at the bottom of the image) is visible, but it appears unlikely that

significantly higher spatial frequencies can be imaged with the system. This reflection image is fairly noisy, demonstrating again the difficulty of reflection-mode operation of the imaging-bundle confocal microscope.

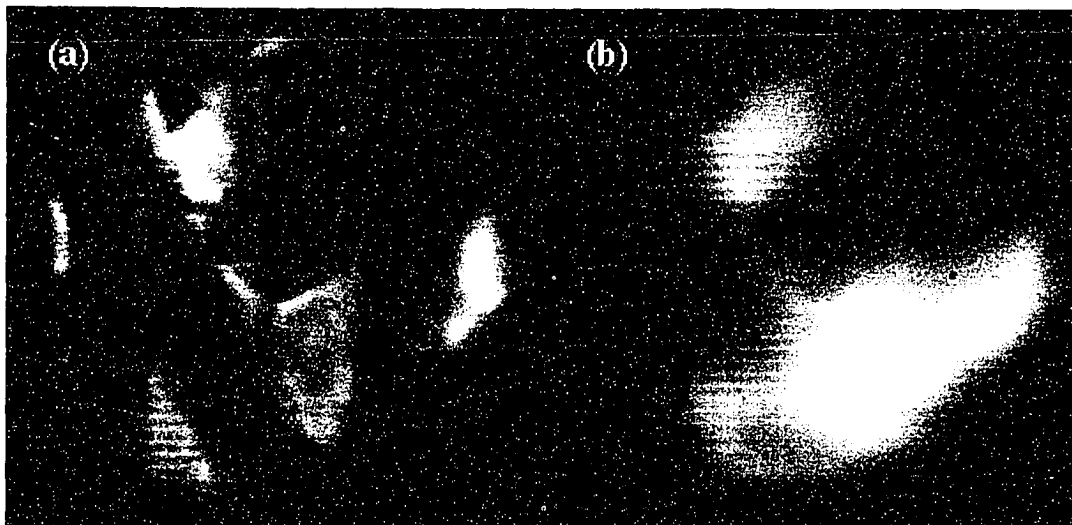


Figure 5.25. Fluorescence images obtained with the slit-scanning fiber-optic imaging-bundle confocal microscope. Figure 5.25a is an image of a portion of a business card coated with fluorescent ink. Figure 5.25b is a non-confocal image of the same portion of the business card, where the detection slit has been opened to at least 10 times the width used in the confocal case of Figure 5.25a.

5.4. Applications

There are a number of potential applications of the fiber-optic imaging-bundle confocal microscope. The optical-sectioning effect can be used to acquire three-dimensional images and to perform sub-surface imaging. One possible application of this system is determination of the invasiveness of cancer. The degree to which cancer cells have invaded below the surface of the basement membrane is an important metric

in the staging of some cancers. It is possible with a confocal microscope to look below the surface of an accessible biological object such as the skin or cornea. The fiber-optic imaging-bundle confocal microscope has the potential to extend this capability to many other areas of the body.

Several possibilities exist for the application of this system in biological research and industrial inspection. This includes environmental chambers used in research or product development, as well as a number of other difficult to reach locations (e.g. inside airplane wings). In general, the range of applications will be limited by the size and performance of the imaging bundle, the distal imaging lens, and the positioning mechanism.

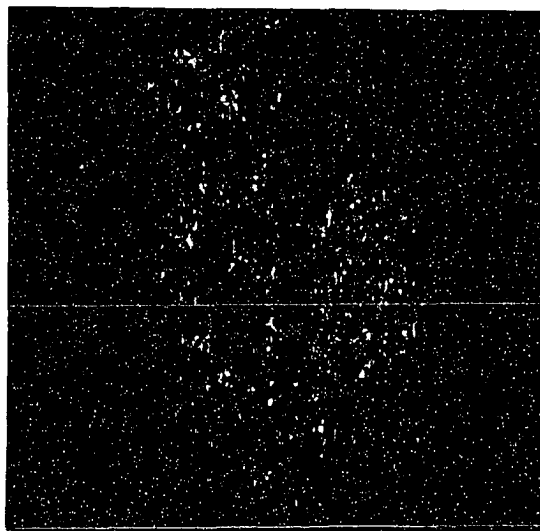


Figure 5.26. Reflection image of a U.S. Air Force bar target obtained with the slit-scanning fiber-optic imaging-bundle confocal microscope. Spatial frequencies of the bars in the image vary from 128 lines/mm to 228 lines/mm.

6. CONCLUSION

This dissertation has described the implementation of confocal microscopy through a fiber-optic imaging bundle. A review of the basic principles of both confocal microscopy and optical fibers has been included. The characteristics of imaging bundles have been discussed, and three silica imaging bundles analyzed and compared. Finally, the fiber-optic imaging-bundle confocal microscope has been described and the design and performance of two systems discussed. This new type of microscope holds promise in the study of thick objects in difficult-to-reach locations. This is relevant in in-vivo medical applications as well as industrial inspection tasks.

There are several tasks remaining in the design of a useful system. The distal imaging lens (at the sample end of the bundle) needs to be miniaturized. This lens has been implemented with a pair of back-to-back microscope objectives. This is adequate for evaluation of system performance, but needs to be modified for real applications. A preliminary, monochromatic, gradient-index lens design was given in chapter 5. This lens has a diameter of 1 mm and a length of 5.4 mm. The design needs to be revised to accommodate dispersion for polychromatic (e.g. fluorescence) applications. Alternate designs including micro-lenses should also be considered. The back-to-back pair of microscope objectives may be a good starting point for this endeavor. A Lister-type low-power objective was used to couple light into and out-of the bundle, while a high-power oil-immersion objective was used adjacent to the sample. These objectives are corrected for larger fields and wider wavelength ranges than are likely to be necessary in the fiber-optic imaging-bundle confocal microscope. This may allow simplified versions of these designs to be used in this system.

It is also necessary to design a positioning and focusing mechanism for the distal imaging lens. This has been accomplished previously with conventional optical positioning equipment. The number of potential in-vivo medical applications falls quickly with the size of the distal lens and positioning mechanism. Thus, it is desirable to minimize the size of this device. A possible design for the focusing mechanism was shown in Figure 5.21.

The two confocal systems that were built as part of this work employ a Sumitomo Electric Corp. IGN-05/10 (0.5 mm diameter, 10,000 fibers) silica imaging bundle. As described in the previous chapters, the important bundle parameters are resolution number of fibers, losses, and flexibility. Silica imaging bundles offer the best combination of these properties for the fiber-optic imaging-bundle confocal microscope. Based on the analysis of chapter 4, it appears that the slightly lower resolution of the Fujikura bundle (with respect to the Sumitomo bundle) may be acceptable in exchange for higher coupling efficiency. The Fujikura bundle evaluated above is a member of their "C" series. It is expected that the performance of the "N" and "S" series Fujikura bundles will be progressively better than that of the "C" series, and their use should be considered.¹¹¹

Finally, it is necessary to apply this system to relevant problems. Images have been collected of fixed samples on microscope slides, as well as objects such as business cards and resolution targets. The next logical step in terms of medical applications is to look at a living system such as a cell culture. This can be accomplished using the current distal lens implementation (microscope objectives and conventional optical

positioning equipment). This will allow demonstration of imaging of live samples. It may also be possible to examine skin in-vivo with the current implementation, such as demonstrated in Figure 2.8 with a conventional confocal microscope. The ultimate goal of this work is to design and demonstrate a full in-vivo system with miniaturized distal optics.

APPENDIX A. CONFOCAL MICROSCOPY REFLECTION TECHNIQUE FOR MEASURING THE INDEX OF REFRACTION OF OPTICAL FIBERS AND FIBER-OPTIC IMAGING BUNDLES

An important part of this work is evaluation of fiber-optic imaging bundles. A new, non-destructive, technique for measuring the refractive index of optical fibers and fiber-optic imaging bundles was developed, and is described in this chapter. This technique was used to evaluate three silica imaging bundles. The results of this evaluation are described in this chapter and used in chapter 4.

A.1. Introduction

The reflection of light from an interface between materials of differing refractive indices can be calculated using the Fresnel reflection coefficients. These coefficients are a function of the two indices of refraction (incident medium and transmitted medium), the angle of incidence, and the state of polarization.

The Fresnel reflection coefficients are defined for plane waves incident on a planar boundary between lossless, isotropic, homogenous media. By measuring the amount of light reflected from a boundary between a known index material and an unknown index material, it is possible to calculate the unknown refractive index.

In order to guide light, an optical fiber must necessarily contain lateral variations in the index of refraction. In high-resolution fiber-optic imaging bundles and single-mode telecommunications fibers, these index variations occur over distances comparable to a wavelength.^{31,42} To make high spatial-resolution measurements of the light reflected from an optical fiber or some other material with a spatially-varying

refractive index, it is necessary to focus the light onto a small point on the face of the fiber. Light converging to the focal point of a lens can be described as a superposition of plane waves.^{112,113} This results in a range of incidence angles and polarizations.

By measuring the reflection from a set of reference materials of known refractive indices, it is possible to determine the relationship between reflected intensity and refractive index for a specific experimental configuration. An object with unknown index of refraction can then be examined and its index of refraction determined. We have used this technique to determine the index of refraction of several silica fiber-optic imaging bundles. The reference materials are optical windows with constant index of refraction. We assume that the index variation of the fibers is gradual relative to the size of the focal spot, so that the reflected intensity is a function of the refractive indices at the focal point. This is equivalent to a geometrical optics assumption of zero wavelength.

We used an epi-illumination confocal scanning microscope for the experiments described. With high numerical-aperture oil-immersion objectives, the lateral resolution (FWHM) of this confocal microscope is approximately one-third of a wavelength, making possible detailed analysis of fibers with dimensions as small as a few microns.¹⁶

Our interest was in the measurement of fiber-optic imaging bundles. These bundles are composed of hundreds or thousands of fibers in a fixed spatial arrangement. The highest resolution bundles are made with doped silica cores and clads, where the clads have been fused together. During the fusing process used prior to drawing the bundle

down to its final size, stresses are placed upon the fibers such that they often deform, resulting in oddly shaped fibers. This can be seen in Figure 4.4, which shows images of small portions of three silica imaging bundles. Thus, no assumptions can be made about the symmetry of the fiber to simplify the measurement, and it is necessary to measure the full two-dimensional profile of the index of refraction.

Reflection methods have been used to measure the refractive index profiles of optical fibers. These techniques are similar to the technique used in this paper, but offer somewhat lower resolution. Ikeda, Tateda, and Yoshikiyo¹¹⁴ and Eickoff and Weidell¹¹⁵ assume that the reflection can be approximated by the Fresnel coefficients at normal incidence, and show there is an approximately linear relationship between index variation and reflected intensity for small index changes. Ikeda, et. al. estimated a resolution of 1 μm (based on the 0.5 μm spot size) and an error of less than 4.3% in the refractive index measurement. Eickoff and Weidell report a resolution of approximately 1 μm and an error in refractive index of less than 1%. Costa and Sordo point out that the sensitivity of the reflection technique can be improved by using an incident medium of nearly the same refractive index as the fiber, although as we shall see below this increases the error of the assumed linear relationship.¹¹⁶

Tateda improved the resolution of the reflection method to approximately 0.3 μm by including the effect of the spatial distribution of the focused laser beam on the reflected signal.¹¹⁷ He applied this only to axially symmetric fibers, however, and it is unclear whether it can be readily modified to evaluate arbitrary index profiles.

Zhu and Iga devised a technique for determining the refractive index by measuring the critical angle when a material of higher refractive index is optically coupled to the test sample.¹¹⁸ This eliminates the linear relationship assumption described above. The technique yielded a lateral resolution of 1 - 2 μm due to the low numerical aperture of the test beam. The low numerical aperture appears to have been necessary to accommodate the 5.5 mm diameter sphere used for the coupling medium, but could be increased to obtain submicron resolution.

Ruschin, et. al. have implemented a filtered Fourier transform technique to determine the refractive index profile of optical waveguides. This requires certain assumptions to be made about the structure of the waveguide, such as the functional form of the index profile, and may therefore be unsuitable for arbitrary profiles.¹¹⁹

A number of other techniques exist for determining the refractive index profile of an optical fiber. These include scanning electron microscopy, local numerical aperture (near-field pattern), interferometry, optical tomography, and calculations of index distribution from bound modes. None of these techniques offer high-resolution non-destructive measurements of arbitrary index profiles. Summaries of these techniques are given by Okoshi⁴⁴ and Ghatak and Thyagarajan.¹²⁰ More recently, an atomic force microscope method has been reported by Zhong and Inniss.¹²¹ Some of the techniques are suitable only for axially symmetric fibers, and therefore cannot be applied to the evaluation of imaging bundles.

A.2. Theory of the reflection method

The reflected intensity of a plane wave at normal incidence is given by

$$R = \left(\frac{n_2 - n_1}{n_2 + n_1} \right)^2, \quad (\text{A.1})$$

where n_1 and n_2 are the refractive indices of the incident and transmitted media, respectively. This is the form assumed by Ikeda, et. al., Eickoff and Weidell, Costa and Sordo, and Tateda to be valid for the case of a focused beam.

The reflected intensity, R , predicted by equation (A.1) is plotted in Figure A.1 as a function of n_2 for fixed n_1 . The range of transmitted indices, $n_2 = 1.45 - 1.50$ is chosen to correspond to the range expected for silica image bundles.⁴³ Figure A.1a shows that for air as the incident medium ($n_1 = 1.0$), the reflected intensity as a function of n_2 is approximately linear. Figure A.1b shows the reflected intensity for immersion oil as the incident medium ($n_1 = 1.518$). The improvement in sensitivity due to the immersion oil is accompanied by an increase in the error of assuming a linear relationship between reflected intensity and index variation, as well as a reduction in signal.

Errors due to the assumed linear relationship generally increase with the numerical aperture of the beam. Therefore, the resolution and accuracy of the reflection technique employing equation (A.1) cannot be increased simultaneously. In order to evaluate the impact of numerical aperture on the accuracy of the technique, we have developed a simple theoretical model to calculate the total reflected intensity for a converging beam.

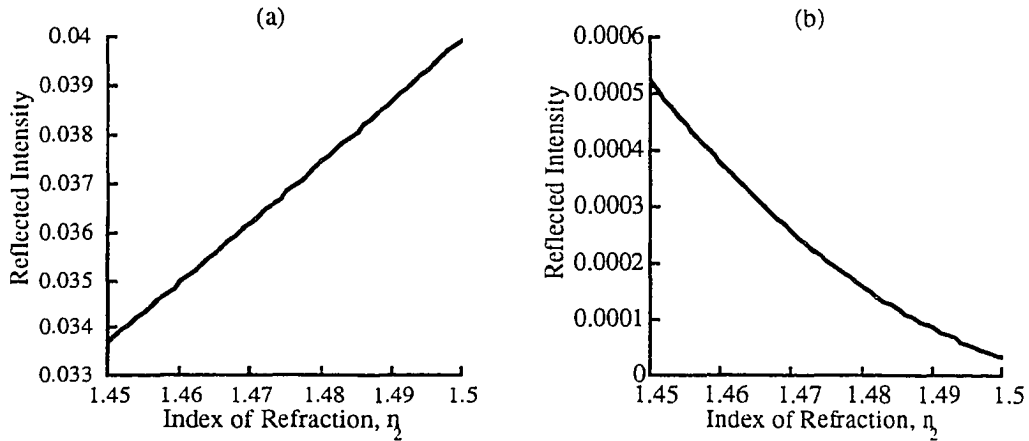


Figure A.1. Reflected intensity versus refractive index of the transmitted medium, n_2 , for normal incidence. Figure A.1a is for an incident medium of air (index, $n_1 = 1.0$) and Figure A.1b is for an incident medium of immersion oil (index, $n_1 = 1.518$).

The model assumes an aberration-free lens focusing a linearly polarized, collimated beam onto a plane interface between dielectrics of different refractive index. A converging beam can be viewed as a combination of plane waves, each having a propagation direction determined by the position in the exit pupil through which it passes. For small angles of incidence with respect to each lens surface, the orientation of the electric field with respect to the meridional plane will be unchanged by refraction.¹²² Thus, the polarization with respect to the final meridional planes is unchanged from that with respect to the initial meridional planes (each "ray" in the beam has a meridional plane at each refracting surface, determined by the local surface normal and the ray propagation direction).

The reflection of each plane wave from the interface at the focal point of the lens can be described by the two polarization components (parallel and perpendicular to the meridional plane) multiplied by the appropriate Fresnel reflection coefficients for that plane wave's angle of incidence. The resulting electric field for each point in the pupil of the collection lens can then be calculated from the vector sum of the two polarization components of the reflected plane waves. The total reflected intensity is calculated by integrating the magnitude squared of the electric field across the pupil. We assume that all reflected light is detected. A diagram of this model is shown in Figure A.2

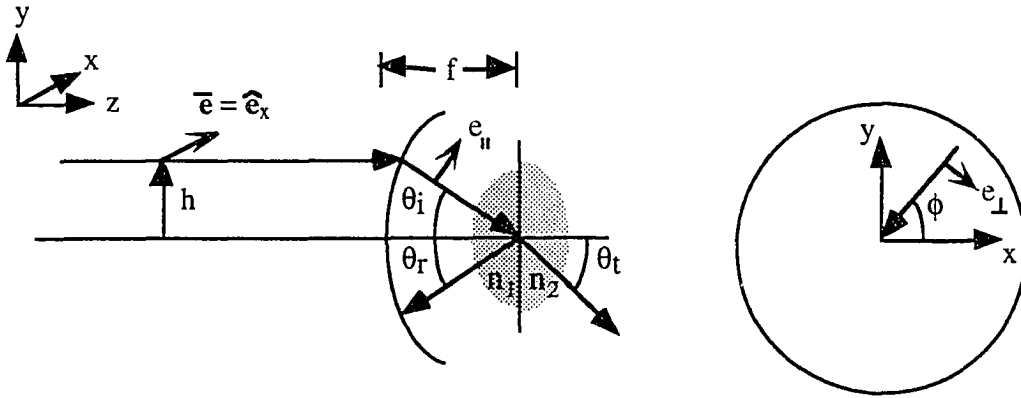


Figure A.2. Diagram of theoretical model for calculating reflected intensity as a function of refractive indices, n_1 and n_2 , and numerical aperture, $n_1 \sin(\theta_i)$.

Rays of light in the illumination beam will be mapped by an aberration-free lens into converging rays according to the sine condition

$$h = f \sin(\theta_i), \quad (\text{A.2})$$

where h is the radial position of a ray in the illumination beam and f is the focal length of the lens.

For an incident beam with unit amplitude and linearly polarized in the x direction, the polarization components with respect to the meridional plane are

$$\begin{aligned} e_{\parallel} &= \cos(\phi) \\ e_{\perp} &= \sin(\phi) \end{aligned} \tag{A.3}$$

in the collimated illumination beam, at each lens surface, and at the focal point. The angle ϕ is defined in Figure A.2.

The Fresnel reflection coefficients are

$$\begin{aligned} r_{\parallel} &= + \frac{\tan(\theta_i - \theta_t)}{\tan(\theta_i + \theta_t)}, \\ r_{\perp} &= - \frac{\sin(\theta_i - \theta_t)}{\sin(\theta_i + \theta_t)} \end{aligned} \tag{A.4}$$

where

$$n_1 \sin(\theta_i) = n_2 \sin(\theta_t). \tag{A.5}$$

The electric field strength for each position in the pupil of the collection lens can then be calculated with

$$e(h, \phi) = \sqrt{(e_{\parallel} r_{\parallel})^2 + (e_{\perp} r_{\perp})^2} \quad (\text{A.6})$$

where r_{\parallel} and r_{\perp} are, in this case, written as functions of h using equations (A.2), (A.4) and (A.5).

Finally, the total reflected intensity is found by integrating the reflected intensity across the collection lens pupil

$$R = \iint_{\text{pupil}} [e(h, \phi)]^2 h dh d\phi. \quad (\text{A.7})$$

The model can be applied to elliptically and circularly polarized light by describing them as a combination of linearly polarized components. Since the total reflected intensity includes angles, ϕ , varying from 0 through 2π , a combination of linear polarizations will have the same total reflected intensity as a single linear polarization of the same total incident intensity.

Applying this model to the test conditions of Eickoff and Weidell (0.85 NA, $n_1 = 1.0$, $n_2 = 1.5$), we obtain the reflected intensity in the exit pupil of the collection lens shown in Figure A.3. The effect of polarization on reflection is clearly seen, with portions of the pupil yielding an intensity reflection of almost 16% (perpendicular polarization) and other portions yielding almost no reflection (parallel polarization near Brewster's angle). The average reflection (intensity) over the pupil is 4.9%, as opposed to the 4% predicted by the on-axis Fresnel coefficient given in equation (A.1).

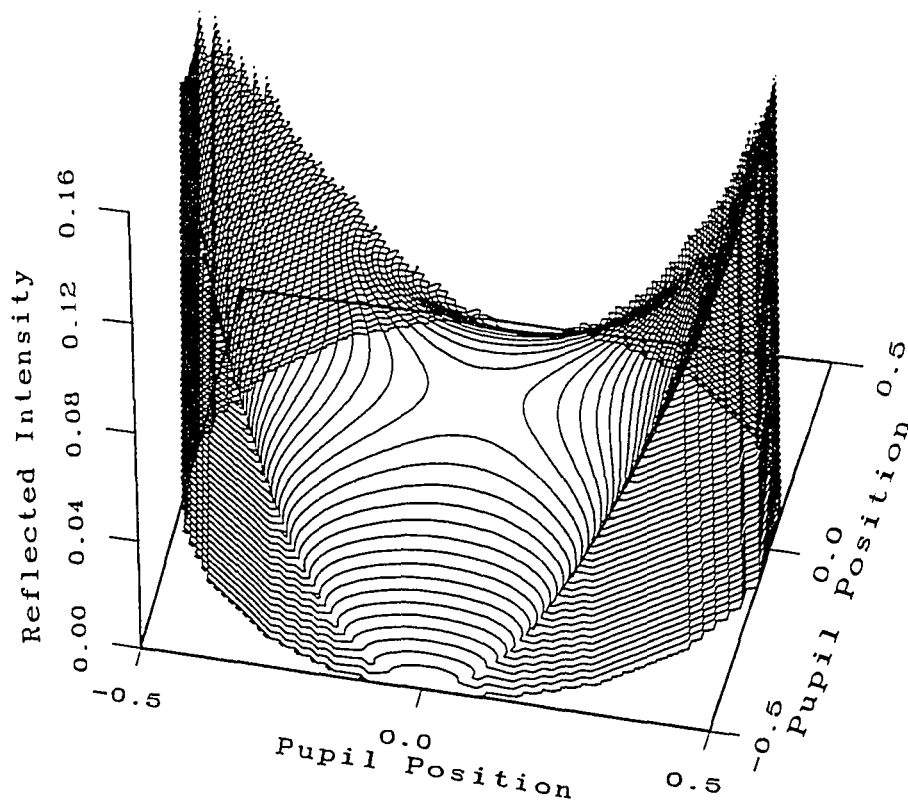


Figure A.3. Reflected intensity in the exit pupil of the collection lens for an 0.85 NA aberration-free lens with $n_1 = 1.0$ and $n_2 = 1.5$. The incident light is a linearly polarized plane wave which is mapped by the objective lens into a range of incidence angles and polarizations. The high reflected intensity regions in this figure correspond to light that is primarily perpendicularly polarized at the $n_1 - n_2$ interface. The low reflected intensity regions at the edge of the pupil are for parallel polarized light near Brewster's angle. The on-axis reflected intensity at the center of the pupil (position 0,0) is approximately 4%. Average reflected intensity across the pupil = 4.9%.

The error in using equation (A.1) increases with numerical aperture. Figure A.4a shows the predicted total reflected intensity for air immersion ($n_1 = 1.0$ and $n_2 = 1.5$), while Figure A.4b shows the result for oil immersion ($n_1 = 1.518$ and $n_2 = 1.46$). In each case, the total reflected intensity in the collection pupil remains within 5% of the result from equation (A.1) for numerical apertures whose steepest angles are no more than 75% of Brewster's angle. This corresponds to numerical apertures of 0.67 and 0.82 for the air-immersion and oil-immersion cases described here, respectively.

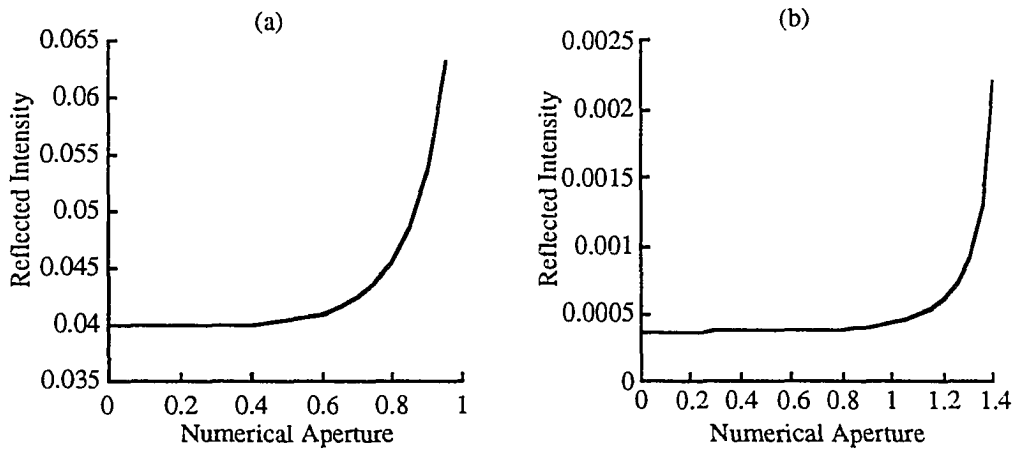


Figure A.4. Total reflected intensity as a function of numerical aperture for cases of air immersion (Fig. A.4a, $n_1 = 1.0$ and $n_2 = 1.5$) and oil immersion (Fig. A.4b, $n_1 = 1.518$ and $n_2 = 1.46$).

It is possible with this model to estimate the effect of a tilted surface, which decreases the collected signal due to vignetting of the reflected beam by the objective lens. This effect is shown in Figure A.5, where the reflected beam is deviated by twice the angle of the sample surface. This is potentially an important source of error in high numerical-aperture systems since the lost light is at the edges of the pupil. The

reflectivity increases monotonically with incidence angle for perpendicularly (s) polarized light. It decreases to zero at Brewster's angle and increases rapidly beyond for parallel (p) polarized light. Thus, the error due to surface tilt varies with tilt orientation for a linearly polarized source.

Surface tilt about the axis in the direction of polarization of the incident collimated beam will result in the maximum effect due to vignetting of portions of the beam that are polarized perpendicular to the plane of incidence. This effect is shown in Figure A.7 for $n_1 = 1.518$, $n_2 = 1.46$, and $NA = 1.2$. In this figure, the tilt angle, α , varies from 0 to 10 degrees, while the tilt orientation angle, ϕ_2 , varies from 0 to 90 degrees in 22.5 degree increments. The greatest effect is seen for $\phi_2 = 90$, where the vignetted light is primarily polarized perpendicular to the meridional plane (see equation (A.3)). The least effect occurs at $\phi_2 = 0$ degrees. For a circularly polarized source, tilts with any orientation will have the same effect as a tilt at $\phi_2 = 45$ degrees with a linearly polarized source.

The effect of vignetting due to a tilted surface can be reduced by using a smaller numerical aperture beam. This, however, comes at the expense of reduced resolution. Vignetting due to surface tilt can be avoided by slightly underfilling the entrance pupil of the objective with the illumination beam, thereby ensuring that all the reflected light will be detected.

It is possible with the optical-sectioning effect of a confocal microscope to evaluate the magnitude and orientation of surface tilt, and, in principle, to correct for the vignetting. With a tilted sample, the optical-sectioning effect results in only a small

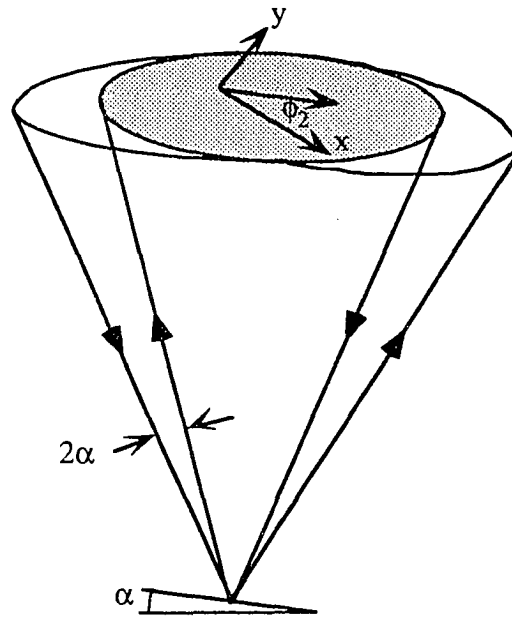


Figure A.5. Vignetting of the reflected beam by the collection lens due to a tilted surface. Orientation of the surface tilt, ϕ_2 , is important for a linearly polarized source due to the difference in reflectance for parallel and perpendicular polarizations.

region being visible in an image. Figure 1.1 shows a tilted fiber bundle imaged with a confocal microscope, where only a band in the center of the image is in-focus.

Measuring the amount of axial motion necessary to scan the focal plane across the sample allows determination of the tilt magnitude and orientation, assuming the image size is known. Data collected for the sample can then be corrected by scaling by the appropriate factor, as indicated by the curves of Figure A.6. For reference samples of constant index, a single scaling factor is necessary to account for tilt. For test samples, the relationship between n_2 and R will be modified by a scaling function, $R(n_2; \alpha, \phi_2) = R(n_2) \times F(\alpha, \phi_2)$. The scaling function, $F(\alpha, \phi_2)$, may be obtained either theoretically or experimentally. Alternatively, the optical-sectioning effect of the confocal microscope

can be used in conjunction with a tip-tilt stage to ensure horizontal surfaces, thereby eliminating the effects of tilt and the need for correction of the data.

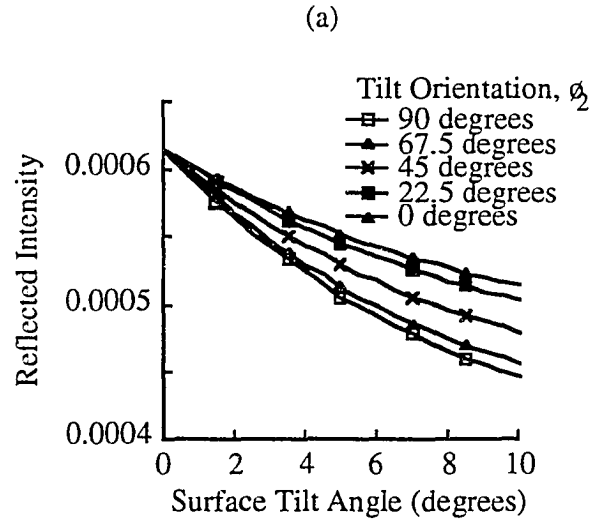


Figure A.6. Effect of surface tilt magnitude, α , and tilt orientation, ϕ_2 , on the total reflected intensity. This figure shows the case of a 1.2 NA lens with tilt orientations of 0 - 90 degrees, where $n_1 = 1.518$ and $n_2 = 1.46$.

We summarize the results of the model as follows. The assumption of a linear relationship between refractive index and reflected intensity is a reasonable approximation for air-immersion systems over index ranges of a few percent. The linear approximation is poorer for oil-immersion systems, and is unsuitable for examining silica imaging bundles with index variations of 2 - 4% (index range of approximately 1.45 to 1.50). Significant errors due to this approximation occur with high NA lenses. Errors due to a tilted surfaces can be significant, but can be avoided or corrected with the technique. This ability to eliminate or correct for tilt is an

advantage of the confocal microscope over a non-confocal microscope in this technique.

We describe below the experimental setup used to measure the reflected intensity from a set of reference materials (optical windows). Figure A.7 shows a comparison of experimental measurements obtained with a 1.4 NA oil-immersion objective (filled in squares) and the model prediction (solid line) for this numerical aperture. The model data were scaled and shifted to match the endpoints of the experimental results. The experimental setup in this case differs slightly from that shown in Figure A.8. The microscope was operated in a non-confocal mode (no detection pinhole) to collect as much light as possible and to best approximate the conditions of the theoretical model.

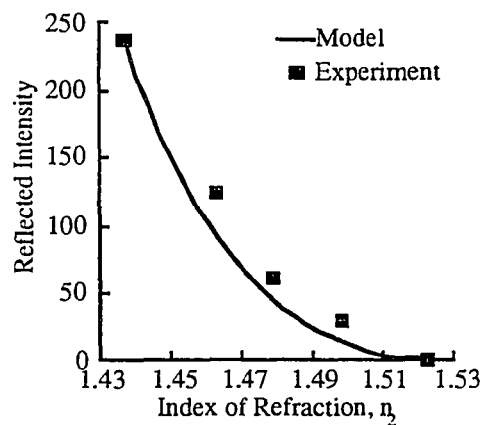


Figure A.7. Comparison of theoretical and experimental results for a 1.4 NA oil-immersion ($n_1 = 1.518$) lens. The experimental results follow a somewhat flatter curve than the theoretical prediction. The detection pinhole aperture was not included in the system in order to approximate the conditions of the theoretical model. For this experiment, a 488 nm argon laser was used rather than the 543 nm helium-neon laser indicated in Figure A.8.

Figure A.7 shows that the experimental results follow a somewhat flatter curve than predicted by the model. Rather than modifying the model in an attempt to match the actual performance of the system (e.g., the microscope objective is known to have some spherical aberration), we chose instead to fit a curve to the experimental data to obtain the relationship between the index of refraction, n_2 , and the reflected intensity. This technique is outlined in the following section.

A.3. Experimental method

A set of optical windows of known refractive index was used to determine the relationship between reflected intensity and refractive index for a specific configuration of an epi-illumination confocal scanning microscope. The reflected intensities from the surfaces of test samples (fiber-optic imaging bundles) were measured, and the relationship between reflected intensity and refractive index was used to convert the reflected intensity measurements into maps of the refractive indices of the surface of the test samples. The experimental setup used for this technique is shown in Figure A.8.

To obtain the calibration data relating reflected intensity to refractive index, a set of optical-quality windows having known refractive indices are scanned axially through focus. The values of peak reflected intensity are then plotted versus refractive index. A smooth curve representing the relationship between intensity and refractive index is obtained by a second-order polynomial fit. The equation describing the fit is then rearranged to yield the index of refraction as a function of the reflected intensity. Any material whose index is within the range of indices of the reference samples can be examined. In order to assure the same imaging properties for the reference samples

and test samples, each test sample is also scanned through focus, and a maximum intensity projection of the reflected intensity used to determine the refractive index profile. A maximum intensity projection is a two-dimensional image in which each pixel value corresponds to the peak value along an axial line through a three-dimensional image. In this case, the projection is performed in the scan direction (parallel to the optical axis).

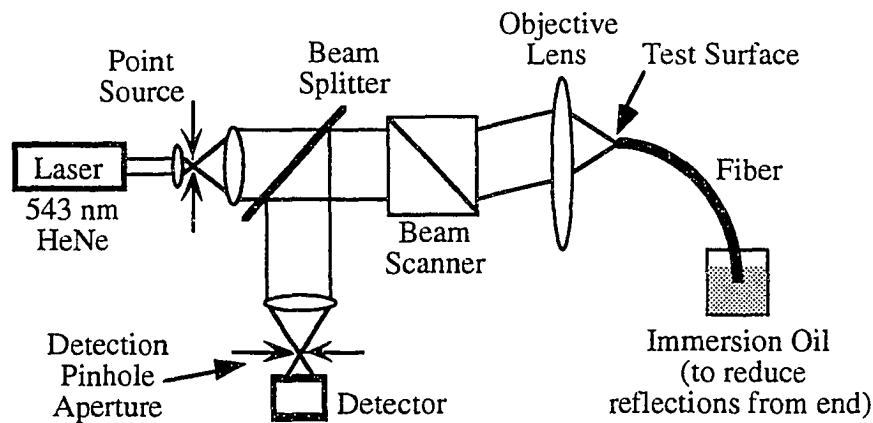


Figure A.8. Experimental setup for measuring the reflection of light from an interface in the focal plane of the objective lens. The pinhole aperture in front of the detector is inserted to make this a confocal microscope. The system used in this work is a Zeiss LSM10 microscope.

The maximum intensity projection is not useful in a non-confocal implementation (detection pinhole-aperture removed) of the system shown in Figure A.8. The image blur with defocus could cause the measured intensity of local regions with low reflection intensity to be greater out-of-focus than in-focus. This is due to the detection of light reflected from surrounding, higher reflection regions of the

defocused sample. This does not occur in the confocal case due to rejection of out-of-focus light by the detection aperture.

The system we have used is a beam-scanning microscope. A slight variation in index measurement results from the variation in imaging across the field of the microscope. This can be minimized by limiting the field-of-view over which measurements are made (we used less than 10% of the system's field-of-view for the experimental results shown below). A better solution is to use a microscope with only on-axis imaging, such as a stage-scanning microscope. This allows spatially-invariant imaging and can accommodate samples whose size is limited only by stage motion.

The reflected intensities from the reference materials were measured with one surface of the optical windows in the sample plane of the microscope and the other surface in air. Reflections from the second face of the window have negligible effect due to the spread of the beam beyond focus. The reference windows used were at least 2 mm thick, but windows as thin as a microscope cover glass (approximately 0.17 mm thick) can be used as well due to the rapid divergence beyond focus of high numerical aperture beams.

For refractive index measurements of an optical fiber, the far end of the fiber was immersed in a medium with a refractive index similar to that of the fiber to minimize back reflections.^{114,115} The near end (examination end) of the fiber was immersed in oil for the 1.4 NA oil-immersion objective, although dry or water-immersion objectives can also be used. With both ends immersed in the same medium, the strength of reflections from the two ends will be comparable for ray angles within the

numerical aperture of the fiber. Thus, the reflected signal within the fiber NA will be approximately equal parts signal (examination-end reflections) and background noise (far-end reflections). The reflected signal from angles beyond the fiber NA will be free of far-end reflections. Thus, use of a high-NA objective lens reduces the importance of reflections from the far end of the fiber, thereby increasing the accuracy of the measurement.

For example, a 1.4 NA beam illuminating an 0.35 NA fiber will be coupled into the fiber with an efficiency of approximately $(0.35/1.4)^2 = 6\%$, while 94% of the illumination light cannot be coupled into the fiber. Combining this with the generally higher reflection at steeper angles yields a far-end reflection that is 1 - 1.5% of the near-end reflection (assuming $n_1 = 1.518$ and $n_2 = 1.45 - 1.50$). The amount of background noise from far-end reflections increases with decreasing numerical aperture, yielding values of 8%, 18%, and 30% for numerical apertures of 1.2, 1.0, and 0.8, respectively. Thus, in the configuration of Figure A.8, measurement accuracy increases with numerical aperture. Alternatively, an objective lens with a central obscuration could be used to eliminate coupling of light into the fiber, or a different immersion medium could be used to increase the examination-end reflections with respect to the far-end reflections.

Reference and test samples must have cleaved or polished surfaces to obtain specular reflections. For this purpose, optical windows make excellent reference samples due to their surface finish. The fiber to be tested can either be cleaved, or ground and polished if the fiber is adequately cleaned after polishing to avoid the effects of residual materials on the fiber surface. It is also necessary to use immersion oil or

another immersion medium that is compatible with both the reference and test samples.

Surface tilt was avoided by mounting the parallel reference windows on a horizontal surface. A tip-tilt stage was used to mount the fiber face in a horizontal position. The fiber was adjusted by viewing the confocal images of the surface. Surface tilt is measured by dividing the amount of focus shift required to bring different parts of the field into focus by the distance between these parts of the field. All measurements were made with a surface tilt of less than 0.5 degrees, and no compensation for tilt effects was included.

Since the reflections from the fiber increase as the fiber index deviates from the immersion medium index, it is not possible with this technique to measure a sample whose range of refractive indices covers both sides of the immersion medium. Thus, while an oil-immersion objective with immersion medium index, n_1 , of 1.518 is suitable for examining silica fiber bundles with refractive indices in the range of 1.45 - 1.50, it will not work for examining a compound glass bundle with refractive indices in the range of 1.4 to 1.6.⁴⁵

Finally, it is important to ensure the stability of the system to guarantee reliable measurements. The reference samples were measured before, between, and after the test samples to monitor this stability. We determined that it was necessary to leave the Zeiss LSM10 microscope on for approximately four hours before making measurements to reach stable operation.

A.4. Results

As discussed above, we have chosen to employ a high numerical-aperture (1.4 NA) oil immersion lens in order to optimize the accuracy, sensitivity, and resolution of our measurements. Using this lens in the experimental configuration of Figure A.8 (confocal detection-pinhole in place), we measured the reflected intensity of a set of known reference samples with indices of refraction of 1.518 (immersion oil), 1.4934 (KCl), 1.4760 (BaF₂), 1.4602 (fused silica), and 1.4350 (CaF₂). Refractive index values are at 543 nm and were obtained from The Infrared Handbook,¹²³ with the exception of the immersion oil whose index is specified as 1.518 at 546 nm by the manufacturer.

In order to obtain the most accurate data about the index of refraction of the fiber, it is desirable to use the full dynamic range of the detector. For the experiments shown here, we were limited to a photomultiplier tube with an 8 bit digitizer. It is preferable to use a detector with a larger dynamic range for greater precision. The set of reference materials was chosen to cover a refractive index range slightly larger than the expected range of the test sample (approximately 1.45 - 1.50). A larger range of reference refractive indices yields greater confidence in the fitted curve, but severely restricts the precision of the measurement possible with our limited dynamic range detector.

Figure A.9 shows the results of the reflected intensity measurements of the reference samples when the microscope is operated in the confocal mode. The results have been fitted to a second-order polynomial. The fitted curve is given by

$$R = 31125(n_2)^2 - 94493(n_2) + 71729, \quad (\text{A.8})$$

where R is the reflected intensity and n_2 is the index of refraction of the test medium. R is a numerical value between 0 and 255, rather than the actual reflected intensity. Equation (A.8) can be solved for index of refraction, n_2 , as a function of reflected intensity

$$n_2 = 1.5180 - \sqrt{3.2129 \times 10^{-5}(R) - 3.4411 \times 10^{-4}}. \quad (\text{A.9})$$

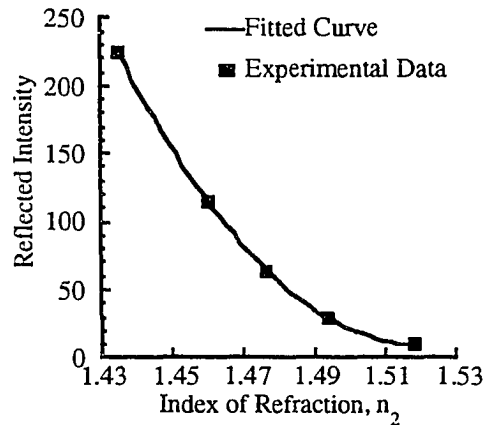


Figure A.9. Experimental results of a set of reference samples and a second-order polynomial curve fit to the data.

High-resolution flexible imaging bundles are typically made of silica doped to increase the core index and/or decrease the clad index. We present here measurements of three bundles of this type. Bundle 1 (Sumitomo Electric Corp. IGN-05/10) has germanium-doped silica cores and fluorine-doped silica clad, yielding an NA of

0.35.⁵¹ Bundle 2 (Fujikura Ltd. FIGH-03-300C) is a silica bundle with a nominal NA of 0.4; none of its material parameters are known.⁹⁴ Bundle 3 (Sumitomo Electric Corp. IGN-10/13) has germanium-doped silica cores and pure silica clad, yielding an NA of 0.3.⁵¹

Figures A.10 - A.12 show the results of this experiment for bundles 1 - 3, respectively. Figure A.13 shows index profiles through the centers of several cores in each bundle. The solid line in Figure A.13 is for bundle 1, the dotted line is for bundle 2, and the dashed line is for bundle 3.

The clad and peak core refractive indices were estimated for each bundle, resulting in the values shown in Table A.1.

Bundle	Specified Numerical Aperture	Measured Clad Index	Measured Peak Core Index	Measured Numerical Aperture
1) Sumitomo Electric Corp. IGN-05/10	0.35	1.454	1.498	0.36
2) Fujikura Ltd. FIGH-03-300C	0.4	1.446	1.500	0.40
3) Sumitomo Electric Corp. IGN-10/13	0.30	1.454	1.496	0.35

Table A.1. Expected and measured parameters of three fiber-optic imaging bundles (identical to Table 4.2).

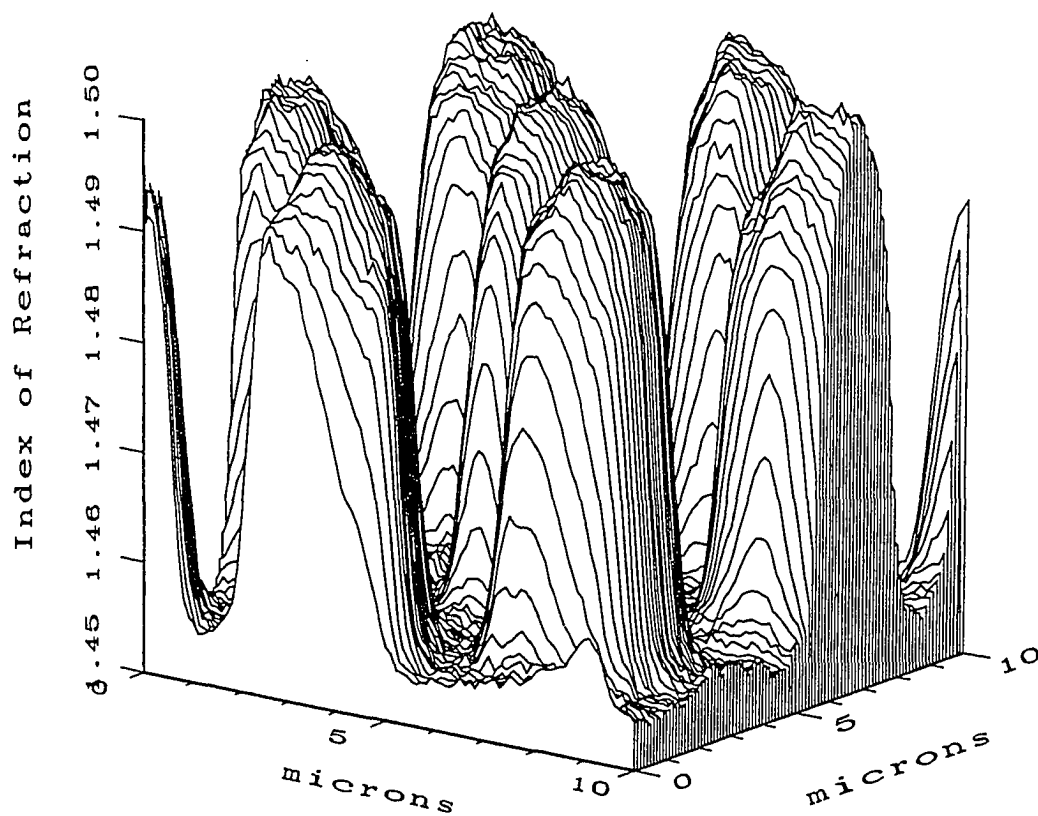


Figure A.10. Index of refraction of a small region of a Sumitomo Electric Corp. IGN-05/10 silica fiber-optic imaging bundle (identical to Figure 4.5a).

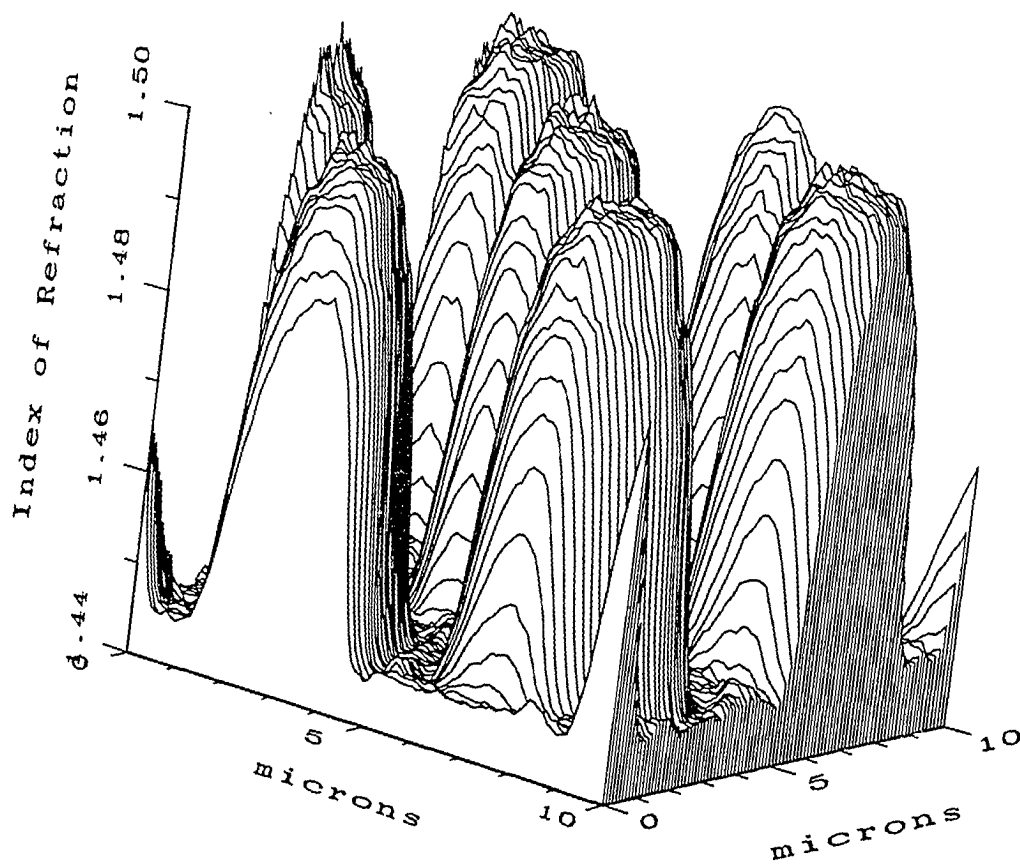


Figure A.11. Index of refraction of a small region of a Fujikura Ltd. FIGH-03-300C silica fiber-optic imaging bundle (identical to Figure 4.5b).

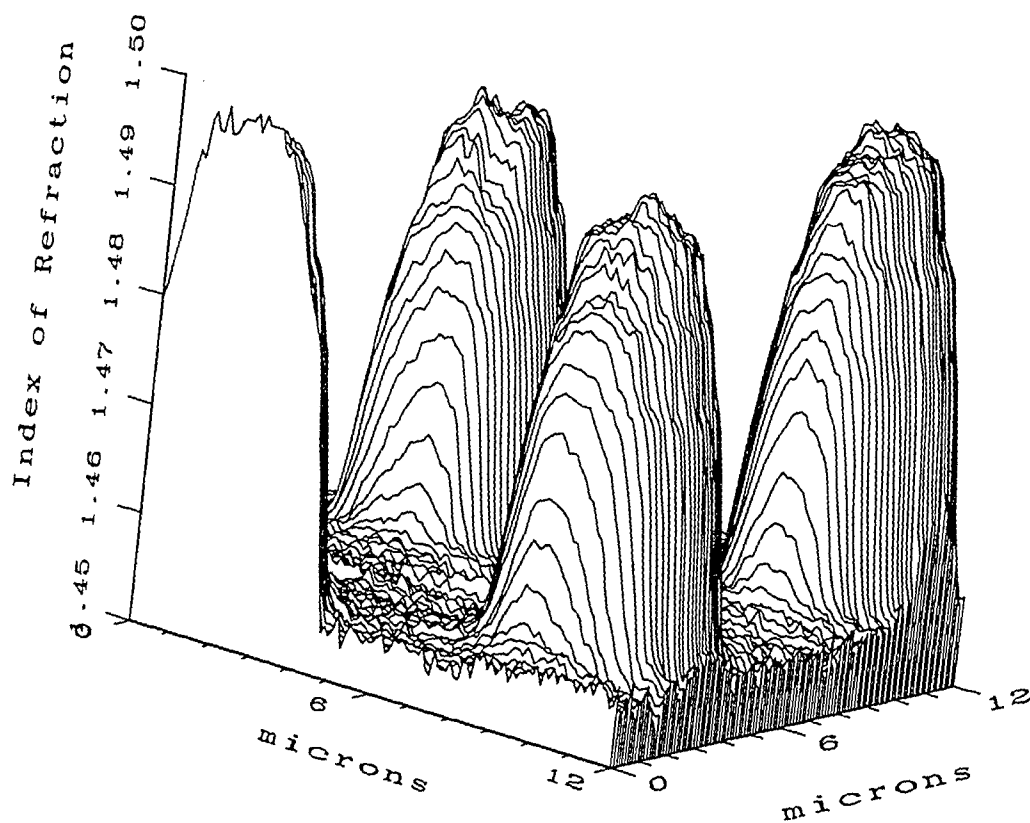


Figure A.12. Index of refraction of a small region of a Sumitomo Electric Corp. IGN-10/13 silica fiber-optic imaging bundle (identical to Figure 4.5c).

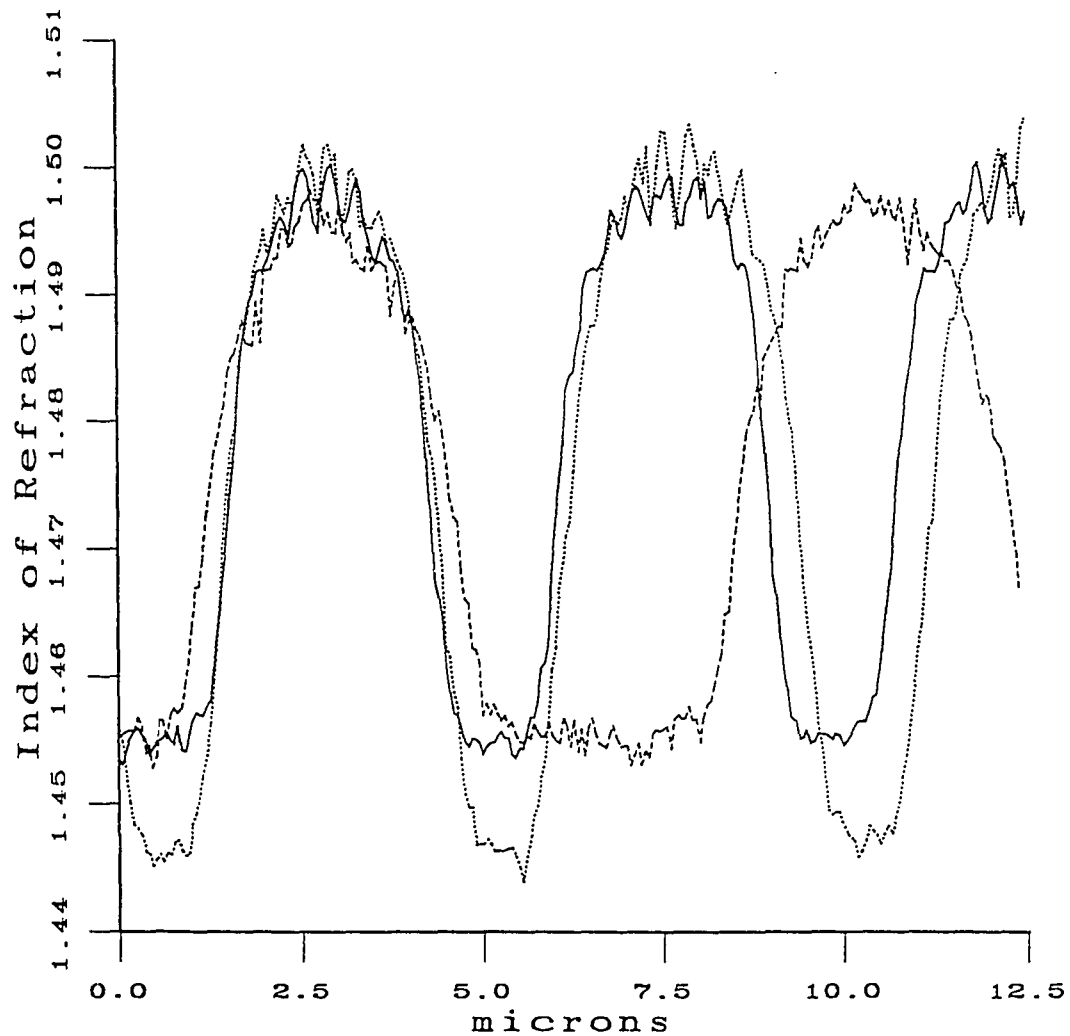


Figure A.13. Profiles through the cores of several silica fiber-optic imaging bundles: Sumitomo Electric Corp. IGN-05/10 (solid line), Fujikura Ltd. FIGH-03-300C (dotted line), and Sumitomo Electric Corp. IGN10/13 (dashed line).

Bundle 1 has a measured clad index of 1.454 and a peak core index of 1.498, resulting in a numerical aperture of 0.36, corresponding well to the manufacturer's specifications. Bundle 2 has a measured clad index of 1.446 and peak core index of 1.500, resulting in a numerical aperture of 0.40, identical to the manufacturer's specifications. From Figures A.10 (bundle 1) and A.11 (bundle 2), as well as Figure A.13 (both bundles), the expected performance of these two bundles can be compared. The resolution is quite close, with core center-to-center spacings of approximately 4.4 μm and 4.7 μm in bundles 1 and 2, respectively. Bundle 2, however, has a higher numerical aperture and, therefore, will be able to accept light over a greater range of incidence angles. Additionally, bundle 2 has a higher packing fraction. Packing fraction is the core area divided by the total (core plus clad) area of an imaging bundle, and is a geometrical optics parameter used to describe input coupling efficiency.

Bundle 3 is from a family of Sumitomo Electric Corp. bundles with lower resolution but more fibers (13,000 - 50,000) than bundle 1 (10,000 fibers). As can be seen in Figures A.12 and A.13, these additional fibers come at the expense of substantially lower resolution and packing fraction. The measured clad and peak core indices of bundle 3 are 1.454 and 1.496, respectively, resulting in a numerical aperture of 0.35. This is somewhat greater than the specified NA of 0.3. We do not know why this bundle is yielding a greater than expected range of refractive indices.

As discussed in chapter 3, the numerical aperture of an optical fiber is given by $NA = \sqrt{n_{core}^2 - n_{clad}^2}$, which specifies the steepest meridional ray that is bound by the fiber (skew rays can be bound at steeper angles). The fibers in these bundles have graded-index cores and, therefore, local numerical apertures. The numerical apertures

specified here are the local numerical apertures at the center of the fiber, where the core refractive index is the highest.

Due to the noise in the images, particularly for high index values, there is some error in determining the index values. Images of the three bundles were evaluated simultaneously, resulting in errors that should be consistent and, therefore, allow reasonable comparison of the three bundles.

The noise for the high indices can be understood from Figure A.9, where the fitted curve flattens out in this region. This is due to the small index difference between n_1 and n_2 in this region. Small errors in measured reflection will correspond to significant errors in index. This source of error can be reduced by using a detector with a larger dynamic range or by changing to an immersion medium whose index, n_1 , is further from the region of interest. For example, a water immersion lens ($n_1 = 1.33$) would provide a compromise between sensitivity to index change and insensitivity to noise and measurement error. Attention needs to be paid to the reference and test materials to ensure compatibility with the immersion medium. KCl is water soluble, for example, and would not make a good reference material in a water immersion system.¹²⁴

There is an additional noise source that produces a periodicity in low intensity regions of an image collected with the Zeiss LSM10 microscope. This is visible in the high index regions of Figure A.13, particularly for the Fujikura bundle (high index regions of the bundles correspond to low reflected intensity due to index of the immersion oil). The source of this noise is unknown.

A.5. Conclusion

We have described a new, non-destructive reflection technique for determining the index of refraction of an optical fiber or other optical material, and have used this technique to evaluate three silica fiber-optic imaging bundles.

REFERENCES

1. Minsky, M., "Microscopy Apparatus," U. S. Patent No. 3013467, (1961, filed 1957).
2. Wilson, T. "Confocal Microscopy," in *Confocal Microscopy*, T. Wilson, ed. (Academic Press, London, 1990).
3. Stelzer, E. H. K., "The intermediate optical system of laser-scanning confocal microscopes" in *The Handbook of Biological Confocal Microscopy*, J. Pawley, Ed. (Plenum, Madison 1989).
4. Dabbs, T., and M. Glass, "Fiber-optic confocal microscope: FOCON," Appl. Opt. **31**, 3030 (1992).
5. Kimura, S., and T. Wilson, "Confocal scanning optical microscopes using single-mode fiber for signal detection," Appl. Opt. **30**, 2143-2150 (1991).
6. Gu, M., C. J. R. Sheppard, and X. Gan, "Image formation in a fiber-optical confocal scanning microscope," J. Opt. Soc. Am. A **8**, 1755 (1991).
7. Delaney, P. M., M. R. Harris, and R. G. King, "Novel microscopy using fibre optic confocal imaging and its suitability for subsurface blood vessel imaging in vivo," Clinical and Experimental Pharmacology and Physiology **20**, 197 (1993).
8. P. M. Delaney, R. G. King, J. R. Lambert, and M. R. Harris, "Fibre optic confocal imaging (FOCI) for subsurface imaging of the colon in vivo," J. Anat. **184**, 157 (1994).
9. Born, M., and E. Wolf, *Principles of Optics*, 6th ed., (Pergamon, Oxford, 1980).
10. Nomarski, G., "Simple method for reducing the depth of focus," JOSA **65**, 1166 (1975).
11. Goodman, D., *Confocal Microscopy*, Tutorial Short Course Notes, SPIE Symposium on Microlithography (1989).
12. Wilson, T., "The role of the pinhole in confocal imaging systems," in *The Handbook of Biological Confocal Microscopy*, J. Pawley, Ed. (Plenum, Madison 1989).
13. Sheppard, C. J. R., and T. Wilson, "Effects of high angles of convergence on $V(z)$ in the scanning acoustic microscope," Appl. Phys. Lett. **38**, 858 - 859 (1981).
14. Wells, K. S. , D. R. Sandison, J. Strickler, and W. W. Webb, "Quantitative fluorescence imaging with laser scanning confocal microscopy," in *The*

REFERENCES - Continued

- Handbook of Biological Confocal Microscopy*, J. Pawley, Ed. (Plenum, Madison 1989).
15. Wilson, T., and S. J. Hewlett, "Optical sectioning strength of the direct-view microscope employing finite sized pin-hole arrays," *J. Micros.* **163**, 131 - 150 (1991).
 16. Wilson, T., "Optical aspects of confocal microscopy," in *Confocal Microscopy*, T. Wilson, ed. (Academic Press, London, 1990)
 17. Bertero, M., P. Boccacci, G. J. Brakenhoff, F. Malfanti, and H. T. M. van der Voort, "Three-dimensional image restoration and super resolution in fluorescence confocal microscopy," *J. Micros.* **157**, 3 - 20 (1990).
 18. General Scanning Inc. product literature - Series G Optical Scanners, Watertown, Massachusetts (617)924-1010.
 19. Masters, B. R., and A. A. Thaer, "Real-time scanning slit confocal microscopy of the *in vivo* human cornea," *Appl. Opt.* **33**, 695 - 701 (1994).
 20. Koester, C. J., S. M. Khanna, H. D. Rosskethen, R. B. Tackaberry, and M. Ulfendahl, "Confocal slit divided-aperture microscope: applications in ear research," *Appl. Opt.* **33**, 702 - 707 (1994).
 21. Kino, G., "Intermediate Optics in Nipkow Disk Microscopes," in *The Handbook of Biological Confocal Microscopy*, J. Pawley, Ed. (Plenum, Madison 1989).
 22. Shack, R. V., P. H. Bartels, R. A. Buchroeder, R. L. Shoemaker, D. W. Hillman, and D. Vukobratovich, "Design for a fast fluorescence laser scanning microscope," *Anal. Quant. Cytol. Histol.*, **9**, 509 - 520 (1987)
 23. Keller, H. E. "Objective lenses for confocal microscopy," in *The Handbook of Biological Confocal Microscopy*, J. Pawley, Ed. (Plenum, Madison 1989).
 24. Corcuff, P., C. Bertrand, and J. L. Leveque, "Morphometry of human epidermis *in vivo* by real-time confocal microscopy," *Arch. Dermatol. Res.* **285**, 475 (1993).
 25. Gratton E. and M. J. vandeVen "Laser sources for confocal microscopy," in *The Handbook of Biological Confocal Microscopy*, J. Pawley, Ed. (Plenum, Madison 1989).
 26. Chen, V., "Non-laser illumination for confocal microscopy," in *The Handbook of Biological Confocal Microscopy*, J. Pawley, Ed. (Plenum, Madison 1989).

REFERENCES - *Continued*

27. Wilson, T., and S. J. Hewlett, "The use of annular pupil plane filters to tune the imaging properties in confocal microscopy," *J. Mod. Opt.* **37**, 2025 - 2046 (1990).
28. Hegedus, Z. S., "Pupil filters in confocal imaging," in *Confocal Microscopy*, T. Wilson, ed. (Academic Press, London, 1990).
29. Wijnaendts-van-Resandt, R. W., "Semiconductor metrology," in *Confocal Microscopy*, T. Wilson, ed. (Academic Press, London, 1990).
30. Corcuff P. and J. L. Leveque, "In vivo vision of the human skin with the tandem scanning microscope," *Dermatology* **186**, 50 (1993).
31. Snyder, A. W. and J. D. Love, *Optical Waveguide Theory*, (Chapman & Hall, London, 1991).
32. Hopkins, H. H., "Physics of the Fibreoptic Endoscope," in *Endoscopy*, G. Berci ed., (Appleton-Century-Crofts, New York, 1976).
33. Marcuse, D., *Theory of Dielectric Optical Waveguides*, 2nd ed., (Academic Press, San Diego, 1991).
34. Midwinter, J. E., *Optical Fibers for Transmission*, (Wiley, New York, 1979).
35. Gloge, D., "Weakly guiding fibers," *Appl Opt.* **10**, 2252 (1971).
36. Potter, R. J., E. Donath, and R. Tynan, *J. Opt. Soc. Am.* **51**, 1079 (1961).
37. Siegmund, W. P., "Fiber Optics," in *Applied Optics and Optical Engineering*, Vol. 4, R. Kingslake, Ed., (Academic Press, NY, 1967).
38. Hentschel, C., *Fiber Optics Handbook*, (Hewlett-Packard GmbH, Boeblingen, Germany, 1989).
39. Siegmund, W., Schott Fiber Optics, private communication, 1993.
40. Polymicro Technologies, Inc. product literature, Phoenix, Arizona, (602)375-4100.
41. 3M Specialty Optical Fibers product literature, West Haven, Connecticut, (203)934-7961.
42. Chigusa, Y., K. Fujiwara, Y. Hattori, and Y. Matsuda, "Properties of silica glass image fiber and its application," *Optoelectronics* **1**, 203-216 (1986).

REFERENCES - *Continued*

43. Fujiwara, K., Y. Hattori, M. Kyoto, Y. Matsuda, Y. Chigusa, A. Urano, K. Yoshimura, and T. Kadota, "Development of a 250,000-pixel image fiber," *Sumitomo Electric Technical Review* **26**, 82 - 88 (1987).
44. Okoshi, T., *Optical Fibers*, (Academic Press, Orlando, 1982).
45. Schott Fiber Optics product literature, Southbridge, Massachusetts, (800)343-6120.
46. South Coast Fiber Optics product literature, Santa Maria, California, (805)928-3360.
47. Poly-optical Products, Inc. product literature, Santa Ana, California, (714)250-8557.
48. Suzuki, F., "Novel plastic image-transmitting fiber," *Proc. SPIE* **1592**, 150 (1991).
49. Gal, D. and A. Katzir, "Silver Halide optical fibers for medical applications," *IEEE J. Quant. Elect.* **CIO-23**, 1827 - 1835 (1987).
50. Siegmund, W., Schott Fiber Optics, private communication, Feb. 2, 1993.
51. Sumitomo Electric Corp. product literature, Torrance, CA, (310)782-0227, Naomi Uji.
52. Reference #31, chapter 23.
53. J. L. Baird, *Brit. Pat. Spec No. 20,969/27* (1927).
54. C. W. Hansell, *U. S. Patent 1,751,584* (1930, filed 1927).
55. Hopkins, H. H., and N. S. Kapany, "A flexible fibrescope, using static scanning," *Nature* **173**, 39 (1954).
56. H. Ohzu, "Image transmission properties of fiber bundles," Appendix A in *Fiber Optics* by N. Kapany, (Academic Press, New York, 1967).
57. Conde, R., C. Depeursinge, O. Coquoz, and F. Taleblou, "Comparative Measurements of Image Quality in Image Guides," *Proc. SPIE* **2131** (1994).
58. Kiat, L. S., K. Tanaka, T. Tsumanuma, and K. Sanada, "Ultrathin single-mode imagefiber for medical usage," *Proc. SPIE* **1649**, 208 (1992).

REFERENCES - *Continued*

59. Fujikura America Ltd. product literature, Santa Clara, California, (408)988-7405 Ted Kumakawa or (408)748-6991 Robert Dahlgren.
60. Moritex product literature, San Diego, California, (800)548-7039.
61. Utsumi, et. al., "Present status of development of medical instruments and systems," article obtained from Mitsubishi Cable America, Inc., New York, New York, (212)888-2270, Mr. Y. Yamogata (1992).
62. Dolan Jenner Industries Inc. product literature, Woburn, Massachusetts, (800)833-4237.
63. Applied Fiberoptics product literature, Southbridge, Massachusetts, (800)225-7486
64. Electro Fiberoptics Corp. product literature, Marlboro, Massachusetts, (800)445-7016, Konrad Leisi.
65. Sumita Optical Glass product literature, Briarcliff Manor, New York, (914)762-2639.
66. Galileo Electro-optics Corp. private communication, 4/92, Forest, Virginia, (800)648-1800.
67. Siegmund, W. P., "Fiber Optics", in *Optical Society of America Handbook of Optics*, (McGraw Hill, New York, 1978).
68. Snyder, A. W. and P. McIntyre, "Crosstalk between light pipes," J. Opt. Soc. Am. **66**, 877 (1976).
69. Hopkins, H. H., and N. S. Kapany, "Transparent fibres for the transmission of optical images," Opt. Acta. **1**, 164, (1955).
70. Kapany, N. S., "Fiber Optics. V. Light Leakage," J. Opt. Soc. Am. **49**, 770 (1959).
71. Kapany, N. S., "Fiber Optics. VI. Image Quality and Optical Insulation," J. Opt. Soc. Am. **49**, 779 (1959).
72. Hosono, T., "Transmission characteristics of image fiber," Electronics and Communications in Japan, **66-C**, No. 11, 111 (1983).
73. Mogi, M. and K. Yoshimura, "Development of super high density packed image guide," Proc. SPIE **1067**, 172-181 (1989).

REFERENCES - *Continued*

74. Indirect measurement of crosstalk obtained from Sumitomo Electric Corp., 10/12/93, showing acceptable contrast up to 90×10^3 fibers/mm² and attributing the limitation to crosstalk.
75. Komiyama, A., and M. Hashimoto, "A new class of crosstalk in image fibers," *Opt. Comm.* **107**, 49 (1994).
76. Siegmund, W., "Fiber optic imaging in medicine," *Proc. SPIE* **1649**, 162 - 171 (1992).
77. Drougard, R., "Optical Transfer Properties of Fiber Bundles," *J. Opt. Soc. Am.* **54**, 907 (1964).
78. Kapany, N. S., J. A. Eyer, and R. E. Keim, "Fiber Optics. Part II. Image Transfer on Static and Dynamic Scanning with Fiber Bundles," *J. Opt. Soc. Am.* **47**, 423 (1957).
79. Vanwormhoudt, M. and W. DeKinder, "Space variant imagery in fiber optics," Appendix C in *Fiber Optics* by N. Kapany (Academic Press, New York, 1967).
80. Marhic, M. E., S. E. Schacham, and M. Epstein, "Misalignment in imaging multifibers," *Appl. Opt.* **17**, 3503 (1978).
81. Csorba, I., P. *Image Tubes* (Howard W. Sams and Co., Inc., Indianapolis, 1985).
82. Allen, W. B., *Fiber Optics* (Plenum, 1973).
83. Eberhardt, E. H., "The modulation transfer function of microchannel and fiber optic plates," Technical Note 126, ITT Electro-Optical Products Division, Fort Wayne, IN (703)563-0371 (1980).
84. Player, M. A., "Spread functions and modulation transfer functions of fibre-optic bundles," *J. Mod. Opt.* **35**, 1363 (1988).
85. Roetling, P. G., and W. P. Ganley, "Observations on the dynamic frequency response of fiber bundles," *J. Opt. Soc. Am.* **52**, 99 (1962).
86. Cook, L. M., "Fractal fiber optics," *Appl. Opt.* **30**, 5220 (1991).
87. Kaneda, K., T. Ohashi, T. Tsumanuma, and K. Sanada, "Ultrathin fiberscope for stereoscopic vision," *Proc. SPIE* **1889**, 233 (1993).
88. Tsumanuma, T., K. Sanada, and K. Inada, "The Ultrathin Silica-Based Imagefiber for Medical Usage," *Fujikura Technical Review* **19** (1989).

REFERENCES - *Continued*

89. Nakatate, K., N. Syamoto, T. Ohashi, T., Tsumanuma, and K. Sanada, "Silica-based rod lens for the medical fiberscope," Proc. SPIE **2131** (1994).
90. Wild, V. Biogeneral Corp., San Diego, CA, (619)453-4451, private communication, May, 1992.
91. Saito, M., M. Takizawa, S. Sakuragi, and F. Tanei, "Infrared image guide with bundled As-S glass fibers," Applied Optics **24**, 2304 (1985).
92. Paiss, I., F. Moser, and A. Katzir, "Properties of silver halide core-clad fibers and the use of fiber bundle for thermal imaging," Fiber And Integrated Optics **10**, 275 (1991).
93. Kersey, A., Naval Research Lab, private communication, May, 1995.
94. Dahlgren, R., Fujikura Technology America, private communication, Feb. 20, 1995.
95. Gloge, D., and E. A. J. Marcatelli, "Multimode theory of graded-core fibers," Bell Syst. Tech. J. **52**, 1563 - 1578 (1973).
96. W. S. Grundfest and T. Papaionnou, *Endoscopic Technology and Applications*, SPIE Short Course SC8, Biomedical Optics '93, Budapest, Hungary (1993).
97. W. P. Siegmund, *Engineering of Endoscopes*, SPIE Short Course SC04, International Symposium on Optics, Imaging, and Instrumentation, San Diego (1993).
98. Juskaitis, R., and T. Wilson, "Differential confocal scanning microscope with a two-mode optical fiber," Appl. Opt. **31**, 898 (1992).
99. Juskaitis, R. and T. Wilson, "Surface profiling with scanning optical microscopes using two-mode optical fibers," Appl. Opt. **31**, 4569 (1992).
100. Aziz, D. J. and A. F. Gmitro, "Confocal Microscopy via a fiber-optic imaging-bundle," Proc. SPIE **1893**, 53 (1993).
101. Gmitro, A. F. and D. J. Aziz, "Confocal microscopy through a fiber-optic imaging-bundle," Opt. Lett. **18**, 565 (1993).
102. Aziz, D. J., and A. F. Gmitro, "Imaging performance of the fiber-optic image-bundle confocal microscope," Proc. SPIE **2083**, 139 (1993).

REFERENCES - *Continued*

103. Martin, L. C., *The Theory of the Microscope*, (American Elsevier, New York, 1966).
104. Nippon Sheet Glass SELFOC Product Guide, Somerset, New Jersey, (908)469-9650 (1991).
105. LightPath Technologies product literature, Tucson, Arizona, (520)884-7424.
106. Wong, M., Nippon Sheet Glass, private communication, Jan. 1993.
107. Sanford, P., Erie Scientific, private communication, (800)258-0834, 1994.
108. Immunological Reagents for Research Catalog, Jackson Immuno-Research Laboratories, Inc., West Grove, Pennsylvania, (800)367-5292, (1993).
Alternatively, contact Molecular Probes, Eugene, Oregon (503)344-3007.
109. Gosse, T., General Scanning, Inc, private communication July 25, 1994.
110. Rolyn Optics Company catalog, Covina, California (818)915-5707.
111. Conde, R., Swiss Federal Institute of Technology, Lausanne, private communication, Feb. 24, 1994.
112. Wolf, E., "Electromagnetic diffraction in optical systems I. An integral representation of the image field," *Proc. Roy. Soc. A*, **253**, 349-357 (1959).
113. Goodman, J., *Introduction to Fourier Optics* (McGraw Hill, New York, 1968).
114. Ikeda, M., M. Tateda, and H. Yoshikiyo, "Refractive index profile of a graded index fiber: measurement by a reflection method," *Appl. Opt.* **14**, 814 -815 (1975).
115. Eickhoff, W., and E. Weidel, "Measuring method for the refractive index profile of optical glass fibers," *Opt. Quantum Electron.* **7**, 109-113 (1975).
116. Costo, B., and B. Sordo, "Measurement of the refractive index profile in optical fibers: comparison between different techniques," *Second European Conference on Optical Fiber Communication* (Paris, 1976).
117. Tateda, M., "Single-mode-fiber refractive-index profile measurement by reflection method," *Appl. Opt.* **17**, 475 - 478 (1978).
118. Zhu, X., and K. Iga, "A scanning total reflection method for refractive-index profiling," *Japan J. Appl. Phys.* **28**, 1497 - 1500 (1989).

REFERENCES - Continued

- 119 Ruschin, S., J. Xu, H. Chung, and W. S. C. Chang, "A filtered-transform microscope method for refractive-index profiling of optical waveguides and surface profiling," *J. Lightwave Technol.* **8**, 1703 - 1708 (1990).
- 120 Ghatak, A., and K. Thyagarajan, "Graded index optical waveguides: a review," in *Progress in Optics XVIII*, E. Wolf, ed., (North Holland, 1980).
- 121 Zhong, Q., and D. Inniss, "Characterization of the Lightguiding Structure of Optical fibers by Atomic Force Microscopy," *J. Lightwave Technol.* **12**, 1517 - 1523 (1994).
- 122 Richards, B., and E. Wolf, "Electromagnetic diffraction in optical systems II. Structure of the image field in an aplanatic system," *Proc. Roy. Soc. A*, **253**, 358 - 379 (1959).
- 123 Wolfe, W. L., and G. J. Zissis, *The Infrared Handbook*, revised edition (Environmental Research Institute of Michigan, 1989).
124. Optical Crystal Handbook, Optivac Corporation, N. Brookfield, Massachusetts, (508)867-6444, (1993).